PHOTONICS INSIGHTS

Terahertz spin dynamics in rare-earth orthoferrites

Xinwei Li,[a,b] Dasom Kim,[b,c] Yincheng Liu,[a] and Junichiro Kono[b,d,e,*]
[a]Department of Physics, California Institute of Technology, Pasadena, USA
[b]Department of Electrical and Computer Engineering, Rice University, Houston, USA
[c]Applied Physics Graduate Program, Smalley-Curl Institute, Rice University, Houston, USA
[d]Department of Physics and Astronomy, Rice University, Houston, USA
[e]Department of Materials Science and NanoEngineering, Rice University, Houston, USA

Abstract. Recent interest in developing fast spintronic devices and laser-controllable magnetic solids has sparked tremendous experimental and theoretical efforts to understand and manipulate ultrafast dynamics in materials. Studies of spin dynamics in the terahertz (THz) frequency range are particularly important for elucidating microscopic pathways toward novel device functionalities. Here, we review THz phenomena related to spin dynamics in rare-earth orthoferrites, a class of materials promising for antiferromagnetic spintronics. We expand this topic into a description of four key elements. (1) We start by describing THz spectroscopy of spin excitations for probing magnetic phase transitions in thermal equilibrium. While acoustic magnons are useful indicators of spin reorientation transitions, electromagnons that arise from dynamic magnetoelectric couplings serve as a signature of inversion-symmetry-breaking phases at low temperatures. (2) We then review the strong laser driving scenario, where the system is excited far from equilibrium and thereby subject to modifications to the free-energy landscape. Microscopic pathways for ultrafast laser manipulation of magnetic order are discussed. (3) Furthermore, we review a variety of protocols to manipulate coherent THz magnons in time and space, which are useful capabilities for antiferromagnetic spintronic applications. (4) Finally, new insights into the connection between dynamic magnetic coupling in condensed matter and the Dicke superradiant phase transition in quantum optics are provided. By presenting a review on an array of THz spin phenomena occurring in a single class of materials, we hope to trigger interdisciplinary efforts that actively seek connections between subfields of spintronics, which will facilitate the invention of new protocols of active spin control and quantum phase engineering.

Keywords: terahertz spin dynamics; magnetism; orthoferrite; ultrafast spectroscopy; magneto-optics.

Received Sep. 2, 2022; revised manuscript received Oct. 24, 2022; accepted Nov. 10, 2022; published online Jan. 18, 2023.

[DOI: 10.3788/PI.2022.R05]

1 Introduction

Physicists have long known that electron spins are the central player of magnetism in solid-state matter. Within a host crystal lattice, spins spontaneously align their orientations to minimize the global free energy, creating a variety of magnetic phases with distinct spin configurations. Understanding the energetics is therefore key to understanding the properties of quantum magnets in equilibrium and has been the central goal of study since early years. Starting from the beginning of this century, however, the field of modern condensed matter physics has witnessed an explosive growth of interest in spin *dynamics*, that is, the evolution of spins in time in magnetic solids. Such interest comes with growing awareness of the important roles spin kinetics play in three major contemporary problems (Fig. 1) that are significant not only for the fundamental physics of quantum materials but also for practical technological advances.

On one hand, there is a strong motivation for producing devices that can process information with clock rates faster than the current electronic technology by orders of magnitude.

*Address all correspondence to Junichiro Kono, kono@rice.edu

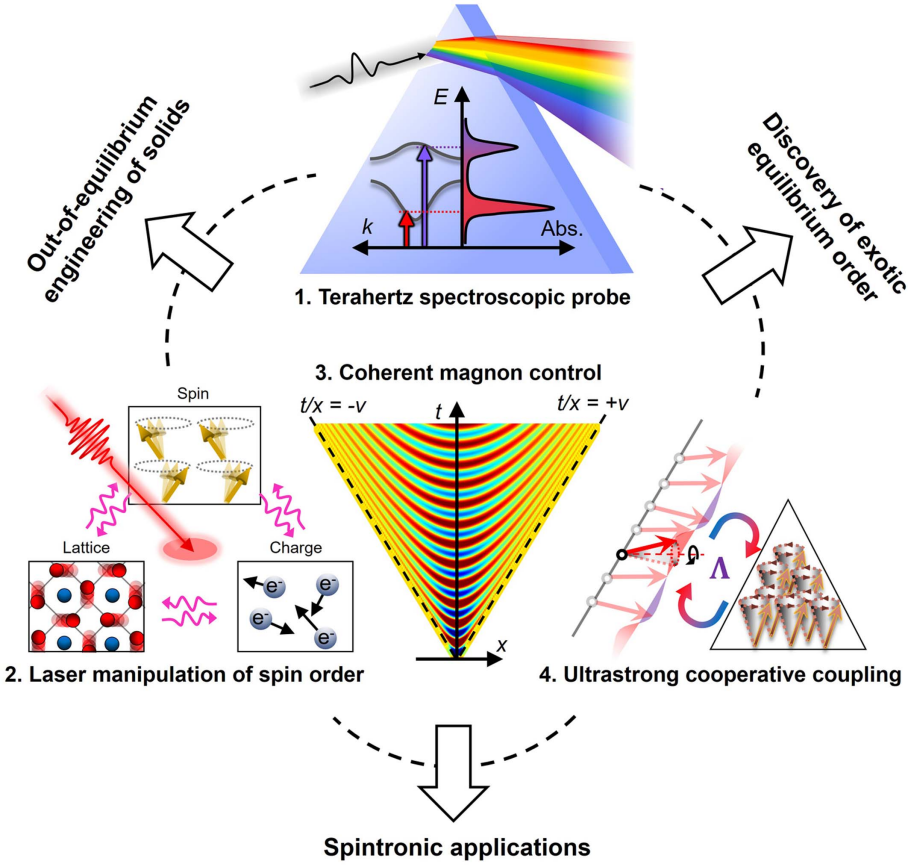

Fig. 1 Overview of current scientific and technological interests related to spin dynamics in solid-state materials. Four topics arranged as smaller triangular elements are covered in this review, which are key elements for achieving the three grander goals (three sides of the larger triangle).

Following Moore's law, the compactness of circuit boards has been increased to an unprecedented level, but the information processing speed, that is, the clock rates of computer chips, has remained on the GHz scale for many years[1]. The goal of spintronics research is to harness spin dynamics, whose natural time scale is picoseconds (ps) in antiferromagnets, to build processing units that are not only significantly faster in clock rate but also robust against charge perturbations, low in energy consumption, and smaller in device footprints[2–5]. What further empowers such a vision is the prospect of wave-based computation[6–10]; by using collective spin resonances (i.e., magnons), one can encode, convert, and transport information, and perform logical operations based on coherent wave interference and nonlinear wave interactions.

On the other hand, this is related to a more fundamental venue in condensed matter physics, with the aim to discover and understand exotic phases in quantum materials[11]. Although each contemporary condensed matter problem can be complex in its own way[12–14], it is not uncommon to find spin dynamics playing a key role in conceptually significant model systems; examples include the Hubbard model and the Kondo model for correlated systems that exhibit high-T_c superconductivity[15] or quantum criticality[16], and the Ising models[17] (of various flavors) and the Kitaev model[18] for assorted ordered or disordered quantum magnets. Clarifying spin excitations in these complex material classes by spectroscopy means provides a clue for the essential microscopic processes at play.

Opportunities for studying out-of-equilibrium dynamics arise when pulsed laser sources are used to drive quantum magnets impulsively. The interest is fueled by the emergence of ultrafast laser technology[19,20], which provides various experimental settings with time resolutions fine enough to resolve the motions of spins *in situ*. Broadly speaking, the technique is able to selectively drive a resonance mode and track in real time the subsequent decay pathways of various degrees of freedom (DOFs) back to equilibrium[21–30]. It reveals the fundamental time scales of spin motion and their interaction with the charge and lattice DOFs. When the excitation is strong enough to shift the balance of competing energy scales so as to modify the free-energy landscape, a light-induced magnetic phase transition can occur[31], bringing the grand pursuit of nonequilibrium control of quantum systems[32], a topic that has long prevailed in atomic, molecular, and optical physics, to a solid-state context. Phenomena that are impossible to be found in thermal equilibrium can thus be investigated, such as dynamical phase transitions[33], quench dynamics[34], and nonthermal quantum states[35].

In recent years, the aforementioned interest in creating efficient spintronic devices, discovering exotic equilibrium orders, and out-of-equilibrium phase engineering has coincided with a few technical advancements proven crucial for their proliferation. High-intensity broadband ultrafast lasers are the ideal instruments for both spectroscopy studies in equilibrium and out-of-equilibrium engineering. One of the most important

developments has been made in time-domain terahertz (THz) spectroscopy techniques[36–38], which closes the THz technology gap, a spectral region that is scientifically important (since it is on resonance with major spin, lattice, and charge excitations) but traditionally hard to access either from the low-frequency (electronics) or high-frequency (photonics) side. In addition, improvements on computational tools have been made to cope with quantum materials with many-body correlation effects[39–46]; some can be even applied to simulate the nonequilibrium state of complex materials, providing significant predictive powers to experiments.

The confluence of interests to address the currently exciting problems (outlined in Fig. 1) with the advent of state-of-the-art experimental and theoretical approaches has led to a rapid expansion in the body of work within the area of THz spintronics and ultrafast quantum materials. The objective of this review paper is to discuss selected recent studies that directly address the core subjects of THz spin dynamics, light–spin coupling, and ultrafast magnetism. To put it concretely, we hope to comprehensively review all the THz-frequency phenomena related to spin dynamics that have been demonstrated so far in rare-earth orthoferrites ($RFeO_3$, with R representing a rare-earth element). Four specific subjects are chosen, which are outlined in Fig. 1 as four small triangular elements that constitute the larger triangle representing motivations from a broader vision. Before introducing the scope of each section, we first clarify the logic for choosing these topics, especially the reason for confining ourselves to THz-frequency phenomena and $RFeO_3$ systems while discussing spin dynamics.

First, our focus is on THz-frequency phenomena, or equivalently, ps time-scale dynamics because the THz frequency range coincides with the characteristic energy scale not only for spin–spin exchange interaction in most antiferromagnets, but also for lattice excitations and certain charge excitations within the same host material[47,48]. With the increasing capability of generating and manipulating THz radiation using the current ultrafast technology, all these DOFs can be interrogated in a single experimental setting. This brings convenience to investigating dynamical coupling of spins to lattice and charge, which is the reason why the number of spintronics studies in the THz range has increased rapidly in recent years[49].

Second, this review focuses on $RFeO_3$ systems exclusively to set a paradigm of a near-exhaustive discussion of all THz-frequency dynamical spin phenomena observed so far in a single class of materials, even though the principles and phenomena therein can easily go beyond $RFeO_3$ and generalize to a broader range of material classes. As shown in Fig. 2, if one defines a "phase space" for the entire research field of spin dynamics, spanned by a horizontal axis representing the array of material systems and another vertical axis listing various physical phenomena, most review papers arrange their discussion in a way similar to making horizontal cuts in phase space. This means that each of them has a topic orienting to a particular physical phenomenon, and a variety of material systems are mentioned in which the core physics manifests. The method is certainly advantageous in elucidating a newly established physical principle to the community, but its drawback is that the discussion needs to be constantly interrupted by introducing basic properties of various material systems before their connections with the core physics can be elucidated. Our attempt here is to present a review by performing a vertical cut in phase space, the advantage of which is the emergence of a grand

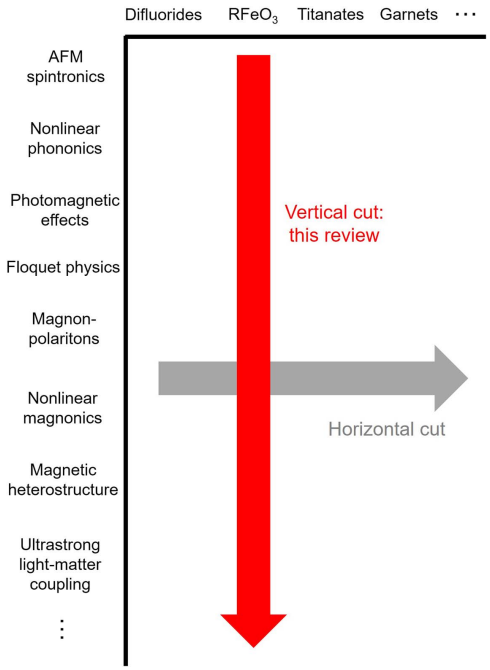

Fig. 2 "Phase space" for review articles in spintronics, spanned by the horizontal axis of materials and vertical axis of novel physical phenomena. The current review represents a vertical cut in the phase space.

picture encompassing assorted types of interesting physics that can be accessed from one material class. This way emphasizes more the connections among various physical phenomena, and the background knowledge associated with the material needs to be presented only once. The prerequisite for our approach is that the basic properties of the target material need to be understood well enough for extensive discussions of novel phenomena to build upon, and we believe that $RFeO_3$ is the first class of compounds in the transition metal (TM) oxide family that satisfies the criterion based on past research. TM oxides form the playground of a vast collection of significant concepts in condensed matter physics[50], including magnetism, strong electron correlations[51], insulator–metal transitions[14], charge density waves[52], orbital order[53], ferroic order[54], high-T_c superconductivity[55], and dimensionality control. The $RFeO_3$ class is related to magnetism and ferroic order among the list but avoids many of the issues that so far remain enigmatic. As fundamental understanding of more complex materials advances, our "vertical-cut" methodology may hopefully find broader usage.

Our discussions are divided into five major sections. Section 2 introduces the background knowledge on the $RFeO_3$ system and experimental methods that have been adopted to study THz-frequency spin dynamics in them. Section 3 focuses on the weak excitation regime of the spin sector by light, namely, using light as a probe to obtain information on the magnetic structure in equilibrium, thermodynamic spin transitions, and elementary excitations that are closely related to the ground states. Section 4 discusses light-induced magnetic phase transitions, where light excitation is no longer a weak perturbation but actively modifies the free-energy landscape of the spin system. Assorted thermal and nonthermal pathways of laser control of magnetism will be examined. In Section 5, our discussions lean slightly towards the application side, which address the issue of

how spin excitations in $RFeO_3$ can be useful in the emerging field of antiferromagnetic (AFM) spintronics and quantum control. Coherent control, polariton devices, magnetic heterostructuring, and nonlinear spin excitations are the major topics in this context. Section 6 provides insight into an emerging interdisciplinary field that merges spintronics with a key concept in quantum optics, that is, ultrastrong light–matter coupling. Viewing dynamic spin–spin interactions from a new angle, the connection between certain magnetic phase transitions in condensed matter systems and the Dicke superradiant phase transition (SRPT) in quantum optics will be clarified. Finally, we end the review by giving an outlook on opportunities that lie in the future by making connections among various intriguing phenomena reviewed in this paper.

Due to the broad range of topics covered by the current paper, we also recommend interested readers to refer to recent excellent reviews, each of which addresses a topic in more depth. These include the topics of ultrafast manipulation of magnetic order[31,56], photomagnetic effects[57], ultrafast spectroscopy studies of quantum materials and strongly correlated systems[58–61], nonthermal laser control of quantum materials[62], nonlinear phononics[63,64], Floquet engineering[65,66], AFM spintronics[4,5,67–69], multidimensional THz spectroscopy[70], cavity quantum materials[71,72], and ultrastrong light–matter coupling[73,74].

2 Background Knowledge

In this section, we present the background knowledge required for understanding the discussions in the following sections. Two aspects will be emphasized. First, in Subsection 2.1, we describe the basic physical properties of $RFeO_3$ materials, including their crystal and magnetic structures, symmetry classifications, phase diagrams, optical properties, and elementary excitations including phonons and magnons. Second, in Subsection 2.2, we provide an introductory survey of the most widely used ultrafast optical techniques for studying THz spin dynamics. These techniques are used for various time-resolved photomagnetic/magneto-optical experiments as well as THz time-domain spectroscopy experiments; the latter includes THz transmission spectroscopy, emission spectroscopy, and nonlinear spectroscopy using intense THz pulses for selectively driving excitations far from equilibrium.

2.1 The $RFeO_3$ Class

The $RFeO_3$ class has been extensively studied ever since it was first identified in the 1940s; the first review paper on $RFeO_3$ appeared in 1969[75]. These crystals have an orthorhombically distorted perovskite structure with four molecular units (20 atoms) per unit cell. The lattice structure is described by the centrosymmetric space group $D_{2h}^{16} - Pbnm$.[1] The Fe^{3+} and R^{3+} ions occupy the $4(b)$ and $4(c)$ positions, respectively, and are responsible for producing magnetism.

To understand the various magnetic phases that appear in this family, it is essential to first introduce Bertaut's analysis of magnetic structures using representation theory[76]. The theory is distinct from the conventional approach of Shubnikov groups[77] to classify magnetic structures, because it does not seek the collection of operations that would leave the symmetry invariant. Instead, it outlines the transformation properties of a magnetic structure under the symmetry elements of the parent crystallographic group. This enables magnetic structures to be denoted by irreducible representations (irreps) of the crystallographic group. Regarding the space group of $D_{2h}^{16} - Pbnm$ for $RFeO_3$, the crystallographic point group is *mmm*, which is specified by the character table to possess eight one-dimensional irreps. Eight types of magnetic configurations (or magnetic phases), labeled by $\Gamma_1 - \Gamma_8$, can therefore appear. Table 1 displays the transformation properties of each phase under all 16 classical symmetry operations of the parent group[78], where "+" ("−") indicates that the structure transforms symmetrically (antisymmetrically) under an operation. The configurations $\Gamma_1 - \Gamma_8$ have one-to-one correspondence with magnetic groups under Shubnikov's classification, which are displayed in Table 1 as well. Note that this principle of one-to-one correspondence between magnetic point groups and one-dimensional irreducible unitary representations is generic.

The advantage of representation theory in classifying magnetic structures is the ease with which one can derive basis functions. These functions are written in terms of spin components that transform in the same way as an irrep, and therefore, they give the allowed magnetic modes for a magnetic phase. For the four Fe^{3+} atoms located in $4(b)$ sites, whose spins are labled by $\boldsymbol{S}_i$ (i = 1−4), the basis functions can be well described by the following four vector components:

$$\begin{aligned} \boldsymbol{F} &= \boldsymbol{S}_1 + \boldsymbol{S}_2 + \boldsymbol{S}_3 + \boldsymbol{S}_4, \\ \boldsymbol{G} &= \boldsymbol{S}_1 - \boldsymbol{S}_2 + \boldsymbol{S}_3 - \boldsymbol{S}_4, \\ \boldsymbol{A} &= \boldsymbol{S}_1 - \boldsymbol{S}_2 - \boldsymbol{S}_3 + \boldsymbol{S}_4, \\ \boldsymbol{C} &= \boldsymbol{S}_1 + \boldsymbol{S}_2 - \boldsymbol{S}_3 - \boldsymbol{S}_4, \end{aligned} \tag{1}$$

where $\boldsymbol{F}$ represents the net moment contributed by all four spins in the unit cell, and $\boldsymbol{G}$, $\boldsymbol{A}$, and $\boldsymbol{C}$ correspond to three types of AFM ordering, distinguished by different ordering wave vectors. Table 1 contains information on which vector components can be basis functions of each irrep. For instance, the fact that $G_xA_yF_z$ ($F_xC_yG_z$) transforms in the same way as the Γ_4 (Γ_2) irrep indicates that the x component of $\boldsymbol{G}$ ($\boldsymbol{F}$), the y component of $\boldsymbol{A}$ ($\boldsymbol{C}$), and the z component of $\boldsymbol{F}$ ($\boldsymbol{G}$) can be nonzero in the Γ_4 (Γ_2) phase. A visualization of $\boldsymbol{S}_i$ vectors, $\boldsymbol{F}$ and $\boldsymbol{G}$ modes, and spin arrangements in Γ_4 and Γ_2 phases is shown later in Fig. 8.

One may notice from Table 1 that the $\Gamma_1 - \Gamma_4$ phases preserve inversion symmetry, while the $\Gamma_5 - \Gamma_8$ phases do not possess inversion symmetry; this can be read from the transformation properties of irreps on the row labeled by the inversion operator "i." While three Fe^{3+} spin components can be finite for the $\Gamma_1 - \Gamma_4$ phases, there is no Fe^{3+} component that can be consistent with $\Gamma_5 - \Gamma_8$. This is because the $4(b)$ sites (that Fe^{3+} ions occupy) are inversion centers, and the inversion operator would not be able to flip spins on these sites. Instead, i-broken phases have to be generated by magnetic ordering of R^{3+} ions. Located on $4(c)$ sites, rare-earth ions may develop certain spin structures that are allowed in the $\Gamma_5 - \Gamma_8$ configurations. Defining four vectors $\boldsymbol{f}$, $\boldsymbol{g}$, $\boldsymbol{a}$, and $\boldsymbol{c}$ based on the four R^{3+} spins $\boldsymbol{R}_i$ (i = 1−4) in a unit cell as

[1]We do notice that a small number of papers in the literature have used the *Pnma* setting, but here we follow the main convention of using the *Pbnm* setting (equivalent upon an axis rotation).

Table 1 Magnetic Phases in $RFeO_3$ Denoted by Irreducible Representations (irreps)[78][a].

Bertaut's notation	Γ_1	Γ_2	Γ_3	Γ_4	Γ_5	Γ_6	Γ_7	Γ_8
Magnetic group	*mmm*	*mmm*	*mmm*	*mmm*	*mmm*	*mmm*	*mmm*	*mmm*
Fe^{3+} basis	$A_xG_yC_z$	$F_xC_yG_z$	$C_xF_yA_z$	$G_xA_yF_z$				
R^{3+} basis	c_z	f_xc_y	c_xf_y	f_z	g_xa_y	a_z	g_z	a_xg_y
E	+	+	+	+	+	+	+	+
C_{2x}	+	+	−	−	+	+	−	−
C_{2y}	+	−	+	−	+	−	+	−
C_{2z}	+	−	−	+	+	−	−	+
i	+	+	+	+	−	−	−	−
$i\,C_{2x}$	+	+	−	−	−	−	+	+
$i\,C_{2y}$	+	−	+	−	−	+	−	+
$i\,C_{2z}$	+	−	−	+	−	+	+	−
R	−	−	−	−	−	−	−	−
RC_{2x}	−	−	+	+	−	−	+	+
RC_{2y}	−	+	−	+	−	+	−	+
RC_{2z}	−	+	+	−	−	+	+	−
iR	−	−	−	−	+	+	+	+
iRC_{2x}	−	−	+	+	+	+	−	−
iRC_{2y}	−	+	−	+	+	−	+	−
iRC_{2z}	−	+	+	−	+	−	−	+

[a]Each phase has an equivalent magnetic group using Shubnikov's conventions. Magnetic modes (basis functions) allowed in each irrep are given in vectors defined in Eqs. (1) and (2). Transformation properties for each irrep under all point-group symmetry elements of *mmm* are given in "+" (symmetric) and "–" (antisymmetric). E: identity operation. C_{2j} ($j = x, y, z$): two-fold rotation about axis j. i: spatial inversion. R: time inversion.

$$\begin{aligned}\boldsymbol{f} &= \boldsymbol{R}_1 + \boldsymbol{R}_2 + \boldsymbol{R}_3 + \boldsymbol{R}_4,\\ \boldsymbol{g} &= \boldsymbol{R}_1 - \boldsymbol{R}_2 + \boldsymbol{R}_3 - \boldsymbol{R}_4,\\ \boldsymbol{a} &= \boldsymbol{R}_1 - \boldsymbol{R}_2 - \boldsymbol{R}_3 + \boldsymbol{R}_4,\\ \boldsymbol{c} &= \boldsymbol{R}_1 + \boldsymbol{R}_2 - \boldsymbol{R}_3 - \boldsymbol{R}_4\end{aligned} \tag{2}$$

enables writing these components in a compact way, as shown in Table 1.

The discussions on the group theory classifications given so far are abstract, but we can now proceed to place them in a concrete context by reading the diagram of the $RFeO_3$ family, the latest version of which was summarized by Li *et al.*[79] in 2019. Figure 3 shows the temperature-dependent magnetic phases of $RFeO_3$ for R = La to Lu (atomic numbers: 57–71) and Y (atomic number: 39); no data are available for R = Pm due to its radioactivity.

For all crystals, the magnetic ordering of Fe^{3+} sets within the temperature range of 620–740 K to form the Γ_4 phase, featuring AFM ordering along the x and y axes (G_xA_y) and a weak net moment along the z axis (F_z). The net moment is produced by a small spin canting (canting angle ~8.5 mrad) arising from the Dzyaloshinskii–Moriya (DM) interaction. For magnetically inert rare-earth ions, $R^{3+} = La^{3+}$, Eu^{3+}, Lu^{3+}, and Y^{3+}, the Γ_4 phase persists down to the lowest temperature.

Magnetic phase transitions arise, however, in crystals where the R^{3+} ions are magnetically active and therefore can interact with the Fe^{3+} spins[80,81]. The transition with the most frequent occurrence is the $\Gamma_4 \rightarrow \Gamma_2$ spin-reorientation transition (SRT) with decreasing temperature, during which the spin structure continuously rotates within the x–z plane while its relative angles remain rigid; the transition is of finite width in temperature, and within the intermediate temperature range, components of the Γ_4 phase ($G_xA_yF_z$) superimpose on those of the Γ_2 phase ($F_xC_yG_z$), producing the Γ_{24} phase. Crystals with R = Pr, Nd, Sm, Er, Tm, and Yb show this transition, among which $SmFeO_3$ has a transition temperature high enough to make itself the only crystal to exhibit the Γ_2 phase at room temperature. In addition to the continuous-type $\Gamma_4 \rightarrow \Gamma_2$ SRT, there is an abrupt-type $\Gamma_4 \rightarrow \Gamma_1$ SRT observed first in $DyFeO_3$[82,83] (at 50 K) and later in $CeFeO_3$[84,85] (at 240 K). Since the magnetic modes of $A_xG_yC_z$ allowed in the low-temperature Γ_1 phase do not possess a net moment ($\boldsymbol{F} = 0$), a sharp decrease of magnetization has been observed across the transition. Moreover, $HoFeO_3$ adopts a more complicated sequence of SRTs as $\Gamma_4 \rightarrow \Gamma_{24} \rightarrow \Gamma_{12} \rightarrow \Gamma_2$[86–89], featuring an intermediate temperature range within which two metastable configurations, Γ_{24} and Γ_{12}, coexist.

Magnetic interactions between R^{3+} and Fe^{3+} not only lead to assorted SRTs of the Fe^{3+} spin configuration, but also cause R^{3+} to be polarized by the exchange field supplied by the Fe^{3+} sublattice. When R^{3+} is paramagnetic, its polarization is always consistent with the irrep that describes the Fe^{3+} spin structure. For instance, in the Γ_4 and Γ_2 phases, where Fe^{3+} spins have a net moment, the R^{3+} spins will also develop a polarized net moment that is either parallel or antiparallel to the Fe^{3+} magnetization. These are labeled "+" (parallel) and "−" (antiparallel) in Fig. 3, respectively. For those crystals that have antiparallel alignments (R = Nd, Sm, Er, and Tm), the strong temperature dependence of the R^{3+} moment leads to a compensation point[90], that is, a temperature at which the R^{3+} net moment exactly cancels the Fe^{3+} moment.

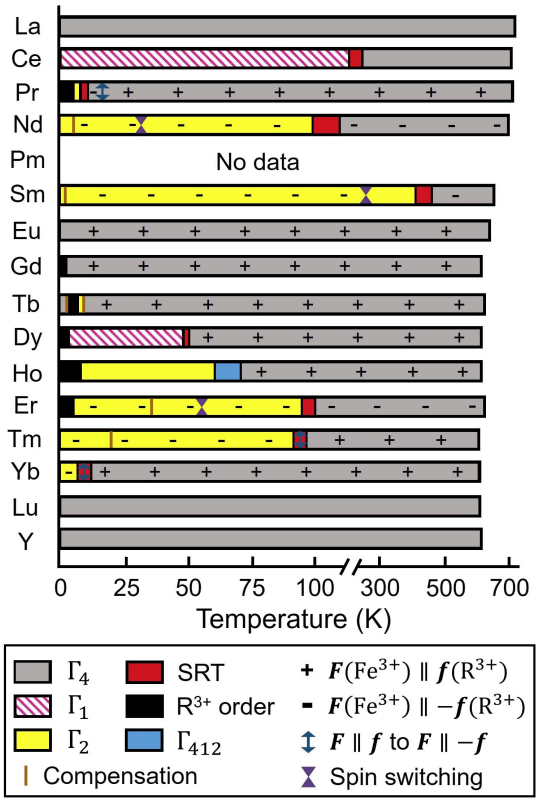

Fig. 3 Temperature-dependent magnetic phase diagrams for all members of the $RFeO_3$ class[79], except for R = Pm, for which no data are available due to its radioactivity. SRT, spin reorientation transition. Reproduced with permission from Ref. [79].

At even lower temperatures, typically below 10 K, R^{3+} develops ordering for R = Pr, Gd, Tb, Dy, Ho, and Er. This creates an interesting situation because the R^{3+} order parameter does not have to be compatible with the Fe^{3+} phase, leading to further symmetry breaking. For $ErFeO_3$, Er^{3+} spins develop a c_z mode when they order, and according to Table 1, the c_z mode transforms according to the Γ_1 irrep, which is different from the Γ_2 phase of the Fe^{3+} spins (before the transition occurs). The low-temperature magnetic phase of $ErFeO_3$ is therefore a Γ_{12} phase[91,92], whose magnetic group ($2m$) is an index-two subgroup of either Γ_1 (mmm) or Γ_2 ($\underline{mm}m$). More interesting physics occur when R^{3+} ordering transforms with an inversion-symmetry-breaking representation Γ_j with $j \in \{5, 6, 7, 8\}$; the resultant phase that takes both Fe^{3+} and R^{3+} into account would be Γ_{ij} with $i \in \{1, 2, 3, 4\}$ and $j \in \{5, 6, 7, 8\}$, which is a noncentrosymmetric phase capable of exhibiting appealing properties that would otherwise be forbidden in centrosymmetric groups. The low-temperature phases of $GdFeO_3$, $DyFeO_3$, and $TbFeO_3$ fall into this category. Their details will be covered in Subsection 3.3 while discussing magneto-electric effects, multiferroicity, and electromagnons.

A variety of experimental methods have been applied to the $RFeO_3$ family in the last century to characterize their magnetic, electronic, and optical properties. Once a crystal is grown, X-ray scattering and Laue diffraction measurements are typically carried out first to examine the crystal quality[93]. After that, the most straightforward method to study magnetic phase transitions is magnetization measurements. Since the Γ_1, Γ_2, and Γ_4 phases are distinguished by their magnitude and orientation of the net moment, an SRT can be readily identified in magnetization curves. Figure 4(a) shows representative temperature-dependent magnetization curves for $LuFeO_3$, $ErFeO_3$, and $DyFeO_3$[75]. In $LuFeO_3$, the Γ_4 phase persists through the entire range below the Néel temperature of Fe^{3+}, which manifests as a finite but nearly temperature-independent z-axis magnetization. Upon cooling, the continuous-type $\Gamma_4 \rightarrow \Gamma_2$ SRT in $ErFeO_3$ induces a finite x-axis magnetization at the expense of z-axis magnetization between 80 K and 100 K. The compensation behavior caused by antiparallel moment alignment between Er^{3+} and Fe^{3+} in the Γ_2 phase manifests as a temperature point (45 K) with zero x-axis magnetization. In $DyFeO_3$, the z-axis magnetization diminishes to zero when the abrupt-type $\Gamma_4 \rightarrow \Gamma_1$ initiates, in agreement with the fact that the Γ_1 phase is incompatible with any net moment. The more complicated multistage SRT in $HoFeO_3$ does not show salient features in magnetization that can be distinguished from the SRT in $ErFeO_3$, but Young's modulus and magnetostriction measurements[86] are able to capture the detailed features. The R^{3+}-ordered phases typically appear as anomalies on magnetization curves at low temperatures[82], but scattering experiments[92,97] are certainly more advantageous to precisely determine the magnetic structure.

Regarding the electronic properties, all crystals within the $RFeO_3$ family are categorized as charge-transfer insulators, rather than Mott insulators, under the framework developed by Zaanen, Sawatsky, and Allen[98,99]. This means that the charge gap is governed by the energy difference between the p bands of oxygen anions and the unoccupied upper Hubbard band of Fe^{3+}; the assignment is also corroborated by density functional theory (DFT) computations[100]. To describe charge excitations more clearly, Fig. 4(b) shows an optical absorption spectrum for an $ErFeO_3$ crystal[94]; other crystals within the same family share much similarity. Intense absorption bands are seen on both sides of a transparent window (1.3 μm to 8 μm). On the short wavelength side, the peaks centered at 1.1 μm, 0.7 μm, and 0.5 μm arise from the $^6A_1 \rightarrow {}^4T_1$, $^6A_1 \rightarrow {}^4T_2$, and $^6A_1 \rightarrow {}^4E + {}^4A$ transitions of Fe^{3+}, respectively. Giant absorption is present for wavelengths shorter than 0.5 μm, and is assigned to the charge-transfer transition from oxygen to Fe^{3+}[101]. Within the transparent window, an absorption band centered at 1.5 μm is identified to be excitations across spin–orbit coupled atomic states of Er^{3+} ($^4I_{15/2} \rightarrow {}^4I_{13/2}$). For longer wavelengths, the absorption coefficient onsets starting from 8 μm are due to infrared (IR)-active phonon excitations. Among the 60 phonon modes, 24 are Raman-active and 36 are IR-active. Although computations reveal the eigen-modes and frequencies of all IR-active phonons[102], many of them remain unobserved except for the Fe-O bond stretching mode at around 18 μm[103]. On the other hand, Raman-active phonons are much better characterized experimentally[104,105], showing excellent agreement with theory.

Finally, we discuss magnetic excitations that can be developed on top of the magnetic ground states of $RFeO_3$, whose understanding is crucial for the major topic of this review paper, i.e., THz spin dynamics. Within a unit cell that consists of four Fe^{3+} and four R^{3+} ions, we focus on a simple model where R^{3+} is assumed to be paramagnetic. This means that magnetic excitations majorly involve Fe^{3+}; cooperative magnetic excitations involving both R^{3+} and Fe^{3+} in the low-temperature R^{3+}-ordered phase are, to date, still an active topic. Shapiro *et al.*[95] used inelastic neutron scattering measurements to map out the dispersion relations of spin waves, and observed an optical

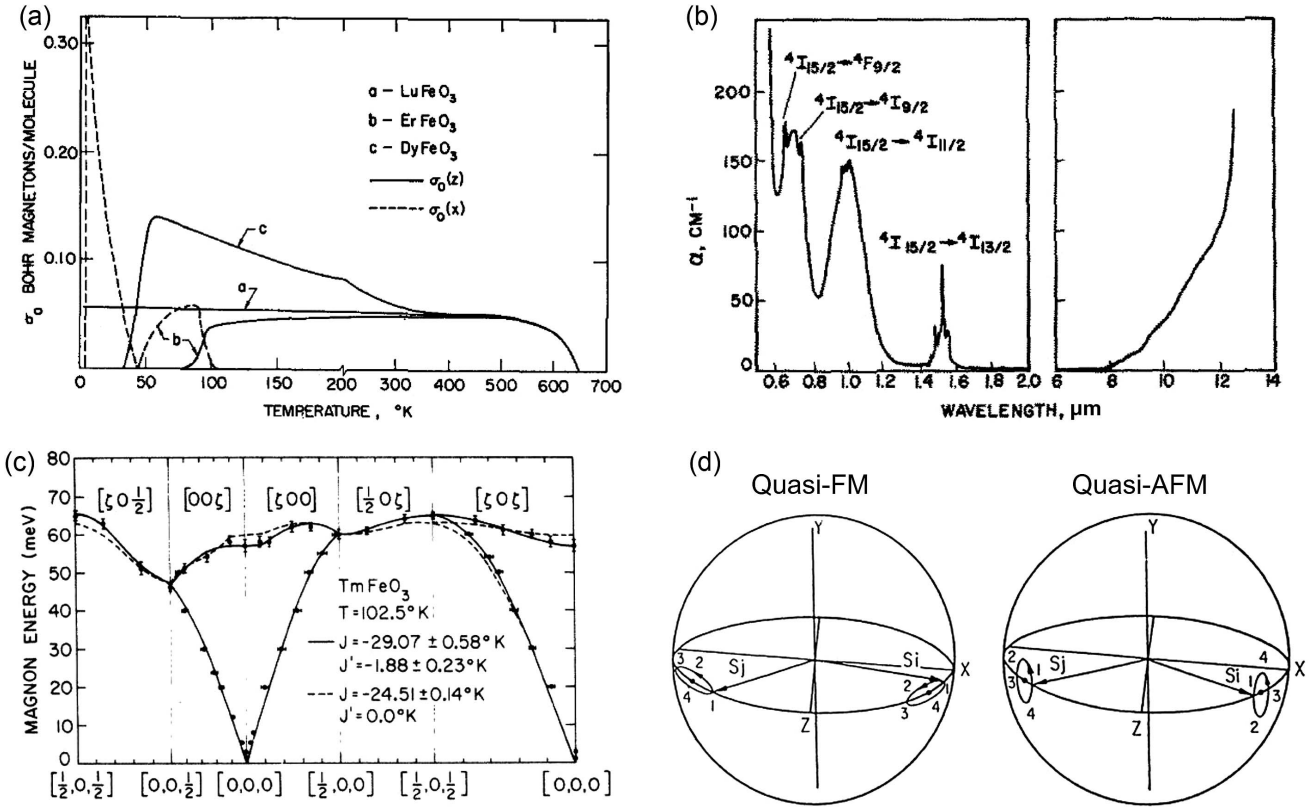

Fig. 4 Basic physical properties of $RFeO_3$ crystals. (a) Temperature-dependent magnetization of $LuFeO_3$, $ErFeO_3$, and $DyFeO_3$ along the z axis and x axis[75]. (b) Optical absorption spectrum of $ErFeO_3$[94]. (c) Spin-wave dispersion mapped by inelastic neutron scattering[95]. (d) Spin oscillations in quasi-FM and quasi-AFM modes[96]. Each spin evolves in the sequence of $1 \rightarrow 2 \rightarrow 3 \rightarrow 4 \rightarrow 1\ldots$. Spins are synchronized by the number label. Reproduced with permission from Refs. [75,94–96].

magnon branch appearing in the energy range from 50 to 70 meV, as shown in Fig. 4(c). This is the exchange mode of Fe^{3+} in the four-sublattice description. Focusing on the high-energy sector, an isotropic Heisenberg Hamiltonian including both the nearest neighbor (J) and next-nearest neighbor (J') fits this branch well, enabling quantitative extraction of J and J'[106].

On the other hand, an acoustic magnon branch, which softens to a near-zero (not exact zero) frequency when approaching the zone center, also appears. In an attempt to accurately describe this branch, especially its low-energy behavior at the zone center, Herrmann[107,108] developed a two-sublattice model, where sublattices A and B arise from the original four Fe^{3+} ions in a unit cell as

$$\boldsymbol{S}^A = \boldsymbol{S}_1 + \boldsymbol{S}_3,$$
$$\boldsymbol{S}^B = \boldsymbol{S}_2 + \boldsymbol{S}_4. \tag{3}$$

This way, the C-type AFM component in Eq. (1) is canceled ($\boldsymbol{C} = 0$), maintaining the G-type AFM and the net moment that can describe the SRTs. The spin Hamiltonian reads

$$H = J_{\mathrm{Fe}} \sum_{\mathrm{n.n}} \hat{\boldsymbol{S}}_i^A \cdot \hat{\boldsymbol{S}}_{i'}^B - D_y^{\mathrm{Fe}} \sum_{\mathrm{n.n}} (\hat{S}_{i,z}^A \hat{S}_{i',x}^B - \hat{S}_{i',z}^B \hat{S}_{i,x}^A) - \sum_{s=A,B} \sum_i [A_x (\hat{S}_{i,x}^s)^2 + A_z (\hat{S}_{i,z}^s)^2 + A_{xz} \hat{S}_{i,x}^s \hat{S}_{i,z}^s], \tag{4}$$

where the first, second, and third terms are isotropic exchange interaction, DM interaction, and magnetic anisotropy, respectively. The isotropic exchange J_{Fe} is the dominant energy scale, stipulating the G-type AFM structure $\boldsymbol{G} = \boldsymbol{S}^A - \boldsymbol{S}^B$; the DM interaction provides spin canting that produces the net moment $\boldsymbol{F} = \boldsymbol{S}^A + \boldsymbol{S}^B$; and the anisotropy energies, A_x and A_z, specify the orientations of the $\boldsymbol{F}$ and $\boldsymbol{G}$ vectors with respect to the crystal axis. The equilibrium configuration determined by Eq. (4) is the Γ_4 (Γ_2) phase, with $\boldsymbol{G} \| x$, $\boldsymbol{F} \| z$ ($\boldsymbol{G} \| z$, $\boldsymbol{F} \| x$), when $A_x > A_z$ ($A_z > A_x$).

The anisotropy terms are precisely the cause of gaps in the acoustic magnon branch (which is usually considered to be gapless in analogy to acoustic phonons) at the zone center in the inelastic neutron spectra. Indeed, an equation of motion calculation using Eq. (4) gives two magnon modes[107,108], named quasi-ferromagnetic (quasi-FM) and quasi-AFM modes, respectively, at

$$\hbar\omega_{\mathrm{FM}} = \{24 J_{\mathrm{Fe}} S^2 [2(A_x - A_z)]\}^{1/2},$$
$$\hbar\omega_{\mathrm{AFM}} = \{24 J_{\mathrm{Fe}} S [6 D_{\mathrm{Fe}} S \tan\beta + 2 A_x S]\}^{1/2}, \tag{5}$$

where $S = 5/2$ is the spin quantum number of Fe^{3+}, and β is the canting angle. The spin trajectories of these modes are shown in Fig. 4(d)[96]. The quasi-FM mode features the precession of the $\boldsymbol{F}$ vector where the relative angle between the two sublattices remains fixed. On the other hand, the quasi-AFM mode periodically modifies the canting angle, but the $\boldsymbol{F}$ vector remains

pointing along its equilibrium orientation, with its amplitude oscillating in time.

Equation (5) provides an important clue for the underlying driving force of a $\Gamma_4 \rightarrow \Gamma_2$ SRT, by showing that $\hbar\omega_{\rm FM} \rightarrow 0$ when $A_x - A_z \rightarrow 0$. Across a $\Gamma_4 \rightarrow \Gamma_2$ SRT, anisotropy switches from $A_x > A_z$ to $A_z > A_x$, and the critical softening of the quasi-FM mode that evolves hand in hand with the anisotropy energy drives the phase transition. The quasi-FM and quasi-AFM modes at the zone center are excitable by both neutron scattering and Raman scattering, so their frequencies have been well studied since early days[95,96,109–111]. Softening of the quasi-FM frequency across a $\Gamma_4 \rightarrow \Gamma_2$ SRT has indeed been observed. On the contrary, the SRT in $DyFeO_3$ is accompanied by softening of the quasi-AFM mode[96].

The quasi-FM and quasi-AFM modes are key players in the THz spintronic studies of $RFeO_3$ materials. In addition to having finite neutron and light scattering cross sections, group theory analysis also stipulates that they also respond linearly to THz-frequency light radiation through the magnetic–dipolar interaction[109]. Section 3 delineates various types of THz probes of magnon modes. In the next subsection, we introduce the major ultrafast optical techniques that enable these studies.

2.2 Ultrafast Optical Techniques for Probing THz Spin Dynamics

The study of interaction between light and spins has a long history. In recent years, however, the advancements of ultrafast laser spectroscopy technologies have redefined the way to investigate THz-frequency spin phenomena. Reconstruction of magnetic dynamics occurring in a material system in real time can be readily implemented by a stroboscopic pump–probe experimental setup. The sample is first excited by a pump pulse, and analysis of the probe pulse that arrives at the sample at a variable time delay enables one to infer the evolution of the excited state of the sample. Since the THz frequency range has time scales of the order of ps, the fs-scale pulse widths provided by current ultrafast lasers provide enough temporal resolution.

In this subsection, we review two major types of ultrafast optical techniques for THz studies of spin dynamics. The first is time-resolved photomagnetic/magneto-optical spectroscopy, which is essentially Faraday/Kerr rotation measurements[112] using pulsed lasers (as opposed to continuous-wave lasers used in earlier studies), and configures a pump–probe time delay to provide time resolution. Owing to the simplicity of envisioning its experimental setup, emphasis of discussion will be on the theoretical framework of tensor analysis that provides the predictive power for the experiments. The second is THz time-domain techniques, including THz time-domain spectroscopy, THz emission spectroscopy, and nonlinear THz spectroscopy, which allows driving spins far away from equilibrium. The working principles of these methods and their advantages will be reviewed.

Probe methods based on spin-resolved photoemission[113,114] and X-ray scattering[115–117] possess advantages in ultrafast spintronics for certain compounds. However, for the $RFeO_3$ family that we focus on here, optical techniques present themselves as not only the most suitable but also the easiest approaches.

2.2.1 Photomagnetic/magneto-optical effects

In a material, either the development of magnetic order or the application of an external magnetic field can affect its optical properties in various ways. These processes are generally known as magneto-optical phenomena and have long been applied to the study of magnetism; notable examples are Faraday and Kerr rotations. On the other hand, intense and properly tailored light impinging on a material can directly influence the states and dynamics of spins and actively modify magnetic properties. These processes representing inverse effects of magneto-optical phenomena are generally known as photomagnetic effects. To gain detailed insight into how photomagnetic and magneto-optic effects are categorized and how they are related to each other, one needs to use the tensor description of light–spin interaction, as described below.

When an $RFeO_3$ crystal is illuminated by light with frequency ω, the total Hamiltonian is given by

$$H = H^0 + H^{\rm MO}.$$

Here, H^0 is the general spin Hamiltonian of $RFeO_3$, while $H^{\rm MO}$ arises from light–spin interactions and can be expanded to lowest order in the electric field of light, $\boldsymbol{E}(\omega)$, as[57]

$$\begin{aligned} H^{\rm MO} \approx -[&\varepsilon^0_{ij} E_i(\omega) E^*_j(\omega) + \alpha_{ijk} E_i(\omega) E^*_j(\omega) F_k(0) \\ &+ \alpha'_{ijk} E_i(\omega) E^*_j(\omega) G_k(0) + \beta_{ijkl} E_i(\omega) E^*_j(\omega) F_k(0) F_l(0) \\ &+ \beta'_{ijkl} E_i(\omega) E^*_j(\omega) G_k(0) G_l(0) \\ &+ \beta''_{ijkl} E_i(\omega) E^*_j(\omega) F_k(0) G_l(0)], \end{aligned} \tag{6}$$

where $\boldsymbol{F} = \boldsymbol{S}^A + \boldsymbol{S}^B$ and $\boldsymbol{G} = \boldsymbol{S}^A - \boldsymbol{S}^B$ are FM and AFM vectors [Eqs. (1) and (3)], respectively, ε^0_{ij}, α_{ijk}, α'_{ijk}, β_{ijkl}, β'_{ijkl}, β''_{ijkl} are tensor coefficients, and the Einstein summation rule is implied (and throughout this paper).

The permittivity tensor, which governs the optical property, then reads

$$\varepsilon_{ij} = -\frac{\partial^2 H}{\partial E_i(\omega) \partial E^*_j(\omega)} = -\frac{\partial^2 H^{\rm MO}}{\partial E_i(\omega) \partial E^*_j(\omega)}, \tag{7}$$

and one can see that all terms in Eq. (6) except for the first term led by ε^0_{ij} are related to magnetism. According to the Onsager principle, the total permittivity tensor can be separated into two parts, $\varepsilon_{ij} = \varepsilon^s_{ij} + \varepsilon^a_{ij}$, where the symmetric part $\varepsilon^s_{ij} = \varepsilon^s_{ji}$ and the antisymmetric part $\varepsilon^a_{ij} = -\varepsilon^a_{ji}$ are even and odd under time reversal, respectively. Since $\boldsymbol{F}$ ($\boldsymbol{F}^2$) and $\boldsymbol{G}$ ($\boldsymbol{G}^2$) are odd (even) under time reversal, the terms that contribute to the total Hamiltonian in Eq. (6) can be categorized based on whether it gives rise to either ε^s_{ij} or ε^a_{ij}. These are given in Table 2.

The property tensors α_{ijk} and α'_{ijk}, both giving rise to the asymmetric part, ε^a_{ij}, contribute only to the off-diagonal elements of the ε_{ij} tensor ($\varepsilon^a_{ii} = 0$). This leads to the eigen-vector of light to take a circularly polarized basis in the medium, giving rise to magnetic circular birefringence, commonly observed as Faraday or Kerr rotations, and magnetic circular dichroism. The proportionality between ε^a_{ij} and $\boldsymbol{F}$ (or $\boldsymbol{G}$) dictates a sign change of these effects upon spin reversal. On the other hand, β_{ijkl}, β'_{ijkl}, and β''_{ijkl} contribute to the symmetric part ε^s_{ij}, which is able to take the diagonal components within ε_{ij}. The associated magneto-optical effects manifest in the linearly polarized basis—i.e., magnetic linear birefringence (Cotton–Mouton effect) and magnetic linear dichroism—and do not change sign upon spin reversal.

Table 2 Property Tensors, Their Contributions to the Hamiltonian, and Their Resulting Magneto-Optical and Photomagnetic Effects[57][a].

Property Tensor	Contribution to H^{MO}	Magneto-Optical Effects		Photomagnetic Effects	
α_{ijk} (axial, *i*)	$\alpha_{ijk}E_iE_j^*F_k$	$\varepsilon_{ij}^a = \alpha_{ijk}F_k$	Magnetic circular birefringence (Faraday/Kerr rotation), magnetic circular dichroism	$H_k^{PM} = \alpha_{ijk}E_iE_j^*$	Inverse Faraday effect
α'_{ijk} (axial, *i*)	$\alpha'_{ijk}E_iE_j^*G_k$	$\varepsilon_{ij}^a = \alpha'_{ijk}G_k$		$h_k^{PM} = \alpha'_{ijk}E_iE_j^*$	
β_{ijkl} (polar, *i*)	$\beta_{ijkl}E_iE_j^*F_kF_l$	$\varepsilon_{ij}^s = \beta_{ijkl}F_kF_l$	Magnetic linear birefringence (Cotton-Mouton effect), magnetic linear dichroism	$H_l^{PM} = \beta_{ijkl}E_iE_j^*F_k$	Inverse Cotton-Mouton effect
β'_{ijkl} (polar, *i*)	$\beta'_{ijkl}E_iE_j^*G_kG_l$	$\varepsilon_{ij}^s = \beta'_{ijkl}G_kG_l$		$h_l^{PM} = \beta'_{ijkl}E_iE_j^*G_k$	
β''_{ijkl} (polar, *i*)	$\beta''_{ijkl}E_iE_j^*F_kG_l$	$\varepsilon_{ij}^s = \beta''_{ijkl}F_kG_l$		$H_k^{PM} = \beta''_{ijkl}E_iE_j^*G_l$ $h_l^{PM} = \beta''_{ijkl}E_iE_j^*F_k$	

[a]Frequencies in parentheses are abbreviated. The electric field $\boldsymbol{E}$ is at frequency ω, while vectors $\boldsymbol{F}$, $\boldsymbol{G}$, and effective fields $\boldsymbol{H}^{PM}$ and $\boldsymbol{h}^{PM}$ are all at zero frequency. Reproduced with permission from Ref. [57].

Photomagnetic effects arise from the same Hamiltonian, Eq. (6), and the influence of the optical field on magnetism can be viewed as effective magnetic fields at zero frequency:

$$\boldsymbol{H}^{PM}(0) = -\frac{\partial H^{MO}}{\partial \boldsymbol{F}(0)},$$
$$\boldsymbol{h}^{PM}(0) = -\frac{\partial H^{MO}}{\partial \boldsymbol{G}(0)}, \tag{8}$$

where $\boldsymbol{H}^{PM}(0)$ and $\boldsymbol{h}^{PM}(0)$ are the effective fields exerted on $\boldsymbol{F}$ and $\boldsymbol{G}$, respectively. Table 2 summarizes various forms of them that are associated with the five property tensors. Most notably, the effective field $H_k^{PM}(0) = \alpha_{ijk}E_i(\omega)E_j^*(\omega)$, which is associated with α_{ijk}, the same tensor that induces the Faraday effect, can be further simplified for isotropic media. Replacing α_{ijk} by the minimal expression of $\alpha \cdot \varepsilon_{ijk}$, where α is a scalar constant and is the Levi–Civita tensor (reflecting the axial nature of α_{ijk}), we obtain the effective field as

$$\boldsymbol{H}^{PM}(0) = \alpha[\boldsymbol{E}(\omega) \times \boldsymbol{E}^*(\omega)], \tag{9}$$

which resembles the form of the inverse Faraday effect (IFE), stating that circularly polarized light imposes an effective magnetic field along its propagation direction on the medium. Following the same logic, effective fields associated with the fourth-rank polar tensors β_{ijkl}, β'_{ijkl}, and β''_{ijkl} can be generated by linearly polarized light, representing the inverse Cotton–Mouton effect (ICME).

If the fields $\boldsymbol{H}^{PM}$ and $\boldsymbol{h}^{PM}$ are generated by a pulsed light field through photomagnetic effects, they will be transient in nature (no longer at zero frequency) and will thus be able to excite coherent magnon oscillations in a way similar to how a THz magnetic field pulse excites magnons though the Zeeman torque. The IFE and ICME have been firmly established in $RFeO_3$ through observation of coherent magnons launched by the laser-induced effective fields. The way to distinguish photomagnetic effects from trivial thermal effects is to see if the phase of coherent magnons can be manipulated by the polarization of pump light. In the case of the IFE, altering the helicity of pump light results in sign reversal of the $\boldsymbol{H}^{PM}$ pulse, and therefore, a 180 deg phase flip in coherent magnons [Fig. 5(a)]. For the ICME, the magnon phase is controlled by the orientation of linear polarization [Fig. 5(b)]. Furthermore, as shown in Fig. 5(c), the general framework that encompasses coherent magnon excitation by the IFE and ICME is the impulsive stimulated Raman scattering (ISRS). The scattering relies on the coexistence of two colors within the light pulse, one at ω and the other at $\omega - \Omega$, Ω being the magnon frequency. The $\omega - \Omega$ component stimulates the inelastic scattering of the ω component to occur, causing it to decompose into another photon at $\omega - \Omega$ and a magnon quantum at Ω.

In realistic situations, making predictions about the outcomes of pump–probe experiments is rather complex. Specifically, the type of photomagnetic effects that can occur for a particular pumping condition, and the probe configuration that can most efficiently detect the spin dynamics by magneto-optical effects, both depend critically on the material of interest. For $RFeO_3$, based on the knowledge in Table 2, Iida *et al.*[119] discussed a useful method to address this problem, which we schematically summarize in Fig. 6.

When one attempts to predict the spin dynamics excited by a photomagnetic pump, one first calculates effective photomagnetic fields from the known static magnetic geometry, property tensors (Table 2) that are simplified by the magnetic point group symmetries, and the eigenvector of the light field. The effective photomagnetic fields, when combined with intrinsic fields derived from the unperturbed Hamiltonian H^0, give the total effective fields (note the time delay dependence of the effective fields due to the transient nature of the pump pulse). The total effective fields can then be used in the Landau–Lifshitz equations to solve for the full time-dependent spin dynamics. After knowing the spin dynamics, one would be interested in detecting them through a magneto-optical probe. This step is easier, as one simply needs to input the time-dependent spin dynamics and the simplified property tensors back into the equation for calculating the optical permittivity tensor (third column in Table 2). The time-dependent optical properties would then be fully determined. Overall, this method is able to provide most qualitative predictions on the pump–probe experiment based on a few symmetry arguments (without resorting to a microscopic model), and is highly efficient and useful.

2.2.2 THz time-domain techniques

Provided that the time-resolved photomagnetic/magneto-optical experiments majorly target at studying Raman-active magnetic excitations, one should seek for a complementary ultrafast optical technique that couples to IR-active spin modes. THz time-domain techniques target such functionality. They encompass a series of experimental methods, all of which utilize pulsed THz

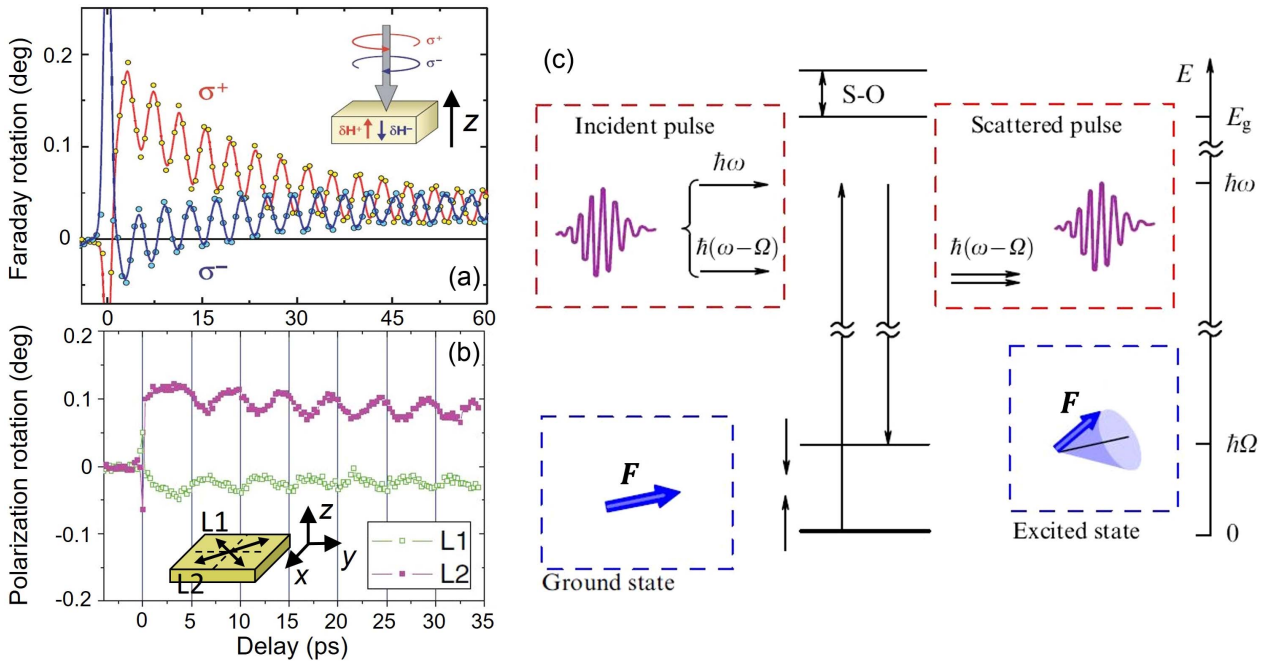

Fig. 5 Observation of (a) the inverse Faraday effect[118] and (b) the inverse Cotton–Mouton effect[119] in $DyFeO_3$. The oscillation phases of magnons excited by these photomagnetic effects depend on the polarization of the pump light. (c) Magnon excitation by the two photomagnetic effects can be described by the framework of impulsive stimulated Raman scattering[57]. Reproduced with permission from Refs. [57,118,119].

radiation to directly couple to the magnetic excitations through the magnetic–dipolar interaction. However, there is an important aspect that makes them more advantageous compared with the magneto-optical probes.

Since the very beginning of ultrafast magnetism studies, there has existed a controversy over whether time-resolved mageto-optical signals faithfully represent magnetic dynamics[120–122]. For instance, one may design a Faraday/Kerr rotation experiment to probe $\boldsymbol{F}$ and $\boldsymbol{G}$ vectors, and the attempt would be successful in an equilibrium situation where the axial tensors α_{ijk} and α'_{ijk} have suitable nonzero components (see Table 2). However, in a non-equilibrium situation where the system is excited by a pump pulse before the arrival of the probe pulse, it is unclear whether the probed Faraday/Kerr rotation originates from the actual magnetic dynamics ($\boldsymbol{F}$ and $\boldsymbol{G}$) or from the dynamics of the tensors α_{ijk} and α'_{ijk}[121,122] (which is only a trivial optical effect unrelated to magnetism). The difficulty with disentangling the two types of possible contributions has led to confusion in interpreting time-resolved magneto-optical data. However, probing spin dynamics using THz time-domain techniques circumvents such complications and therefore is more direct[123].

THz time-domain spectroscopy is a useful technique to reveal fundamental excitations in solids[124–137]. Its most common layout is in transmission geometry, as depicted in Fig. 7(a), although reflection geometry is also often used[139]. A pulsed laser beam is first split by a beam splitter into a strong THz generation beam and a weak probe beam. The THz generation beam, incident on a nonlinear crystal such as ZnTe, generates pulsed THz radiation through a second-order nonlinear process called optical rectification[37]. The nonlinear polarization

$$P_i^{(2)}(\Omega) \propto \chi_{ijk}^{(2)}(\Omega = \omega_2 - \omega_1; \omega_1, -\omega_2) E_j(\omega_1) E_k^*(\omega_2) \tag{10}$$

gives rise to a radiation field $\boldsymbol{E}_{\mathrm{THz}}(t) \propto \partial^2 \boldsymbol{P}^{(2)}(t)/\partial t^2$. The phase-matching condition requires the phase velocity of the generated THz pulse to match the group velocity of the generation pulse:

$$v_{\mathrm{THz}}^{\mathrm{ph}} = v_{\mathrm{opt}}^{\mathrm{gr}}. \tag{11}$$

The THz beam is then collimated and focused onto a sample using a pair of off-axis parabolic mirrors. The THz pulse interacts with the sample by resonantly coupling to its excitations. The transmitted (reflected) wave is then collected and focused onto another piece of nonlinear detection crystal. Electro-optic sampling is carried out by the time-delayed probe pulse that is directed to the same detection crystal, achieving spatial and temporal overlap with the THz pulse. When the THz pulse and the probe pulse co-propagate in the detection crystal, a polarization modulation is induced on the probe pulse, depending on the amplitude and sign of the THz electric field[36]. The modulation is analyzed by a polarization-sensitive differential detection scheme [depicted as a zoom-in view in Fig. 7(b)] as a function of probe time delay, mapping out the complete THz electric field waveform in time.

Far-IR spectroscopy techniques using continuous-wave light sources preceded the advent of THz time-domain spectroscopy and have been applied to $RFeO_3$ crystals to provide crucial insights into their magnetic properties[87,140–142]. However, the phase resolution unique to THz time-domain techniques enables precise extraction of Kramers–Kronig compatible real and imaginary parts of index of refraction. Further, time-domain techniques enable one to observe the free-induction decay of a resonance directly in time. A THz time-domain spectrometer can be easily configured into a THz emission spectroscopy

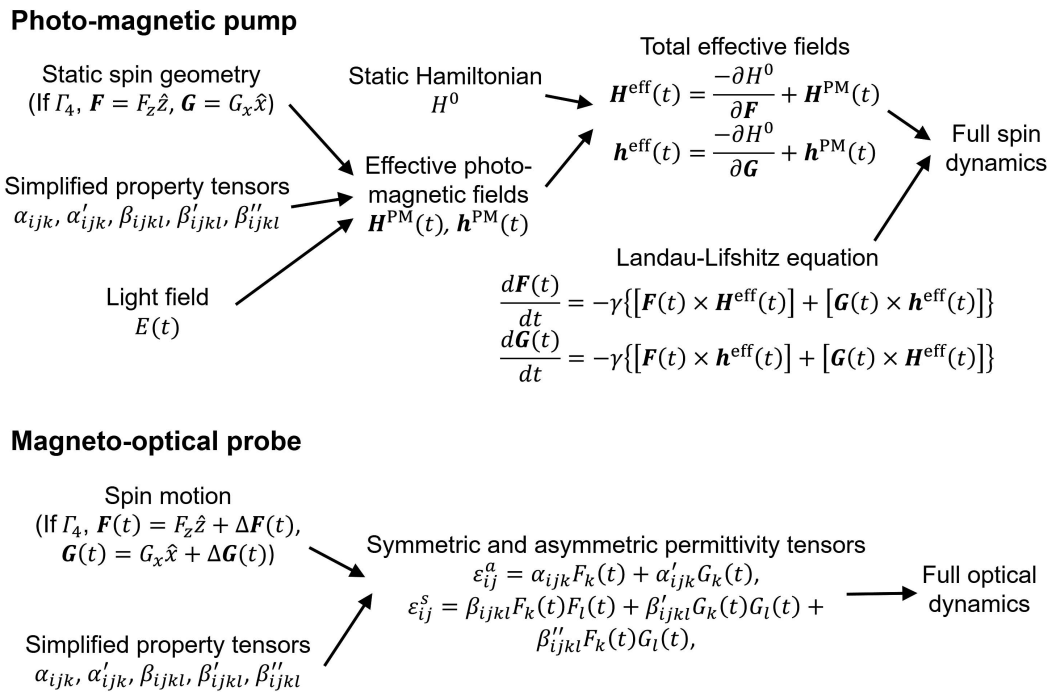

Fig. 6 Path of solving for the full dynamics of photomagnetic pump, magneto-optical probe experiments on $RFeO_3$, summarized from the procedure adopted in Ref. [119].

setup as in Fig. 7(c). Here, the nonlinear crystal for THz generation is removed, and the THz radiation emitted from the sample itself under optical excitation is measured. Emission spectroscopy is useful for investigating quasi-FM and quasi-AFM magnon modes in $RFeO_3$ because these modes can not only be excited by optical pulses through Raman scattering, but also can couple with THz radiation through magnetic-dipole interactions.

As THz time-domain techniques gain increasing popularity in studies of quantum materials, progress is being made currently to incorporate them with extreme experimental conditions such as low temperatures and high magnetic fields. In particular, high magnetic fields can facilitate explorations of exotic quantum properties of materials with high controllability, as has been shown recently using fields up to 30 T[143]. Since such high magnetic fields are typically supplied by pulsed magnets, whose

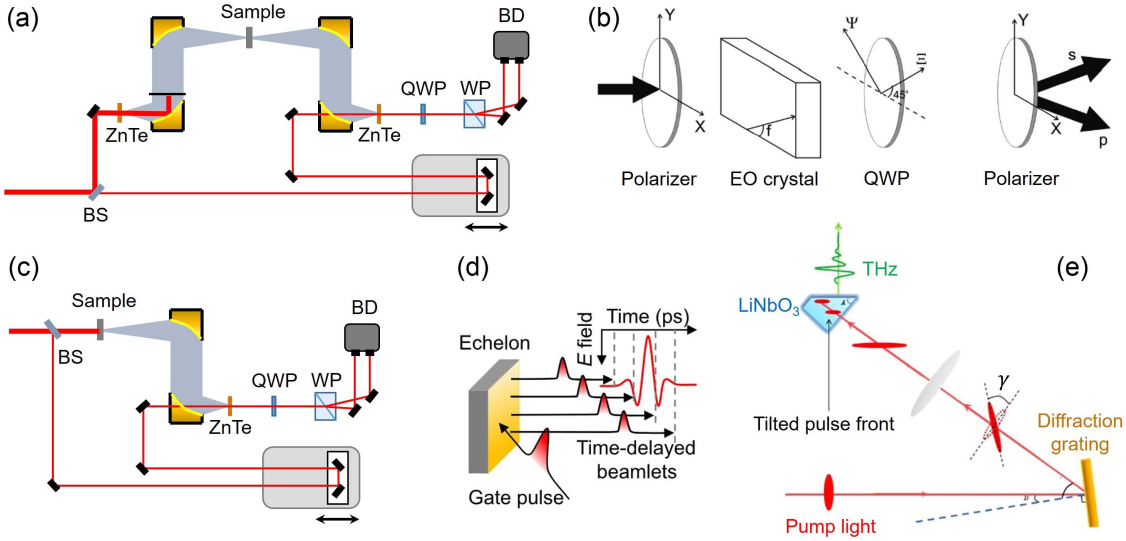

Fig. 7 THz time-domain techniques. (a) Layout of a THz time-domain spectroscopy setup configured in a transmission geometry. (b) Zoom-in view of the polarization-sensitive differential detection setup[36]. (c) Layout of a THz emission spectroscopy setup. (d) Function of a reflective echelon used in a single-shot THz spectrometer[138]. (e) Pulse-front-tilt technique for generating intense THz radiation in $LiNbO_3$[38]. BS, beam splitter; QWP, quarter-wave plate; WP, Wollaston prism; BD, balanced detector. (b), (d), (e) Reproduced with permission from Refs. [36,38,138].

peak fields last for only a short duration of time (~1 ms), conventional electro-optic sampling of THz waveforms by a stage-scan system cannot be used[144]. Nevertheless, single-shot detection schemes have been developed[145], which are capable of measuring the full THz waveform using just one laser pulse within the very short time window during which the sample is experiencing the peak of the pulsed magnetic field. As shown in Fig. 7(d), the key to single-shot detection is to replace the probe delay stage with a reflective echelon mirror[146], which tilts the pulse front of the optical gate beam by forming time-delayed beamlets; the time delay information is therefore encoded in the pulse-front tilt across the intensity profile of the beam. A fast CMOS camera captures the full image of the gate beam, enabling the extraction of THz waveforms at various time delays.

THz time-domain techniques also nurture the nonlinear THz spectroscopy technique[147,148], where peak THz electric fields of the order of MV/cm can be generated, leading to an entirely new class of extreme experimental conditions for out-of-equilibrium engineering of quantum materials[149–154]. Being easily resonant with lattice phonons and magnons, strong THz radiation can selectively drive the lattice and/or spin DOFs of the system far out of equilibrium without strong charge excitations (which is usually a significant source of laser-induced heating). We will see the application of such an apparatus in the study of nonlinear magnonics in Subsection 5.4.

To achieve higher THz electric field strengths in optical rectification, much effort has been expended on increasing the nonlinearity of the generation crystals. However, at the same time, difficulty arises with regard to maintaining the phase-matching condition [Eq. (11)], because of the normal dispersions of nonlinear crystals. A scheme of tilted-pulse-front optical rectification has developed to address this challenge[155–157]. As shown in Fig. 7(e), the generation beam is tilted in wavefront after being diffracted by a high-efficiency grating. If the tilting angle is γ, the phase-matching condition in Eq. (11) can be achieved as

$$v_{\mathrm{THz}}^{\mathrm{ph}} = v_{\mathrm{opt}}^{\mathrm{gr}} \cos \gamma. \tag{12}$$

When implemented in nonlinear crystals such as $LiNbO_3$, this relation suggests that the propagation direction of the generated THz wave is different from that of the optical beam. Strong THz electric fields of the order of MV/cm have been generated based on this scheme.

An increasing number of novel schemes for intense THz generation are being developed currently. There are two important highlights. One is the optical rectification from organic crystals—molecular crystals with gigantic nonlinear coefficients (which can be larger by an order of magnitude than inorganic nonlinear crystals)[158–161]. By tuning the generation beam to appropriate wavelengths, the phase-matching condition can be achieved in collinear geometry. Another novel scheme to note is carrier–envelope-phase stable difference-frequency generation and optical parametric amplification technology[162], which generates phase-locked multi-THz (10–30 THz) radiation with strong intensity[163–166]. The same technique is now being expanded to the mid-IR frequency range[167,168], dramatically enhancing the capability of quantum control of the lattice sector of quantum materials.

3 Probing Equilibrium Properties

This section describes various previous studies where THz spectroscopy techniques were used for probing properties of the $RFeO_3$ family in thermal equilibrium, including phase transitions and elementary excitations. There are two objectives that we wish to achieve by discussing these topics. The first objective is to give concrete examples for which the background knowledge presented in the last section can be put into direct use. We will show how the representation theory in Subsection 2.1 can be used to understand and predict certain THz properties of $RFeO_3$ in equilibrium. The second objective is to lay the foundation for describing the out-of-equilibrium engineering efforts in later sections. Understanding the THz-frequency signatures of thermodynamic phase transitions facilitates the identification of a similar class of transitions achieved in nonequilibrium scenarios. Furthermore, illustrating fundamental excitations on an individual basis will set the stage for investigating their mutual interactions and dynamical couplings, providing necessary insight for the discussion related to ultrastrong coupling (USC) and Dicke cooperativity in Section 6.

We will first consider the temperature- and magnetic-field-induced SRTs in the Fe^{3+} subsystem, particularly the most common $\Gamma_4 \rightarrow \Gamma_2$-type transition. The unique advantage of THz time-domain spectroscopy in detecting these transitions is the ability to simultaneously probe magnons' polarization selection rule, frequency shifts, and spin trajectory, all of which are expected to develop anomalies across an SRT. We will then focus on the R^{3+} ion subsystem, highlighting spectroscopy studies of transitions between their crystal-field levels. These levels, with spacings in the THz range, are the major origin of the strong temperature dependence of magnetic properties in the $RFeO_3$ family. We will consider both non-Kramers-type Tm^{3+} and Kramers-type Er^{3+}. Finally, we will turn to a type of cooperative magnetic excitation that involves both R^{3+} and Fe^{3+} subsystems, called electromagnons, which exist in only a few low-temperature R^{3+} ordered phases where spatial inversion is broken by magnetic order. Observation of these modes not only signals successful detection of these low-temperature R^{3+} ordered phases, but also provides insight into spin-mediated multiferroicity and useful protocols for switching magnetoelectric coupling on/off through magnetic control of spatial inversion symmetry.

3.1 THz Probe of Temperature- and Magnetic-Field-Induced Spin Reorientation Transitions

As shown in Fig. 4(c), the spin-wave dispersion in $RFeO_3$ features high-frequency optical branches corresponding to the exchange mode of the four-sublattice model as well as gapped low-frequency acoustic branches whose properties closely link with magnetic anisotropy. Since SRTs in $RFeO_3$ are mainly driven by magnetic anisotropy, probing these acoustic branches provides much information on the SRTs themselves.

THz radiation couples with zone-center modes of the acoustic branches, which are quasi-FM and quasi-AFM magnon modes [Fig. 4(d)]. These modes respond linearly to THz radiation through the magnetic-dipole interaction[109]. Microscopically, the excitation can be described by a Zeeman-torque-type interaction $\boldsymbol{T}_i = \gamma \boldsymbol{S}_i \times \boldsymbol{H}_{\mathrm{THz}}$, where γ is the gyromagnetic ratio, $\boldsymbol{H}_{\mathrm{THz}}$ is the magnetic field component of the THz pulse, and i = A or B. The sublattice spins $\boldsymbol{S}_A$ and $\boldsymbol{S}_B$ are tipped to deviate from their equilibrium orientations through the Zeeman torque, initiating precessions about their equilibrium axis. The quasi-FM and quasi-AFM modes hold distinct polarization selection rules:

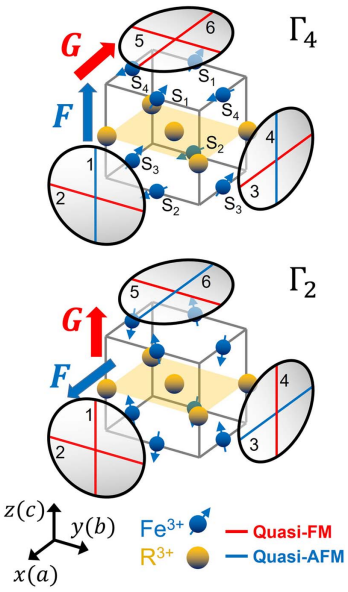

Fig. 8 Six measurement configurations, along with the magnon polarization selection rule in the Γ_4 and Γ_2 phases. The magnetic field component of the THz pulse $\boldsymbol{H}_{\mathrm{THz}}$ is polarized along a line whose color indicates the magnon mode that can be excited. The THz propagation direction is perpendicular to the disk containing the line. Reproduced with permission from Ref. [169].

the quasi-FM mode is excited when $\boldsymbol{H}_{\mathrm{THz}} \perp \boldsymbol{F} = \boldsymbol{S}_A + \boldsymbol{S}_B$, and the quasi-AFM mode is excited when $\boldsymbol{H}_{\mathrm{THz}} \| \boldsymbol{F} = \boldsymbol{S}_A + \boldsymbol{S}_B$.

When an SRT occurs, three major features are expected within the THz time-domain signal of quasi-FM and quasi-AFM modes. First, there is a change in the polarization selection rule that accompanies the direction switching of the $\boldsymbol{F}$ vector. Taking the most common $\Gamma_4 \rightarrow \Gamma_2$ SRT as an example, a total of six measurement configurations are possible for a linearly polarized THz field interacting with a crystal cut along a major axis; see Fig. 8. For each number-labeled configuration, $\boldsymbol{H}_{\mathrm{THz}}$ is polarized along a line (marking a major crystal axis), whose color indicates the magnon mode that can be excited, and the THz pulse propagates along the out-of-plane direction of the disk that contains the colored line. For a given measurement configuration, the mode that can be excited changes across a $\Gamma_4 \rightarrow \Gamma_2$ transition; for instance, configuration 4 would excite the quasi-AFM mode in the Γ_4 phase and the quasi-FM mode in the Γ_2 phase. Second, there is a change of the polarization trajectory of the emitted field of magnons, which reflects the trajectory of spins within the eigenmode. Third, there is a shift of magnon frequency, which is a natural consequence of the fact that the quasi-FM and quasi-AFM frequencies respond sensitively to magnetic anisotropy; see Eq. (5).

Yamaguchi *et al.*[170] have studied the temperature driven $\Gamma_4 \rightarrow \Gamma_2$ SRT in $ErFeO_3$. As shown in Fig. 9(a), when a THz pulse with $\boldsymbol{H}_{\mathrm{THz}} \| x$ transmits through a z-cut crystal, corresponding to configuration 6 in Fig. 8, it excites the quasi-FM mode at 250 K (Γ_4) and switches to excite the quasi-AFM mode at 70 K (Γ_2). When the THz pulse is tailored with $\boldsymbol{H}_{\mathrm{THz}} \| y$ (configuration 5 in Fig. 8), although both Γ_4 and Γ_2 phases support excitation of the quasi-FM mode, their spin precession trajectories are different [Fig. 9(b)]; the oscillations project to a near-circle (elliptical to be exact) pattern to the $x-y$ plane in the Γ_4 phase, but to linear polarization in the Γ_2 phase. This causes different polarization states of the free-induction decay (FID) signal that arises from the magnon precession, which is indeed experimentally detected through polarization-resolved measurement of the emission [Fig. 9(c)]. This experiment thus

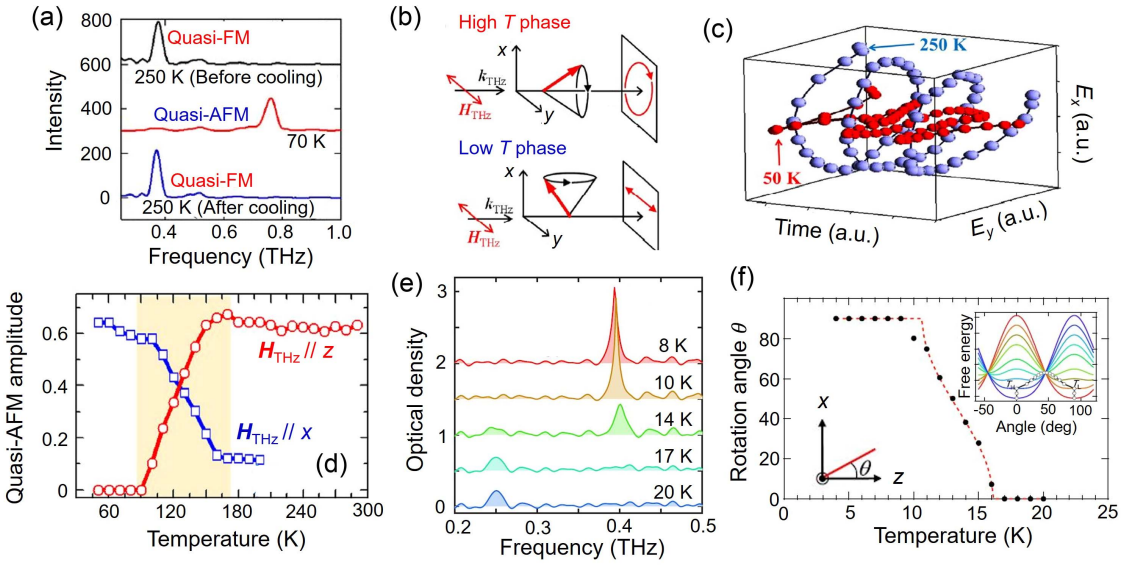

Fig. 9 Temperature-dependent SRT probed by THz spectroscopy[170–172]. (a) Switching of the polarization selection rule. (b) Switching of the polarization trajectory of magnon emission. (c) Experimental verification of (b). (d) Continuous spectral weight transfer between two measurement configurations of the quasi-AFM mode amplitude. (e), (f) Quantifying the rotation angle during the SRT from quasi-AFM to quasi-FM mode spectral weight transfer in z-cut $Dy_{0.7}Er_{0.3}FeO_3$. Inset to (f): calculated free-energy landscape at various temperatures (red to blue: low to high temperatures). Reproduced with permission from Refs. [170–172].

demonstrated a unique usage of the time resolution provided by THz time-domain techniques in measuring the magnon FID, which reconstructs the spin trajectories.

While Yamaguchi *et al.*[170] probed the SRT by studying only two temperature points, one above and the other below the transition temperature, Jiang *et al.*[171] have investigated the SRT temperature range in detail. Within a *y*-cut $NdFeO_3$ crystal, they detected the amplitudes of the quasi-AFM mode for both the $\boldsymbol{H}_{THz}\|z$ configuration (configuration 4 in Fig. 8) and the $\boldsymbol{H}_{THz}\|x$ configuration (configuration 3 in Fig. 8), and plotted them as a function of temperature. Figure 9(d) shows that, within the $\Gamma_4 \rightarrow \Gamma_2$ SRT temperature range, weight transfer between the two configurations occurs in a continuous manner, pointing to the continuous nature of the SRT.

Suemoto *et al.*[172] have brought the analysis to a more quantitative level by calculating the rotation angle of the spin structure in the Γ_{24} phase from the spectral weight transfer. They used a *z*-cut $Dy_{0.7}Er_{0.3}FeO_3$ crystal, and aligned $\boldsymbol{H}_{THz}\|x$ (configuration 6 in Fig. 8). As shown in Fig. 9(e), a continuous-type spectral weight transfer between the quasi-AFM and quasi-FM modes was observed when the temperature was fine-tuned across the SRT. They were able to quantify the rotation angle as

$$\theta = \arctan\left(\sqrt{\frac{A_F}{A_{AF}}}\right), \tag{13}$$

where A_F and A_{AF} are the spectral amplitudes of quasi-FM and quasi-AFM modes, respectively. Figure 9(f) shows the temperature dependence of the rotation angle extracted by this method, which shows excellent agreement with a standard second-order phase transition theory incorporating both second-order and fourth-order anisotropy terms in free energy[173].

In addition to temperature-driven SRTs, THz time-domain techniques have also been used for probing SRTs driven by an external magnetic field. To perform this study, Jiang *et al.*[174] aligned $\boldsymbol{H}_{THz}\|z$ in a *y*-cut $NdFeO_3$ crystal (configuration 4 in Fig. 8). They first demonstrated the polarization selection rule in the temperature-driven SRT. The quasi-AFM mode is detected in the high-temperature Γ_4 phase but not in the low-temperature Γ_2 phase [Fig. 10(a) top]. Then they set the system in the high-temperature Γ_4 phase, and applied a static magnetic field along the *x* axis of the crystal. Since the $\boldsymbol{F}$ vector is prone to align parallel to the static field, a field-driven $\Gamma_4 \rightarrow \Gamma_2$ transition occurs. This again manifests in the polarization selection rule, as shown by the diminishing quasi-AFM mode in the high-field case [Fig. 10(a) bottom].

Based on a similar idea, Lin *et al.*[175] have studied a field-driven $\Gamma_4 \rightarrow \Gamma_2$ transition in $YFeO_3$. Since Y^{3+} is nonmagnetic, a $\Gamma_4 \rightarrow \Gamma_2$ SRT would not occur in the temperature-dependent phase diagram of $YFeO_3$ (Fig. 3). In a *z*-cut $YFeO_3$ crystal, the polarization of the THz radiation is $\boldsymbol{H}_{THz}\|x$ (configuration 6 in Fig. 8), for which only the quasi-FM mode is expected in the zero-field Γ_4 phase. However, when a static magnetic field is applied along the *x* axis, the spin structure will be polarized to approach a $\Gamma_4 \rightarrow \Gamma_2$ transition. Key experimental signatures, including softening of the quasi-FM frequency and increase of the spectral amplitude of the quasi-AFM mode, are observed; see Fig. 10(b). Up to the highest field that is applied (7 T), the quasi-FM mode does not soften completely, suggesting that the transition to the Γ_2 phase is incomplete; this is consistent with prior studies[142,176] that observed the transition at 7.4 T. Nevertheless, a theoretical model taking into account an additional spin-field Zeeman term in the original spin Hamiltonian [Eq. (4)] gives field-dependent magnon frequencies that match the experimental results very well [Fig. 10(c)].

3.2 THz Probe of Crystal-Field Transitions of Rare-Earth Ions

For $RFeO_3$ crystals where R^{3+} ions are magnetically active, the energy levels of R^{3+} are crucial for understanding the overall magnetic properties, even within the temperature range where R^{3+} ions remain paramagnetic. The SRTs, compensation behavior, and spin switching are a few notable examples. R^{3+} ions are typically heavy elements where the spin–orbit interaction is significant enough to form atomic states in free space with

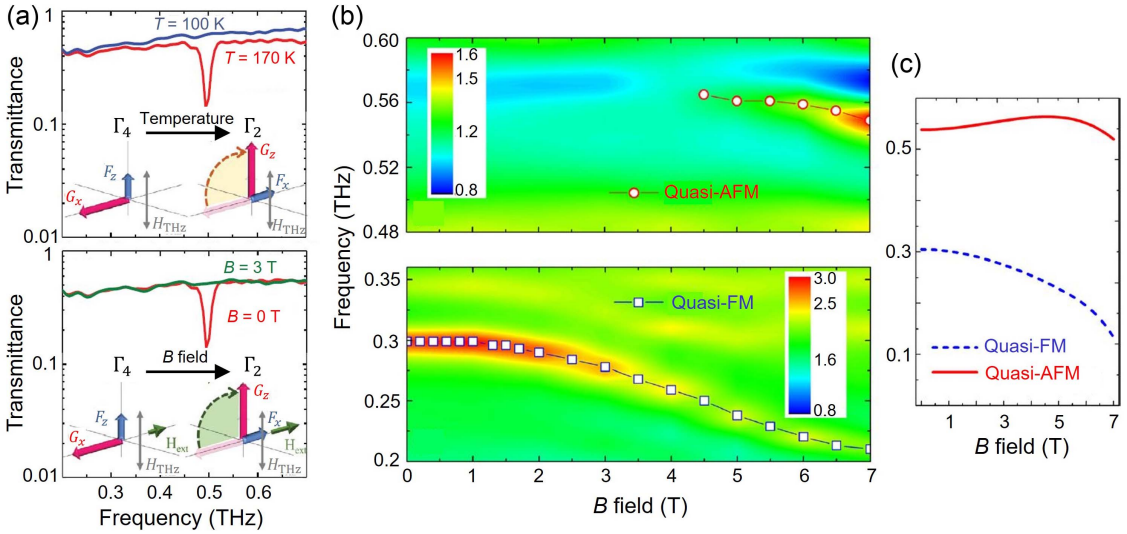

Fig. 10 Magnetic-field-induced $\Gamma_4 \rightarrow \Gamma_2$ SRT probed by THz spectroscopy[174,175]. (a) Observation of switching of the polarization selection rule in $NdFeO_3$. (b) Field-dependent absorption spectra in $YFeO_3$. (c) Calculated quasi-FM and quasi-AFM frequencies versus magnetic field, to compare with (b). Reproduced with permission from Refs. [174,175].

well-defined quantum number J. The confined nature of the $4f$ orbitals stipulates that the crystal electric field acts only as a weak perturbation (weak compared to the spin–orbit interaction) to split these spin–orbit coupled states into crystal-field states (distinguished by the magnetic quantum number m). However, the energy scale of crystal-field splitting is of the same order of magnitude as the thermal energy at a few tens of Kelvin. This is the fundamental reason that the magnetic properties of R^{3+} are sensitive to temperature, which, in turn, leads to the rich temperature-dependent magnetic phase diagrams of the $RFeO_3$ family.

In this subsection, we discuss the use of THz time-domain spectroscopy to study transitions between crystal-field states, known as crystal-field transitions (CFTs), of R^{3+} ions in $RFeO_3$. We will describe how peaks in the absorption spectrum can be assigned to CFTs, whose evolutions with an external magnetic field can be used to quantitatively extract the microscopic parameters of R^{3+} sublattices, and how the polarization dependence of the emitted THz field from CFTs can be used to distinguish the dipolar nature of the transitions. While the highlighted work here all used time-domain techniques, some important early studies used continuous-wave far-IR spectroscopy to study similar transitions[140,177,178].

Zhang *et al.*[179] used THz time-domain spectroscopy to study the ground multiplets ($^6H_3$) of Tm^{3+} ions in $TmFeO_3$. Here, the spin–orbit coupled atomic states are denoted using the spectroscopy notation $^{2S+1}L_J$, where S and L are the total spin and orbital quantum numbers, respectively, and $J = L + S$ is the total angular momentum quantum number. Using an x-cut $TmFeO_3$ crystal, the authors aligned $\boldsymbol{H}_{\mathrm{THz}} \| z$ (configuration 1 in Fig. 8) and obtained the temperature-dependent absorption spectra shown in Fig. 11(a). In addition to the sharp lines highlighted by solid markers, which are assigned to the quasi-FM and quasi-AFM modes, a strong absorption band centered at 0.54 THz appears below 70 K, gaining amplitude as the temperature decreases. A constant-temperature cut at 60 K of the colormap gives the spectrum in the top panel of Fig. 11(b). To study the polarization selection rule of the transition, the authors also performed measurements using $\boldsymbol{H}_{\mathrm{THz}} \| y$ in an x-cut crystal and a z-cut crystal, corresponding to configurations 2 and 5 in Fig. 8, respectively; see the middle and bottom panels of Fig. 11(b). Another absorption peak at 1.2 THz is identified.

Figure 11(c) displays the energy-level structure of Tm^{3+} assigned by Zhang *et al.*[179] to explain the experimental spectra. Tm^{3+}, which has even filling in the $4f$ shell, is a non-Kramers-type ion. Since Tm^{3+} ions occupy noncentrosymmetric sites with C_s symmetry, a crystal field generally splits its $^6H_3$ states into singlets, denoted by the two one-dimensional irreps of the C_s group, A_1 and A_2. The observed absorption peaks centered at 0.54 THz (R_1 and R_1' peaks) and 1.2 THz (R_3 and R_3' peaks) can be explained as the $E_1(A_1) \rightarrow E_2(A_1)$ and $E_1(A_1) \rightarrow E_3(A_2)$ transitions, respectively. The R_2 line, assigned to the $E_2(A_1) \rightarrow E_3(A_2)$ transition, should in principle appear in the $\boldsymbol{H}_{\mathrm{THz}} \| y$, $\boldsymbol{E}_{\mathrm{THz}} \| z$ configuration, but the saturated absorption observed in this case makes this line hard to detect. Further, the fact that the spectral amplitudes of the R_1 and R_3 lines increase with decreasing temperature is in agreement with the expected trend of the thermal population of the $E_1(A_1)$ ground state, corroborating the assignment of the transitions.

Li *et al.*[169] used THz time-domain magneto-spectroscopy experiments to study CFTs of Er^{3+} in $ErFeO_3$. Peak splitting and shifting versus magnetic field (applied along different crystal axes) enabled quantitative determination of the microscopic parameters of Er^{3+} ions. Figure 12(a) shows an energy-level diagram of Er^{3+}. Since Er^{3+} has odd filling in the $4f$ shell, the crystal fields remove all but the Kramers degeneracy, forming Kramers doublets $|m = \pm 15/2\rangle, |m = \pm 13/2\rangle, \ldots$, where m is the magnetic quantum number. At zero field, time-reversal-symmetry-breaking magnetic exchange interactions between Fe^{3+} and Er^{3+} slightly split the Kramers doublets. By further applying a magnetic field (B) along different crystal axes, different patterns of Zeeman splitting occur.

Figures 12(c)–12(e) show experimental absorption spectra for $ErFeO_3$ measured in configurations 1, 4, and 6 in Fig. 8, respectively. The sample temperature was 80 K. Generally, the observed absorption lines can be categorized into two groups. One group of transitions, labeled with letters (A, B, …), occurs below the THz bandwidth at $B = 0$ and blueshifts with B. This group is ascribed to intra-Kramers-doublet transitions, namely, the $|-15/2\rangle \rightarrow |+15/2\rangle$ transition (lines A and C) and the

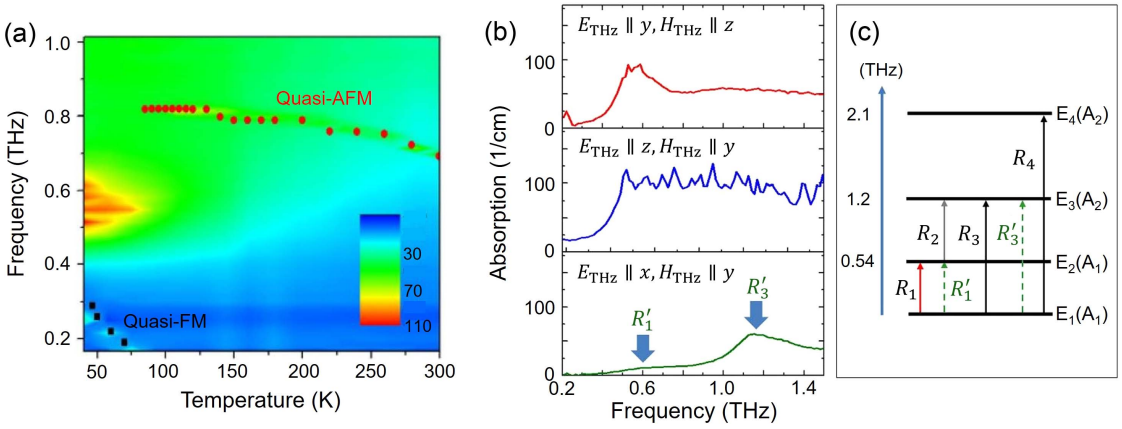

Fig. 11 CFTs of Tm^{3+} ions in $TmFeO_3$[179]. (a) Absorption coefficient mapped as a function of frequency and temperature. Red circles: quasi-AFM mode. Blue squares: quasi-FM mode. (b) Constant-temperature cut of absorption coefficient at 60 K for three different measurement configurations. (c) Energy-level diagram explaining the THz transitions. Reproduced with permission from Ref. [179].

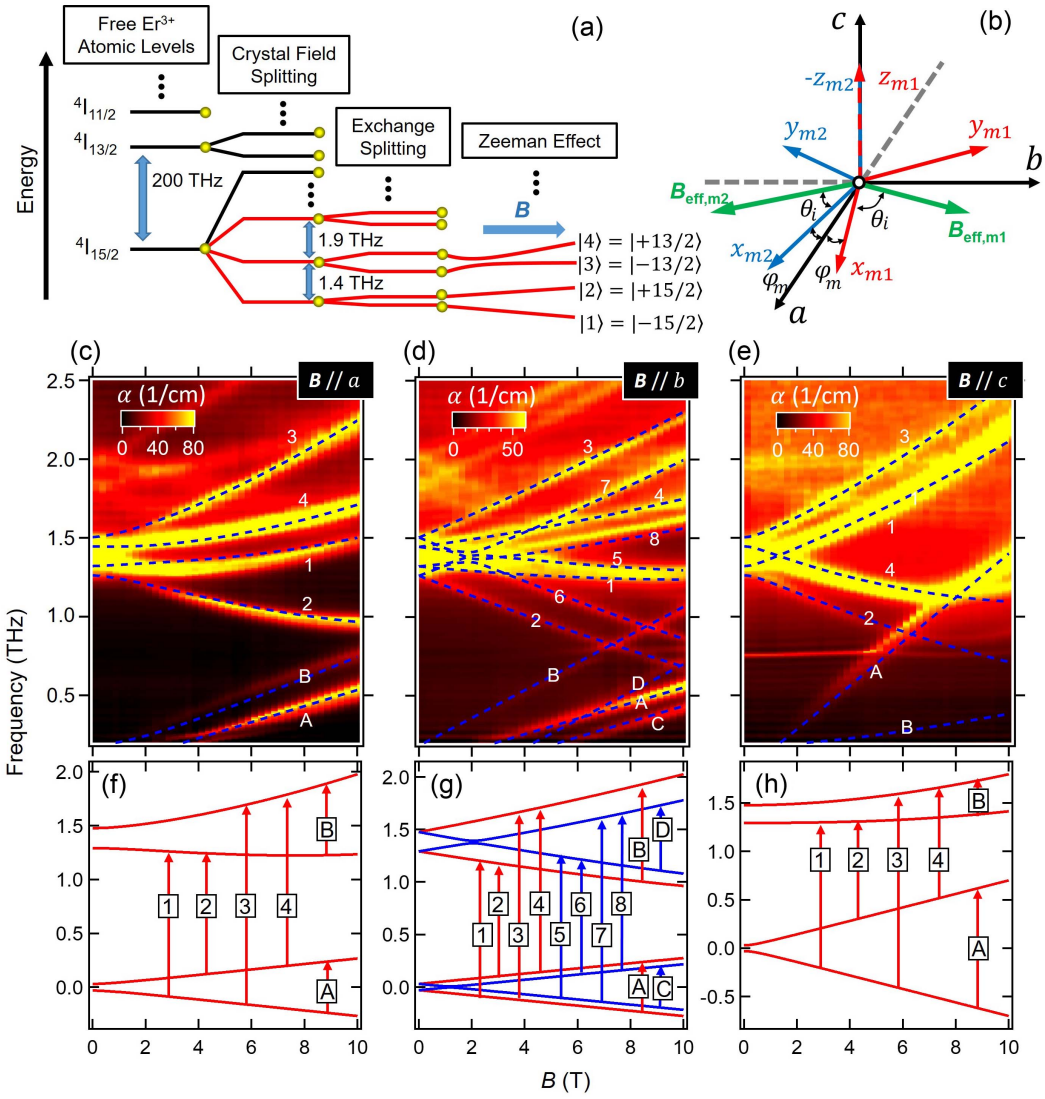

Fig. 12 CFTs of Er^{3+} in $ErFeO_3$[169]. (a) Energy-level scheme of Er^{3+}. Levels shown in red lines are involved in the transitions observed in experiments. (b) Two-sublattice model. Magneto-THz absorption spectra from measurements in (c) configuration 1, (d) configuration 4, and (e) configuration 6. (f)–(h) Energy-level calculations from the best fit of experimental spectra using the two-sublattice model, corresponding to the configurations in (c)–(e), respectively. Reproduced with permission from Ref. [169].

$|-13/2\rangle \rightarrow |+13/2\rangle$ transition (lines B and D). The other group of transitions, labeled with numbers (1, 2, …), emerges from a strong absorption band at ~1.4 THz at $B = 0$ and splits like a "firework" with B. This group is ascribed to inter-Kramers-doublet transitions, namely, the $|-15/2\rangle \rightarrow |-13/2\rangle$ transition (line 1, line 5), the $|+15/2\rangle \rightarrow |-13/2\rangle$ transition (line 2, line 6), the $|-15/2\rangle \rightarrow |+13/2\rangle$ transition (line 3, line 7), and the $|+15/2\rangle \rightarrow |+13/2\rangle$ transition (line 4, line 8). In the $\boldsymbol{B}\|y$ case, the number of lines doubles due to the broken sublattice degeneracy. More inter-Kramers-doublet transition lines centered at 1.9 THz at $B = 0$ can be identified. They are the $|\pm 13/2\rangle \rightarrow |\pm 11/2\rangle$ transition group.

Because there are two inequivalent Er^{3+} sites in the crystal, the two-sublattice model depicted in Fig. 12(b) explains the data well. Defining $j = 1, 2$ to be the Er^{3+} sublattice index, as shown in Fig. 12(b), we can see that the site orientations of the two inequivalent sublattices depend on both m and j, characterized by an angle φ_m. Furthermore, the $Fe^{3+} - Er^{3+}$ exchange coupling is described by the m- and j-dependent effective field $B_{\text{eff},mj}$ that is experienced by the Er^{3+} ion, characterized by an angle θ_m. Symmetry analysis determines that the local z_{mj} axes have to coincide with the crystal z axis, and $B_{\text{eff},mj}$ have to be in the x–y plane. The Hamiltonian for the crystal-field level m and sublattice j in a magnetic field is written as the summation of the linear Zeeman term and the quadratic Zeeman term:

$$\begin{aligned} H_{mj} &= H_{\text{linear},mj} + H_{\text{quadratic},mj} \\ &= \mu_B \sum_k g_{m,k} \hat{\sigma}_k B_{\text{tot},mj,k} \\ &\quad + (\mu_B)^2 \delta_{m,\pm 13/2} \sum_k \Delta D_k (B_{\text{tot},mj,k})^2 \hat{I}, \end{aligned} \tag{14}$$

Table 3 Crystal-Field Parameters for Levels $|m = \pm 15/2\rangle$ and $|m = \pm 13/2\rangle$ Obtained from the Fits to the 80 K Experimental Spectra Shown in Fig. 12 (reproduced with permission from Ref. [169]).

	$\lvert m = \pm 15/2\rangle$	$\lvert m = \pm 13/2\rangle$
$\lvert \boldsymbol{B}_{\mathrm{eff},mj} \rvert$ (T)	1.19	2.1
θ_m (deg)	48	80
φ_m (deg)	33	1
$g_{m,x}$	1.9	2.5
$g_{m,y}$	1.7	3.15
$g_{m,z}$	5	1.2
ΔD_x (J^{-1})	1.6×10^{22}	
ΔD_y (J^{-1})	0.6×10^{22}	
ΔD_z (J^{-1})	1.7×10^{22}	

where μ_B is the Bohr magneton, $k = x, y, z$ is the Er^{3+} local axis index, $g_{m,k}$ are the anisotropic Lande g factors, $\hat{\sigma}_k$ are Pauli matrices, $\boldsymbol{B}_{\mathrm{tot},mj} = \boldsymbol{B} + \boldsymbol{B}_{\mathrm{eff},mj}$ is the net magnetic field experienced by Er^{3+}, ΔD_k are the anisotropic quadratic Zeeman coefficients, and $\hat{I}$ is a 2×2 identity matrix. The eigen-energies of all the states can be calculated as a function of B by diagonalizing the Hamiltonian. A single group of parameters can be used to fit all three experimental spectra in Figs. 12(c)–12(e); see Table 3 for the parameters obtained from the fits. The energy-level schemes of the best fit for the $\boldsymbol{B}\|x$, $\boldsymbol{B}\|y$, and $\boldsymbol{B}\|z$ cases are plotted in Figs. 12(f)–12(h), respectively. Transition lines are identified, labeled, and plotted correspondingly in Figs. 12(c)–12(e) as dashed blue lines. Excellent agreement between theory and experiment is achieved.

Mikhaylovskiy *et al.*[180] have performed polarization-resolved THz emission spectroscopy experiments on Er^{3+} in $ErFeO_3$ to determine the dipolar activity of the CFTs. The energy-level diagram is exactly the same as the zero-field diagram in Fig. 12(a). A symmetry classification of macroscopic normal modes has been previously performed[178], dividing CFTs associated with Er^{3+} into either magnetic-dipole active or electric-dipole active in nature. Any dipolar activity can be closely related with the possible polarization state of the emitted THz radiation. Further, although the CFT excitations in this experiment are all created by ISRS processes, the magnetic- and electric-dipole transitions respond to different polarizations of the excitation light. For magnetic-dipole transitions, the effective magnetic field description, given in Subsection 2.2.1, is the dominant mechanism, the most representative of which is the IFE. Figure 13(a) shows a THz emission signal along the x axis from a y-cut crystal created by circularly polarized optical pumps with opposite helicities. A helicity-dependent signal is clearly present, whose Fourier transform is shown in Fig. 13(b); the peaks appearing in the Fourier transform are assigned to magnetic-dipole-active CFTs.

The ISRS type excitation of electric-dipole-active CFTs, on the other hand, is less straightforward since for centrosymmetric crystal generation of an effective electric field is forbidden via electric-dipole transitions. However, Mikhaylovskiy *et al.*[180] have proposed a novel mechanism based on virtual magnetic-dipole transitions, $\boldsymbol{E}_{\mathrm{eff}} \propto \chi \boldsymbol{E}_{\mathrm{opt}} \boldsymbol{H}^*_{\mathrm{opt}}$. The following summarizing statement therefore arises: the magnetic-dipole-active THz modes respond to electric-dipole optical transitions, while the electric-dipolar-active THz modes respond to magnetic-dipole optical transitions[180]. Mode assignments based on the pump-helicity dependence and polarization state of the emission were then carried out across the $\Gamma_4 \rightarrow \Gamma_2$ SRT, giving Fig. 13(c).

3.3 THz Probe of Electromagnons

Electromagnons are magnetic resonances that can be excited by the electric field of light (i.e., electric-dipole-active magnons), which is a type of excitation associated with dynamic magnetoelectric coupling[181]. Their emergence is closely related to magnetoelectric effects and novel ferroic orders[182–185], and therefore, electromagnons play an important role in the study of electric control of magnetism for functional electronic and spintronic devices[186,187]. From the group theory perspective, spatial inversion symmetry is the most important symmetry element to discuss, because the leading-order magnetoelectric tensors are axial tensors of even rank, which can have only nonzero elements in noncentrosymmetric systems. For multiferroicity to emerge, the system is required not only to be noncentrosymmetric but also to belong to a polar group.

In Subsection 2.1, we discussed possible magnetic phases that can arise in $RFeO_3$ using Bertaut's representation theory.

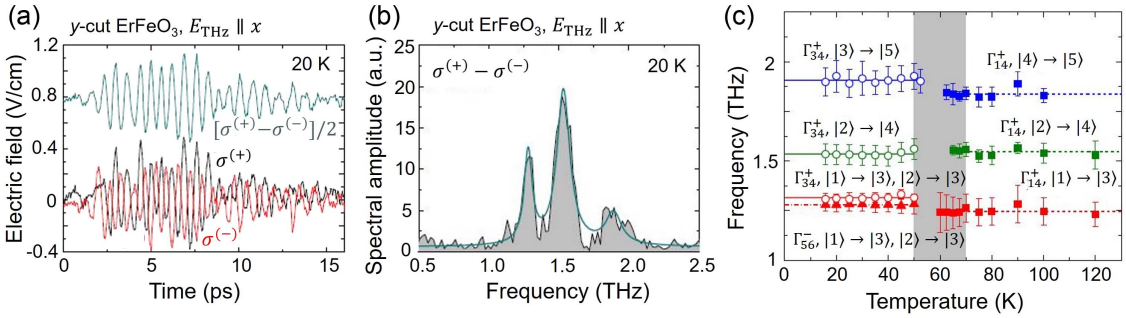

Fig. 13 Studying Er^{3+} CFTs in $ErFeO_3$ by THz emission spectroscopy[180]. (a) Pump-helicity-dependent THz emission from y-cut $ErFeO_3$. (b) Fourier transform of the helicity-dependent contribution in (a). (c) Mode symmetry assignments determined from the polarization of emission and pump-helicity dependence. Measurement configuration is the same as (a) and (b). Gray region indicates the SRT temperature range. Crystal-field states are labeled with the same notations as in Fig. 12(a). Reproduced with permission from Ref. [180].

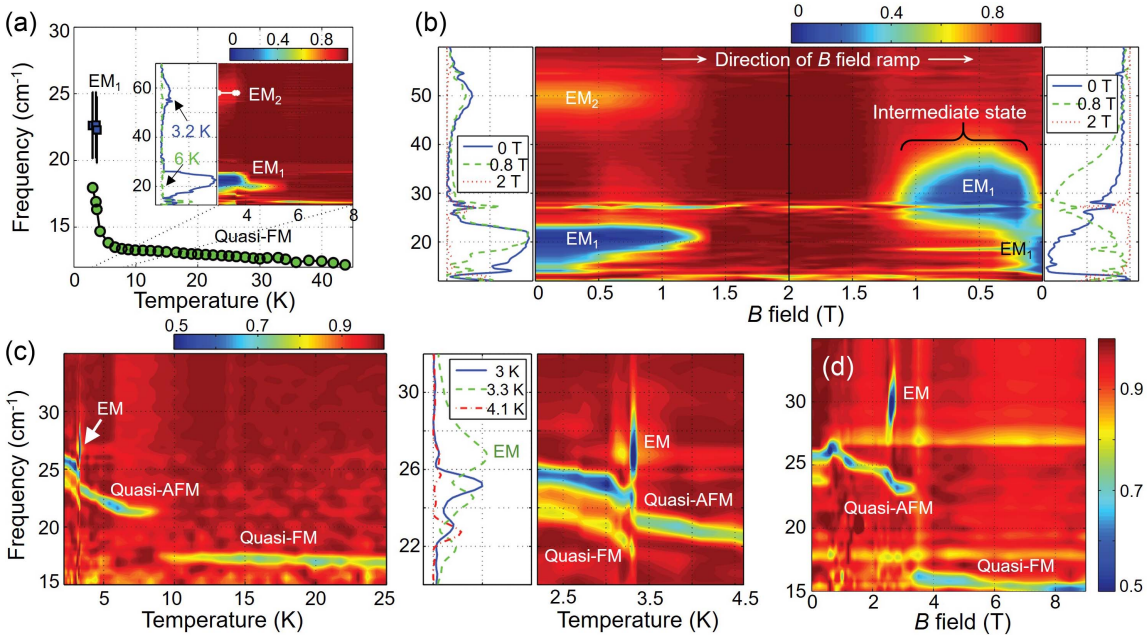

Fig. 14 Electromagnons in $DyFeO_3$ and $TbFeO_3$[195,196] measured by far-infrared transmittance spectroscopy. (a) Zero-field mode excitations as a function of temperature in the $\boldsymbol{E}_{THz}\|z$, $\boldsymbol{H}_{THz}\|y$ geometry for $DyFeO_3$. (b) Magnetic field dependence of $DyFeO_3$ transmittance using the $\boldsymbol{E}_{THz}\|z$, $\boldsymbol{H}_{THz}\|x$ geometry for $\boldsymbol{B}\|y$ at 1.5 K. Up and down sweeps are shown in the left and right panels, respectively. (c) Zero-field temperature-dependent scans using the $\boldsymbol{E}_{THz}\|z$, $\boldsymbol{H}_{THz}\|x$ geometry for $TbFeO_3$. Right panel zooms in the left panel. (d) Magnetic field dependence of $TbFeO_3$ transmittance for $\boldsymbol{B}\|y$ at 1.5 K. Reproduced with permission from Refs. [195,196].

We mentioned that, while inversion symmetry is retained in the $\Gamma_1 - \Gamma_4$ phases, it is broken in the $\Gamma_5 - \Gamma_8$ phases. Located at 4(b) sites as inversion centers, Fe^{3+} alone cannot develop an order that is consistent with $\Gamma_5 - \Gamma_8$. Therefore, to achieve potential magnetoelectric coupling and multiferroicity in the $RFeO_3$ family, R^{3+} ordering that transforms according to $\Gamma_5 - \Gamma_8$ is required.

Within the entire family, inversion-symmetry-breaking events by low-temperature magnetic ordering have been demonstrated in $GdFeO_3$[188], $DyFeO_3$[97,189], and $TbFeO_3$[190,191]. Although possible observation of room-temperature multiferroicity in $SmFeO_3$ has been reported[192], symmetry analysis calls the interpretation into question[193], leading to controversy regarding whether multiferroicity actually exists in $SmFeO_3$[194]. As shown by the phase diagram in Fig. 3, $GdFeO_3$ adopts a Γ_4 configuration from the Néel temperature of Fe^{3+} (661 K) all the way to 2.5 K. Below 2.5 K, Gd^{3+} moments order according to g_x, which transforms according to Γ_5 (Table 1). This mode mixes with the Fe^{3+} Γ_4 mode to form a noncentrosymmetric Γ_{45} configuration (point group: $m'm'2$), allowing polarization along the crystal z axis. This has been observed by Tokunaga *et al.*[188]; exchange striction, that is, the cooperative lattice distortion caused by magnetic coupling, is believed to be the microscopic origin of the polarization.

The Fe^{3+} subsystem in $DyFeO_3$ exhibits an abrupt-type SRT (named the Morin transition) at 50 K. Below 4 K, Dy^{3+} ions develop $g_x a_y$-type ordering, consistent with the Γ_5 mode; the total magnetic phase therefore becomes Γ_{15} (magnetic group: 222). This phase belongs to a nonpolar noncentrosymmetric group, which allows a linear magnetoelectric response but forbids polar order. However, polar order and multiferroicity can be switched on by applying a magnetic field along the z axis, polarizing the system into the Γ_{45} configuration (point group: $m'm'2$). $DyFeO_3$ magnetized along the z axis therefore has the same group representation as $GdFeO_3$ at zero field, allowing spontaneous electric polarization along the z axis.

Stanislavchuk *et al.*[195] have performed comprehensive far-IR spectroscopy measurements on $DyFeO_3$, aiming at probing electromagnon excitations in the low-temperature Γ_{15} phase. Figure 14(a) shows zero-field mode excitations as a function of temperature in $\boldsymbol{E}_{THz}\|z$, $\boldsymbol{H}_{THz}\|y$ geometry[2]. While the quasi-FM mode shows a prominent blueshift upon entering the Γ_{15} phase, new modes centered at 22 cm^{-1} (0.66 THz) and 58 cm^{-1} (1.74 THz), labeled EM_1 and EM_2, respectively, are observed. The authors not only ruled out phonons and CFTs as possible origins for these modes, but also determined their electric-dipole activity, namely, they are excited only for $\boldsymbol{E}_{THz}\|z$. These are consistent with characteristics of electromagnons. Further, the authors demonstrated that EM_1 and EM_2 can be observed only in the noncentrosymmetric magnetic structure, which corroborates the assignment. Upon applying a static magnetic field $\boldsymbol{B}\|y$, at a critical field of 1.3 T, a $\Gamma_{15} \rightarrow \Gamma_{43}$ phase transition occurs, which restores the inversion center (Table 1). EM_1 and EM_2 abruptly disappear across the field-induced transition [Fig. 14(b)]. Interestingly, the eletromagnons exhibit strong hysteresis upon cycling the static magnetic field $\boldsymbol{B}\|y$; compare the mode excitations in the up and down sweeps of the magnetic field in Fig. 14(b). The irreversibility potentially

[2]Strictly speaking, the far-IR measurements here are not based on THz time-domain techniques, but since they measure the same quantity, we still denote the electric and magnetic fields of the probe light this way.

reflects a metastable low-symmetry phase during the $\Gamma_{15} \rightarrow \Gamma_{43}$ phase transition, which has been demonstrated to exhibit intermediate stages[197].

By using a similar experimental technique, Stanislavchuk *et al.*[196] have also investigated THz electromagnons in a Tb^{3+}-ordered phase in $TbFeO_3$. The low-temperature phase diagram of $TbFeO_3$ is more complicated than that of $DyFeO_3$. At $T_{SR1} = 8.5$ K, a $\Gamma_4 \rightarrow \Gamma_2$ SRT occurs, which is found in many $RFeO_3$ systems. The Tb^{3+} moment orders according to $a_x g_y f_x c_y$ (Γ_{28}) at $T_{NTb} = 3.3$ K. The Γ_{28} phase holds for only a very narrow temperature range, until it transforms into a Γ_{48} phase through another SRT at $T_{SR2} = 3.1$ K. In both the Γ_{28} phase (within $3.1\,\text{K} < T < 3.3\,\text{K}$) and Γ_{48} phase ($T < 3.1$ K), inversion symmetry is broken, and therefore, potentially electromagnons can be excited.

In performing zero-field temperature-dependent scans in $\boldsymbol{E}_{THz} \| z$, $\boldsymbol{H}_{THz} \| x$ geometry, Stanislavchuk *et al.* found a wealth of mode excitation behavior, shown in Fig. 14(c); its right panel shows a zoom-in view of data at $T < 4$ K. While the switching of the polarization selection rule between quasi-FM and quasi-AFM modes was clearly observed across the $\Gamma_4 \rightarrow \Gamma_2$ SRT at T_{SR1}, both modes appeared at $T < 3.1$ K, suggesting a significant relaxation of the polarization selection rule in the Γ_{48} phase. In particular, the quasi-FM mode was found to gain electric-dipole activity in this phase. On the other hand, within the narrow temperature range of $3.1\,\text{K} < T < 3.3\,\text{K}$, a mode at 27 cm^{-1} (0.81 THz) was observed and assigned to an electromagnon (labeled EM, excited only by $\boldsymbol{E}_{THz} \| z$). The electromagnon mode also showed a delicate appearance within the field-dependent diagram for $\boldsymbol{B} \| y$ at 1.5 K [Fig. 14(d)]. It was found that $\boldsymbol{B} \| y$ leads to multistage phase transitions, and it is only within a narrow field range around 2.5 T where one can observe the EM mode. This field-induced phase features a complicated magnetic structure characterized by Γ_{2358}, which supports spontaneous polarization along the y axis.

4 Ultrafast Laser Manipulation of Magnetic Order

The ability to manipulate spins in magnetically ordered solids on the shortest possible time scale possesses significant potential for applications in future spintronic and magnetic memory devices, fast-speed computation technology, and quantum information processing[2,198–200]. Among various competing proposals, femtosecond lasers have emerged as the most suitable tool for control at the fundamental speed limit of quantum spins, namely, within ps or sub-ps time durations. In the dramatic cases where laser pulses drive the material to extreme nonequilibrium, ultrafast magnetic phase transitions occur[31,49], which has attracted considerable interest over the past two decades[201–208]. Due to the rapid pace at which current laser technology is developing, this research field is expected to gain increasing accessibility, as pulse energies become stronger, pulse durations become shorter, and wavelengths become more tunable.

However, accessibility by no means implies simplicity of the problem of interest. As a matter of fact, ultrafast laser manipulation of magnetic order has been identified as one of the most challenging topics in modern spintronics, encompassing the demand to expand the frontier of knowledge within multiple areas in physics and photonics. Since spins in magnetic solids can never be viewed as an isolated system, but instead, are frequently found to entangle with multiple other fundamental DOFs including charge, lattice, and orbit, one is faced with the demand to understand complex correlated phases and intertwined orders of condensed matter[209]. In addition, once laser excitation comes into play, the problem gains an additional level of complexity due to the nonequilibrium nature of the driven system[39–42,210,211]. Besides light–spin interactions, electronic charge transitions and lattice phonons both couple with light strongly and evolve via distinctly different pathways and speeds[58]. Thus, it is necessary to understand how the extremely nonthermal status in multiple coupled reservoirs created by laser excitation evolves in time, and the impact of such evolution on magnetism.

Once a reasonable understanding of the material itself and light–matter interaction is established, what becomes challenging is the way to tailor optical pulses to achieve the desirable type of light–matter interaction. Within the (usually) undiscriminating excitations of multiple reservoirs by light, one identifies the type of excitation that can most efficiently foster the desired modification to spin order. Is it preferable that light interacts only with spins so that charge and lattice excitations should be suppressed? Or, if spins do not interact with light strong enough, could one strongly excite the lattice, and manipulate spins through lattice–spin interactions? Tailoring light excitations following answers to considerations like these advances the so-called "surgical" approach of laser manipulation of condensed matter[62]. Within the process, one leverages state-of-the-art laser technology, seeks guidance from theoretical proposals of nonequilibrium quantum matter[212–215], and creates novel experimental methodologies. All of these activities depend uniquely on the magnetic material of interest, and thus, the number of opportunities is vast for creating a unique combination of conditions to tailor magnetism on demand.

Historically, magnetic metals[216,217], semiconductors[218–222], and insulators[223] have all been used as candidates for laser manipulation of magnetic order; phenomenology and microscopic descriptions are very different, but we will not review all of them at length here. Rather, we focus on the role of $RFeO_3$ along this line of effort. $RFeO_3$ represents the most prototypical Heisenberg-type of AFM insulator. The magnetic energy hierarchy and temperature-dependent magnetic phase diagram are well understood. THz-frequency magnons, serving as the fingerprints to track distinct magnetic phases, have been well characterized; see Section 3. Therefore, the stage for the quest for laser manipulation of magnetic order has been set. In the following subsections, we discuss five major pathways to achieve ultrafast laser-induced magnetic phase transitions in $RFeO_3$ that have been reported in the literature.

4.1 Ultrafast Laser-Induced Heating

Modification of magnetic order due to laser-induced heating is a widely observed phenomenon and has been proven to be effective. Photons absorbed by the sample (kept in a thermal bath at temperature T) through electronic excitations increase the local temperature by ΔT, and the magnetic order evolves towards the status that would be expected for a sample at $T + \Delta T$. Scrutiny is required when heating is supplied by a femtosecond laser pulse. Since the time duration of excitation is shorter than the typical durations of electronic decay and electron–lattice thermalization, the way to perceive ΔT strongly depends on the time delay after pump excitation.

A phenomenological three-temperature model has been frequently applied to describe the time evolution of the thermal properties of the system[216,224]. As shown in Fig. 15(a), the model assumes three separate but mutually interacting reservoirs, namely, the electrons, lattice, and spins, which are given respective pump-induced temperature changes—$\Delta T_{\text{electron}}$, $\Delta T_{\text{lattice}}$, and ΔT_{spin}. At early time delays immediately after the pump excitation of the charge sector, $\Delta T_{\text{electron}}$ is the largest. Then $\Delta T_{\text{lattice}}$ and ΔT_{spin} increase with time at the expense of $\Delta T_{\text{electron}}$ through energy transfer processes at rates determined by the coupling strengths between the reservoirs [Fig. 15(b)]. It is only at time delays when $\Delta T_{\text{electron}}$, $\Delta T_{\text{lattice}}$, and ΔT_{spin} have fully converged (quasi-equilibrium condition) can an overall local temperature increase of the system ΔT be defined, but for the purpose of controlling the magnetic properties, examining ΔT_{spin} only before reaching quasi-equilibrium is also reasonable.

Within the $RFeO_3$ class, the temperature range around the Fe^{3+} SRT is ideally suited for ultrafast magnetic phase transitions induced by laser heating. In the spin Hamiltonian, Eq. (4), although the isotropic exchange constant and the DM interaction constant are temperature independent, the anisotropy energies depend strongly on the temperature. In $TmFeO_3$, by spectroscopically resolving quasi-FM and quasi-AFM mode frequencies, the temperature dependence of the A_x and A_z constants has been quantitatively determined. Their difference, $A_x - A_z$, has been found by Zhang *et al.*[179] to change sign across the SRT temperature range (80–90 K); see Fig. 16. This suggests that a sign change of a similar origin would occur when one imposes ultrafast heating on a sample kept around the SRT temperature as well. The laser-heated sample would then have an easy axis that deviates from that in equilibrium, leading to a spin-structure rotation.

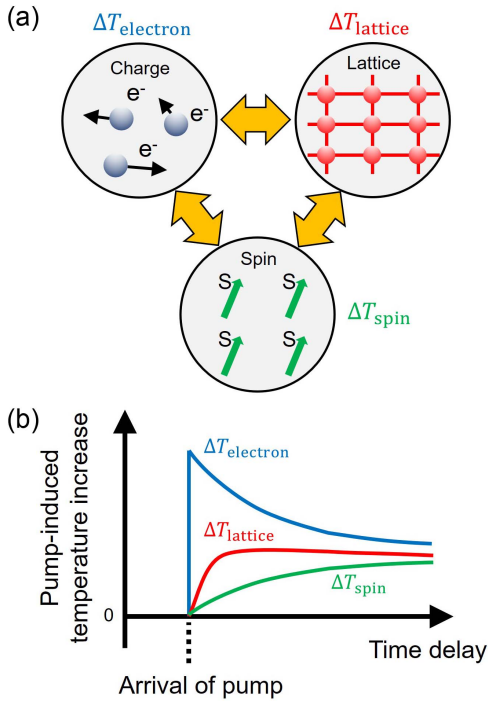

Fig. 15 Three-temperature model. (a) Separate but mutually interacting reservoirs. (b) Time dynamics of temperatures of the reservoirs.

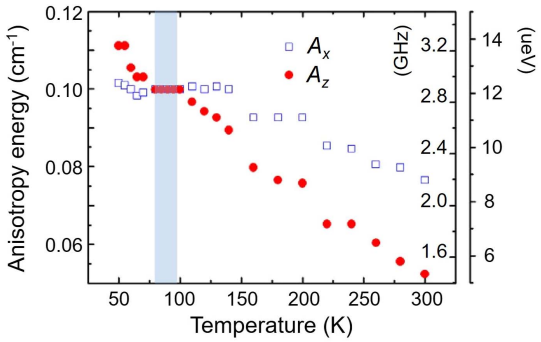

Fig. 16 Temperature dependence of the anisotropy constants, A_x and A_z, in $TmFeO_3$[179]. Reproduced with permission from Ref. [179].

Kimel *et al.*[225] have performed time-resolved linear birefringence measurements on a $TmFeO_3$ crystal around the SRT temperature in the presence of ultrafast pump excitation. In equilibrium (with no pump excitation), it was found that linear birefringence is a sensitive indicator of the orientation of the AFM vector $\boldsymbol{G}$ across the $\Gamma_4 \rightarrow \Gamma_{24} \rightarrow \Gamma_2$ transition [Fig. 17(a)]. This type of probe mechanism couples to the $\boldsymbol{G}$ vector directly, which is different from the Faraday- or Kerr-effect probes (which couple linearly to the bulk magnetization). As detailed in Subection 2.2.1, the probe utilizes the symmetric portion of the dielectric permittivity tensor, which contains a term that reads $\varepsilon_{ii} = \beta_{iijk} G_j G_k$; the coupling to $\boldsymbol{G}$ is quadratic and sensitive to the rotation of $\boldsymbol{G}$ across the SRT. In a z-cut crystal, when the polarization is aligned in-plane between x and y axes (propagation along z), the birefringence $\Delta n_{xy} = (\varepsilon_{xx} - \varepsilon_{yy})/2n$ is detected by reading the polarization of the transmitted probe pulse.

Upon pump excitation, time-resolved linear birefringence reflects the pump-induced change in $\boldsymbol{G}$. As shown in Fig. 17(b), such traces were collected at different sample temperatures. In the time domain, three distinct regimes were identified: regime (1) is a fast decay due to the charge-phonon thermalization within 1 ps, regime (2) spans from 1 to 10 ps and makes the signal settle to an offset compared to the equilibrium value, and regime (3) represents the range with longer time delays showing magnon oscillations. Regime (2) is particularly notable due to the offset structure that is developed in linear birefringence, suggesting the rotation of $\boldsymbol{G}$ within the same time duration[225]. The pump-induced heating mechanism explains the direction of $\boldsymbol{G}$ rotation perfectly. What further corroborates the interpretation is that the pump-induced spin reorientation has the largest amplitude around and slightly below the equilibrium SRT temperature range [Fig. 17(c)]. This is expected because at temperatures far below or above the SRT temperature, the laser-induced transient temperature rise is unable to cause a sign change in $A_x - A_z$ (Fig. 16), leading to no change to the easy axis. What makes the observation more interesting is that the spin rotation reaches a maximum amplitude of 30 deg, which is a considerable fraction of the full $\Gamma_4 \rightarrow \Gamma_{24} \rightarrow \Gamma_2$ transition in equilibrium, and completes the rotation within the first 4 ps of regime (2), which is faster than the spin precession period. The fast and large-amplitude spin control therefore opens up promising applications in magnetic random access memory devices.

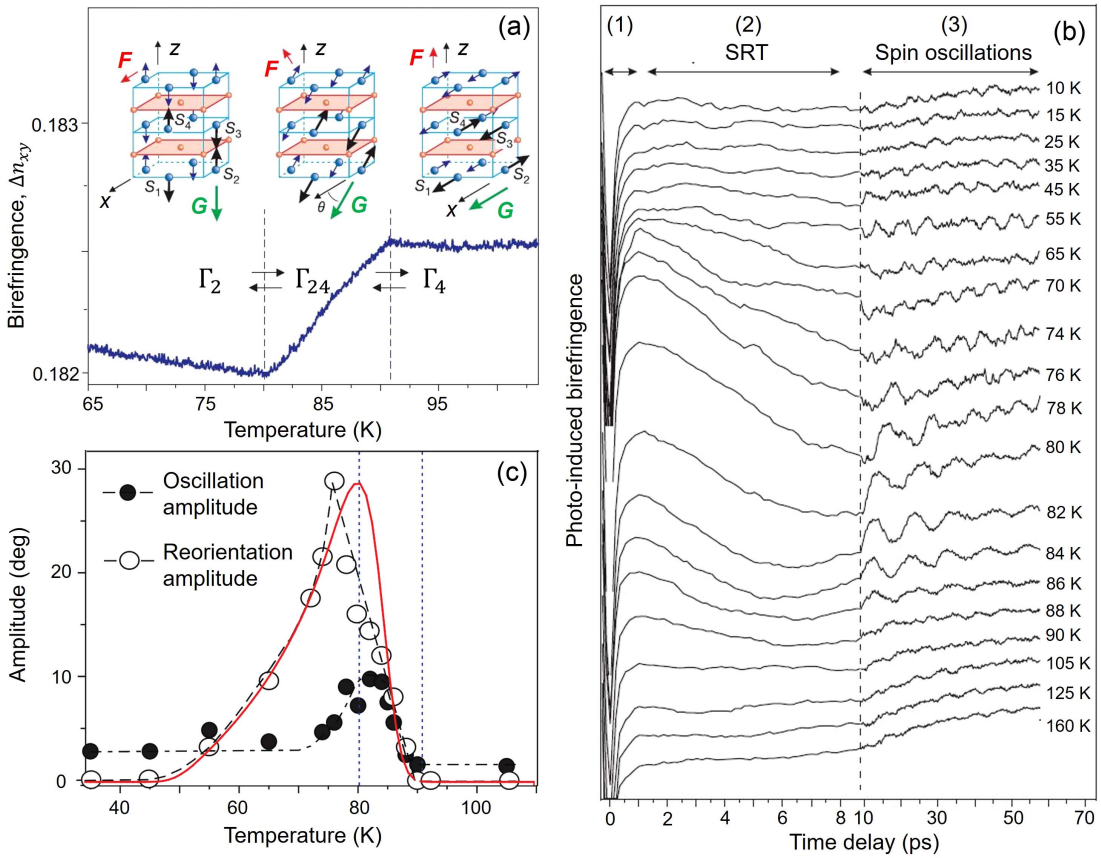

Fig. 17 Ultrafast-heating-induced SRT in $TmFeO_3$[225]. (a) Equilibrium linear birefringence as a function of temperature. (b) Time-resolved pump–probe linear birefringence traces at different temperatures. (c) Temperature dependence of the amplitudes of magnon oscillations and reorientation amplitude extracted by fitting to the data in (b). Reproduced with permission from Ref. [225].

A similar experiment by de Jong *et al.*[226] performed on $ErFeO_3$ around the SRT temperature exhibited some differences compared to the $TmFeO_3$ experiment[225]. The laser-induced SRT again showed the strongest amplitude in the vicinity of the equilibrium SRT temperature range; see Fig. 18(a) for the offsets of the time-resolved Faraday rotation traces on an *x*-cut crystal. However, the rise of the spin rotation took a considerably longer time (~40 ps) than in $TmFeO_3$ (~4 ps). This raises the question of the microscopic pathway for ultrafast heating. In $TmFeO_3$, the very fast completion of spin rotation suggests that the anisotropy modification gets well established within 1 ps, while in $ErFeO_3$, the fact that spin rotation is much slower than the precession period implies that the heating process itself, and likewise, the modification of the anisotropy axis, take a longer time.

Yamaguchi *et al.*[227] have provided valuable insight into the problem. The quasi-FM mode, whose frequency is sensitive to anisotropy energy $A_x - A_z$ [Eq. (5)], was first launched by a THz pump. Once the oscillation was stabilized [Fig. 18(b)], an NIR heating pulse pumped the system again [Fig. 18(c)], and the dynamics of the magnon frequency shift following the NIR pulse revealed the time evolution of the anisotropy energy [Fig. 18(d)], and thus, the true time scale of heating. For $ErFeO_3$, it was found that heating took ~15 ps, which naturally explains why the laser-induced SRT observed by de Jong *et al.*[226] was slow. This finding also corroborates a model proposed by de Jong *et al.*[226] that analyzes the microscopic pathway of ultrafast heating in the entire $RFeO_3$ class. As shown in Fig. 18(e), when the electronic states of Fe^{3+} are excited by the pump pulse, the energy needs to be passed over to the rare-earth ion R^{3+} to modify the anisotropy. Since the Fe^{3+}–lattice interaction is strong, the entire pathway is bottlenecked by the lattice-R^{3+} energy transfer; the transfer rate strongly depends on the rare-earth ion species[228]. The knowledge over the ultrafast heating pathway has led to protocols to control the timing and speed of laser-induced SRTs[226].

Kurihara *et al.*[229] have performed another interesting experiment, demonstrating reconfigurable magnetic domain control by laser heating. Unlike the previous examples of ultrafast transient heating, where the effect disappeared when heat diffused outside the pumped area, this work utilized static heating, a time-averaged effect of temperature rise due to laser illumination. An intense THz beam from a free-electron laser (FEL) was used. The beam consisted of macropulses with energy up to 40 mJ, spectrally centered around 4 THz, at a repetition rate of 5 Hz. Each macropulse consisted of short micropulses with peak electric fields of the order of several MV/cm (at the focus spot) and a pulse separation of 37 ns. Faraday rotation imaging microscopy on a *z*-cut $ErFeO_3$ crystal at room temperature was performed by a continuous-wave probe laser in the presence of

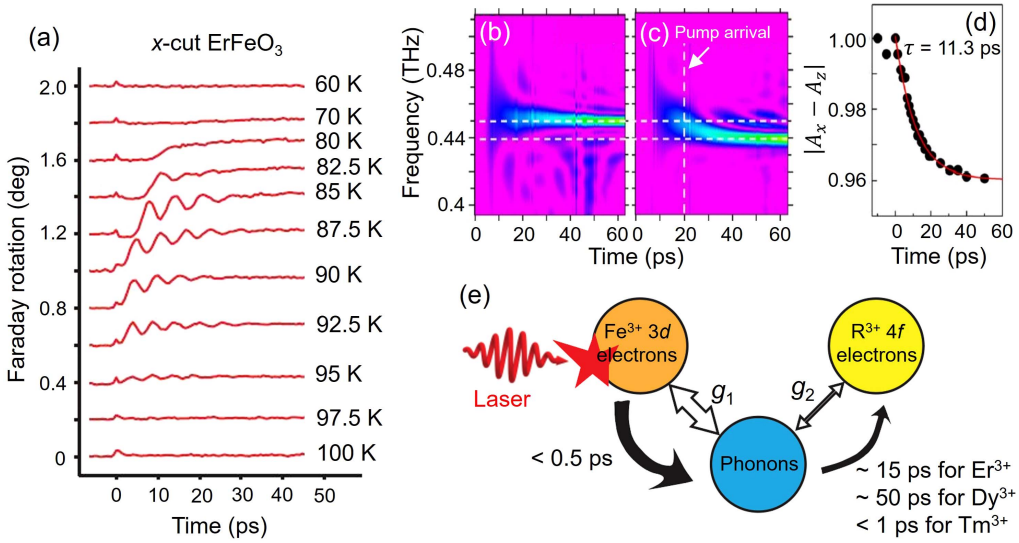

Fig. 18 (a) Ultrafast-heating-induced SRT in $ErFeO_3$ probed by time-resolved Faraday rotation[226]. (b) THz pump Faraday rotation probe experiment on $ErFeO_3$[227]. Quasi-FM mode whose frequency is stable with time is observed. (c) Same experiment as (b) except that an additional near-infrared pulse excites the sample at 20 ps to produce ultrafast heating. The temperature was 30 K. (d) Time evolution of the anisotropy energy due to ultrafast heating extracted by fitting the magnon frequency shift in (c). (e) Energy-transfer scheme among three reservoirs during ultrafast heating[226]. 3*d* electrons and phonon quickly thermalize upon excitation, but the energy transfer rate between 4*f* ions and lattice depends on the 4*f* ion species. The model resembles the three-temperature model in essence, but slightly differs in the definition of reservoirs. Reproduced with permission from Refs. [226,227].

THz FEL illumination. It was observed that the laser heating expands the minority domains (whichever has a smaller volume fraction between spin-up and spin-down domains) when the FEL focal spot scans spatially on the same surface; see Fig. 19(a). Upon analysis of an extensive image data set, they found that as the minority domain expands, the active area of domain flipping does not coincide with the center of the laser spot (where the intensity is highest), but instead, appears at the trailing side of the spot where the spatial gradient of intensity is large. Guided by these observations, the domain reconfiguration was interpreted to result from an entropy force exerted by the laser-induced thermal gradient, assisted by the depinning effect due to static heating.

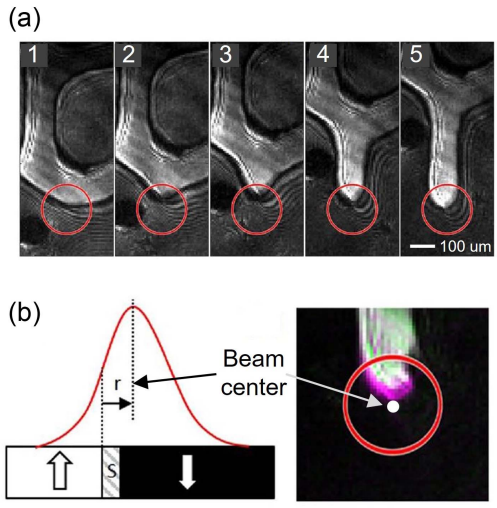

Fig. 19 Reconfigurable magnetic domains in $ErFeO_3$ by static heating from a THz free-electron laser (FEL)[229]. (a) Sequence of Faraday rotation microscopy images showing spin-up domain expansion when the FEL spot (macropulse energy: 8 mJ) scans on the sample surface. Red circle: FEL focal spot. (b) Active area of domain flipping is off from the center of the laser spot. Reproduced with permission from Ref. [229].

A related but different observation was made by Afanasiev *et al.*[230] in their magneto-optical imaging experiments performed on $DyFeO_3$, which tracks the $\Gamma_4 \rightarrow \Gamma_1$ transition. Instead of demonstrating laser-induced temperature rise as in all the examples shown above, they discovered an intriguing long-lived effect where laser illumination seems to be "cooling" the crystal; the Morin temperature appears to shift higher for a sample area illuminated by a few laser pulses (pulse energy ~20 μJ), and the shift is robust against thermal cycling. It has been proposed that the laser "cooling" originates from modification to Dy–Fe exchange interaction due to photo-ionization of Dy^{3+}, which in turn changes the anisotropy landscape experienced by the Fe^{3+} spins. This type of anisotropy control in the opposite direction of a laser-induced temperature rise is unique among this line of work.

4.2 Photomagnetic Pathways

Photomagnetic effects, whose basic properties are overviewed in Subsection 2.2.1, represent an important nonthermal pathway for achieving laser manipulation of magnetism. The effective magnetic fields generated by IFE and ICME do not rely on the absorption of photons, but rather, depend sensitively on the five property tensors in Table 2 and laser polarization.

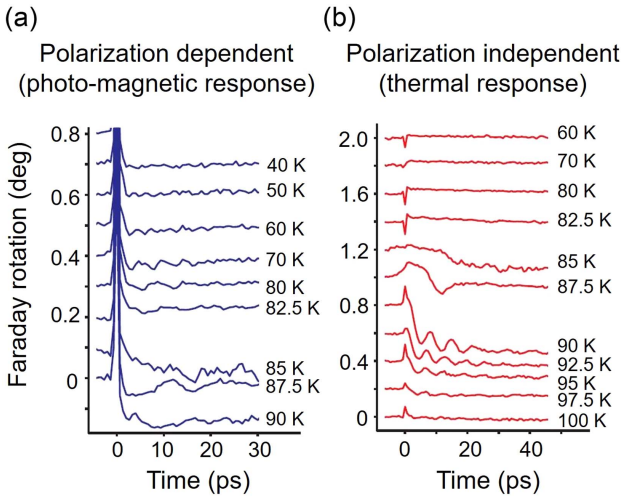

Fig. 20 Comparison of time scales between (a) photomagnetic-effect-induced SRT and (b) laser-heating-induced SRT, analyzed by extracting the polarization-dependent and polarization-independent probe responses, respectively[226]. Reproduced with permission from Ref. [226].

This suggests a wider range of tuning possibility that can be afforded by this method.

As discussed in Subsection 4.1, de Jong *et al.*[226] observed that the time scale for ultrafast-heating-induced SRT in $ErFeO_3$ is 40 ps. The same study also analyzed the impact of IFE on SRT by pumping with circularly polarized light with opposite helicities and extracted the pump-polarization-dependent response of the Faraday rotation probe. As shown in Fig. 20(a), the IFE visibly creates an offset in the Faraday rotation signal around the SRT temperature range in a z-cut crystal, indicating a similar type of laser-induced spin rotation as in the case of ultrafast heating. The difference, however, is that the rotation caused by IFE is considerably faster; see the comparison between the 90 K curves shown in Figs. 20(a) and 20(b).

The potential of fast and impulsive spin switching via photomagnetic effects has been demonstrated by Kimel *et al.*[231]. The study attempted to harness the inertia of spins to switch the equilibrium magnetic configuration to a metastable state; this involves overcoming a potential barrier that separates two local minima in the free-energy potential, as shown in Fig. 21(a). $HoFeO_3$ provides an appropriate double-minima free-energy landscape by hosting both Γ_{12} and Γ_{24} configurations within a particular temperature range [Fig. 21(a)]. The "kick" to the spin system was supplied by a short but intense magnetic field pulse generated by IFE.

Upon certain simplifications, the magnetic configuration can be described by a single parameter, that is, the azimuthal angle φ of the AFM vector defined in Fig. 21(a). For the Γ_{12} phase (initial unperturbed phase), $\varphi = 0$, $\boldsymbol{F}$ is along x, and $\boldsymbol{G}$ is in the y–z plane. For the Γ_{24} phase, there are two possible domains with $\varphi = \pm\pi/2$, $\boldsymbol{F}$ has a finite z component, and $\boldsymbol{G}$ is in the x–z plane. The equation of motion is

$$\frac{d^2\varphi}{dt^2} + 2\Gamma\frac{d\varphi}{dt} + \omega_0^2\frac{dw(\varphi)}{dt} - \frac{\gamma^2 H_D}{\sin\theta}H(t)\cos\varphi = 0. \quad (15)$$

The first term reflects the spin inertia (second derivative suggests the presence of acceleration), and the second, third, and fourth terms represent the spin damping, restoring force, and driving force, respectively. Γ is the damping constant, ω_0 is the magnon frequency, H_D is the DM field, θ is an angle defined in Fig. 21(a) and is assumed to be constant, and $H(t)$ is the IFE-induced magnetic pulse. One can tell that the driving force relies on the presence of DM interaction and is strongest in the Γ_{12} phase ($\cos\varphi = 1$).

Experimentally, Kimel *et al.*[231] then used circularly polarized light to pump a z-cut crystal and probed via Faraday rotation, keeping in mind that $\boldsymbol{F}$ is expected to develop a

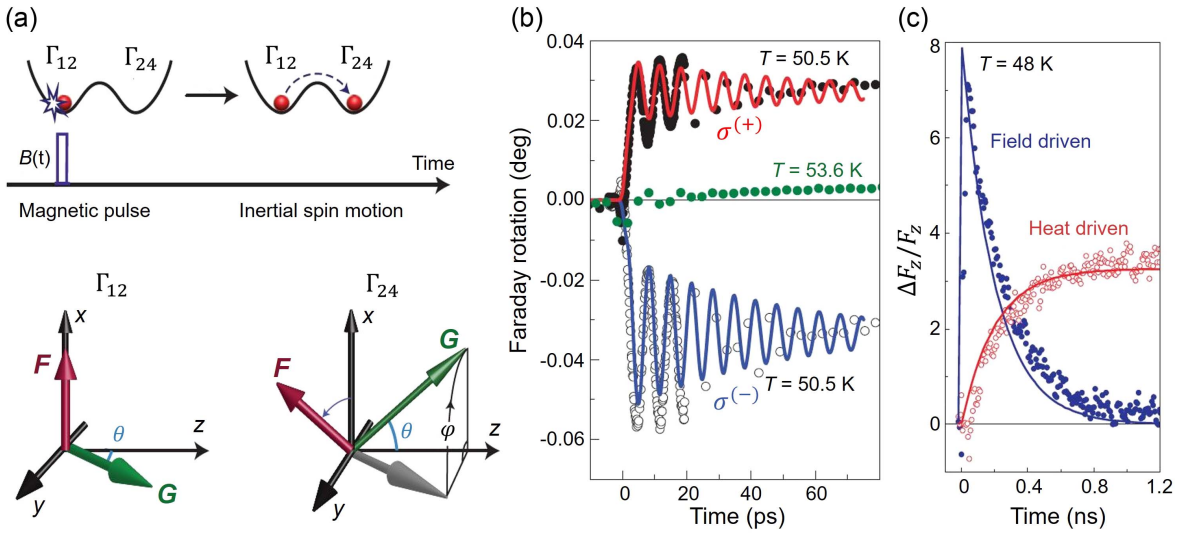

Fig. 21 Inertia-driven SRT in $HoFeO_3$[231]. (a) Intense magnetic field pulse generated by IFE supplies enough kinetic energy to enable spin switching to a metastable state. In $HoFeO_3$, the two free-energy minima coincide with the Γ_{12} and Γ_{24} phases, distinguished by an azimuthal angle φ of the AFM vector. (b) Observation of spin switching when the photomagnetic pulse exceeds a critical field strength. (c) Time scale of IFE-induced switching is much faster than the heating time scale. Reproduced with permission from Ref. [231].

finite projection onto z when a Γ_{12} to Γ_{24} switching occurs. Figure 21(b) indeed shows the fast development of a finite offset in the signal, whose sign flips when the pump helicity is reversed; this is the expected behavior for switching into the two possible types of domains, $\varphi = \pm\pi/2$, for the Γ_{24} phase. In addition, when the pump intensity is reduced so that the IFE-induced field is smaller than the critical field required for the switching (~0.5 T), the offset fails to develop and the system remains in Γ_{12} [green curve in Fig. 21(b)]. The pump polarization dependence unambiguously points to the nonthermal nature of the switching, and as shown in Fig. 21(c), the switching governs the behavior of the system at early time delays, arising considerably faster than the heating-induced response.

From the two examples above, one can tell that the thermal effects of laser heating and nonthermal photomagnetic effects usually coexist in an actual experiment, and some pump polarization arguments need to be made to distinguish the two. In fact, their coexistence is not always a drawback, but instead, can be leveraged to realize more powerful control over the routes of laser-induced SRTs. de Jong *et al.*[232] have established a unique single-shot magneto-optical imaging setup to study this possibility. When a z-cut (SmPr)FeO_3 crystal is initially kept in the low-temperature Γ_2 phase, $\boldsymbol{F}$ has zero projection along z, and the Faraday rotation image appears gray [first column in Fig. 22(a)]. If a linearly polarized pulse heats up the sample, a transition to Γ_4 within the laser spot manifests through the appearance of the equal populations of the two energetically degenerate domains with either positive or negative F_z [first row in Fig. 22(a)]. However, when the heating pulse is circularly polarized, the domain state that the system transitions into can be selected, and uniformly registered within the spot; see the second and third rows in Fig. 22(a). The interpretation for the domain-controllable SRT is shown in Fig. 22(b). A spin oscillation whose phase is determined by the pump helicity is initially excited in the single-well potential through IFE. Since the same pulse also induces ultrafast heating, the free-energy landscape then evolves according to the temperature-dependent SRT. At the instant where the landscape becomes a double well (Γ_4), the symmetry of the system is in fact broken due to spin oscillations. The well to which the system is closer at that instant is the more favorable state that the system will evolve into eventually. Therefore, by controlling the phase of spin oscillations through IFE, the domain state of the ultrafast-heating-induced SRT can be controlled.

This method of utilizing both symmetry breaking by spin precessions and ultrafast heating to achieve domain-controllable SRT has been demonstrated in another notable work by Kurihara *et al.*[233] using a double-pump scheme. Here, the THz magnetic pulse that initiates spin precession is separated from the NIR heating pulse by a time delay of dt [Fig. 23(a)]. On a z-cut $ErFeO_3$ crystal initially in the Γ_2 phase, launching the quasi-FM mode induces an oscillation of the out-of-plane magnetization component F_z, with the sign of F_z alternating in time. When the NIR heating pulse arrives, the instantaneous sign of F_z determines an SRT into one of the two Γ_4 domains; the domain with the same sign of F_z would be more favorable. Figure 23(b) clearly shows the alternating final-state magnetization (period synchronized with that of spin precessions) achieved in the Γ_4 phase by sweeping dt. In addition, since a metamaterial ring was used to enhance the THz magnetic field, the authors also compared the final-state magnetization curves between spots inside and outside the ring [Fig. 23(c)]. The two curves are out-of-phase, consistent with the fact that the phase of the symmetry-breaking spin precession is determined by the sign of the THz magnetic pulse.

4.3 Phonon Pathway

A rapidly developing method for nonthermal control of quantum materials is resonant excitation of IR active phonons. The superexchange interaction, which governs the magnetic properties of TM compounds, depends critically on the orbital overlap between TM ions and ligands, so it is expected to be effectively modified by lattice distortions induced by phonons. Two particularly notable pathways aligned with this idea are the nonlinear phononics and the phonomagnetic effect within the framework of dynamical multiferroicity.

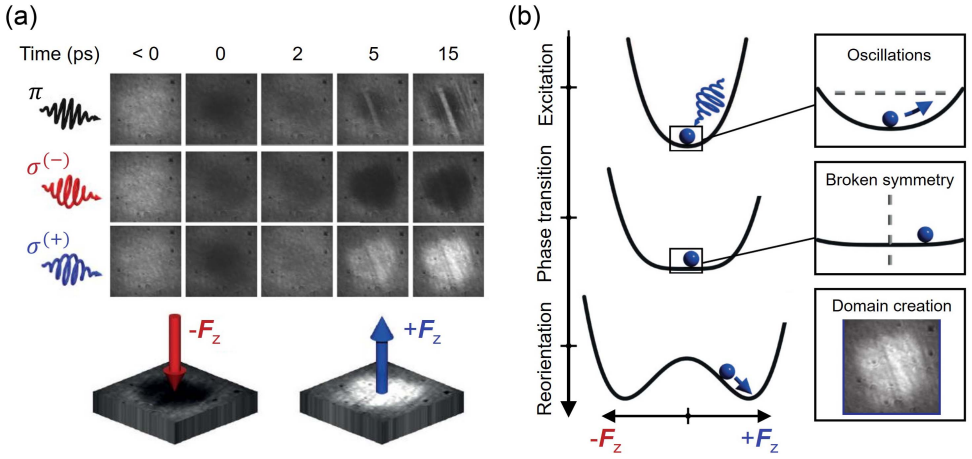

Fig. 22 Domain-controllable laser-induced SRT due to the combined effect of IFE and ultrafast heating[232]. (a) Faraday rotation images taken after a single shot of pump pulse by various delay times around the $\Gamma_2 \rightarrow \Gamma_4$ SRT temperature range. Gray corresponds to the Γ_2 phase. Black (white) corresponds to a spin-down (-up) domain in the Γ_4 phase. (b) Mechanism for controllable switching. Reproduced with permission from Ref. [232].

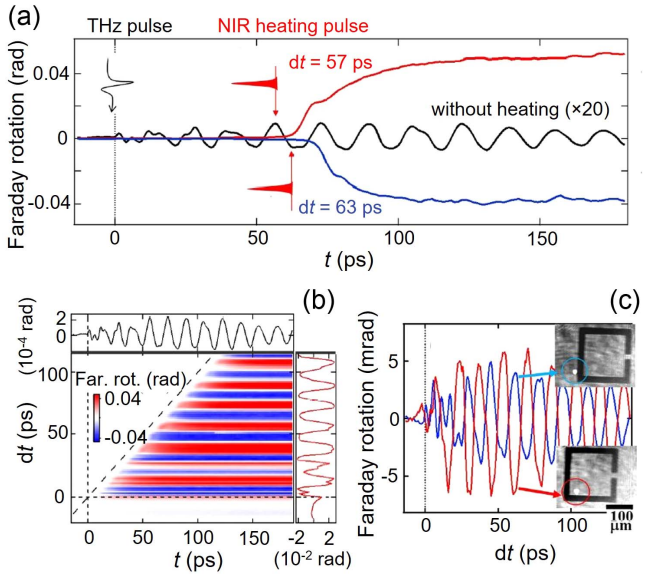

Fig. 23 Domain-controllable SRT in $ErFeO_3$ using THz-NIR double pumping[233]. (a) THz pump field (enhanced by a metamaterial) first launches a coherent magnon, and depending on the timing of the NIR heating pulse within the magnon oscillation period, the SRT can be controlled to show a single domain. The sample temperature is 84 K. (b) 2D plot of Faraday rotation as a function of probe time delay t and THz-NIR time interval dt. (c) Final-state magnetization as a function of dt has opposite phase when probing inside and outside the metamaterial ring, suggesting the SRT pathway is sensitive to the sign of the THz magnetic field. Reproduced with permission from Ref. [233].

Nonlinear phononics is a proposal to induce nonequilibrium distortions of a crystal by harnessing the anharmonicity of the lattice free-energy potential[64,234–236]. One can consider an anharmonic potential that includes only the cubic term (and neglects all higher orders)

$$V_{\text{anh}} = g_{ijk} Q_i Q_j Q_k, \tag{16}$$

where Q represents normal coordinates of a phonon, g_{ijk} is the coupling coefficient, and the indices in the sum, i, j, k, run over various phonon modes. An important criterion imposed by symmetry is that V_{anh}, being a constituent of the total free energy, must remain invariant under all symmetry operations within the crystallographic point group; this limits the possible combinations of phonons that can couple. The criterion can be expressed as

$$[\Gamma_1 \otimes \Gamma_2] \otimes \Gamma_3 \supset A_g, \tag{17}$$

which means that the direct product of the irreps of all three phonons involved in the coupling in Eq. (16) must contain the fully symmetric irrep (A_g for centrosymmetric crystals, which applies to $RFeO_3$).

One widely explored scenario[234,237] is when the first two irreps are from the same IR active phonon, while the third is from a Raman (R) phonon, which gives $[\Gamma_{\text{IR}} \otimes \Gamma_{\text{IR}}] \otimes \Gamma_{\text{R}} \supset A_g$, and $V_{\text{anh}} = g(Q_{\text{IR}})^2 Q_{\text{R}}$. The equation of motion for the IR and R phonon coordinates under a resonant laser drive of the IR mode can then be derived as[64]

$$\begin{aligned} &\ddot{Q}_{\text{IR}} + \gamma_{\text{IR}} \dot{Q}_{\text{IR}} + (\omega_{\text{IR}}^2 + 2gQ_{\text{R}}) Q_{\text{IR}} = z_i^* E(t), \\ &\ddot{Q}_{\text{R}} + \gamma_{\text{R}} \dot{Q}_{\text{R}} + \omega_{\text{R}}^2 Q_{\text{R}} = -g(Q_{\text{IR}})^2, \end{aligned} \tag{18}$$

where $\gamma_{\text{IR(R)}}$ is the IR (R) phonon decay rate, $\omega_{\text{IR(R)}}$ is the IR (R) phonon frequency, $E(t)$ is the time-dependent laser driving field, and z_i^* is the Born effective charge of the IR phonon. It is clear that the Q_{IR} is majorly driven by the laser field, but Q_{R} is driven by $-g(Q_{\text{IR}})^2$, which relies entirely on anharmonicity and the Q_{IR} amplitude. Figure 24 plots the time evolution of Q_{IR} and Q_{R} upon pulsed laser excitation (whose center frequency is resonant with ω_{IR}). The coordinate Q_{IR} oscillates around zero, whose amplitude grows during the drive, and decays after the drive. On the contrary, Q_{R} develops a rectified response with a nonzero time average in the time period during which Q_{IR} is oscillating. This is a significant result since it suggests a distortion of the lattice along the R phonon coordinate lasting on the order of $1/\gamma_{\text{IR}}$, which can be much longer than the oscillation periods, $1/\omega_{\text{IR}}$ or $1/\omega_{\text{R}}$. Furthermore, the R phonon coordinate is likely to have no equilibrium analog, suggesting access to distorted structures that cannot be achieved by applying static strain fields or pressure. Such a unique lattice control opens up vast possibilities for ultrafast manipulation of magnetic order.

Afanasiev *et al.*[238] resonantly pumped the highest frequency B_{1u} phonon mode at 85 meV of a (001)-oriented $DyFeO_3$ crystal, and measured time-resolved Faraday rotation signals at various temperatures. In equilibrium, $DyFeO_3$ shows a $\Gamma_1 \rightarrow \Gamma_4$ SRT upon warming up across the Morin temperature (51 K). The authors demonstrated the nonequilibrium analog of the same SRT induced by the phonon pumping scheme. As shown in Fig. 25(a), it was observed that phonon pumping causes the quasi-AFM mode frequency to redshift at $T < 51$ K, and blueshift at $T > 51$ K, and the magnitude of the shifts depends sensitively on the spectral overlap between the pump and the phonon absorption peak [Fig. 25(b)]. Since the quasi-AFM frequency is a probe of the local curvature of the magnetic potential, these observations hint at modification of the magnetic potential due to the phonon drive.

Figure 25(c) shows that when the crystal in the Γ_1 phase is pumped with increasingly strong fluences, an offset ΔM develops in the Faraday rotation transients; this indicates a $\Gamma_1 \rightarrow \Gamma_4$ SRT because the Γ_4 phase possesses a weak magnetization along z. The offset ΔM exhibits a threshold behavior as a function of fluence [Fig. 25(d)], showing the largest amplitude slightly below the Morin temperature [Fig. 25(e)]. Through DFT calculations, Afanasiev *et al.*[238] argued that nonlinear phononic coupling with the form $V_{\text{anh}} = g(Q_{B_{1u}})^2 Q_{A_g}$ is the cause of the SRT. By driving the B_{1u} IR phonon to large amplitude, the crystal distorts along a fully symmetric A_g phonon coordinate that involves antipolar motions of Dy^{3+} ions. The $Fe^{3+} - Dy^{3+}$ exchange interaction is thus renormalized by a few μeV, which modifies the magnetic potential strong enough [inset to

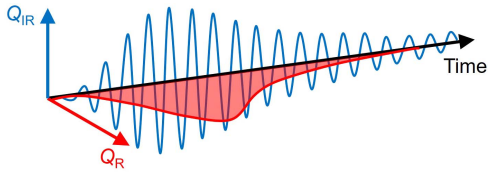

Fig. 24 Solution of Q_{IR} and Q_{R} from Eq. (18) upon pulsed laser excitation whose center frequency is resonant with ω_{IR}[206].

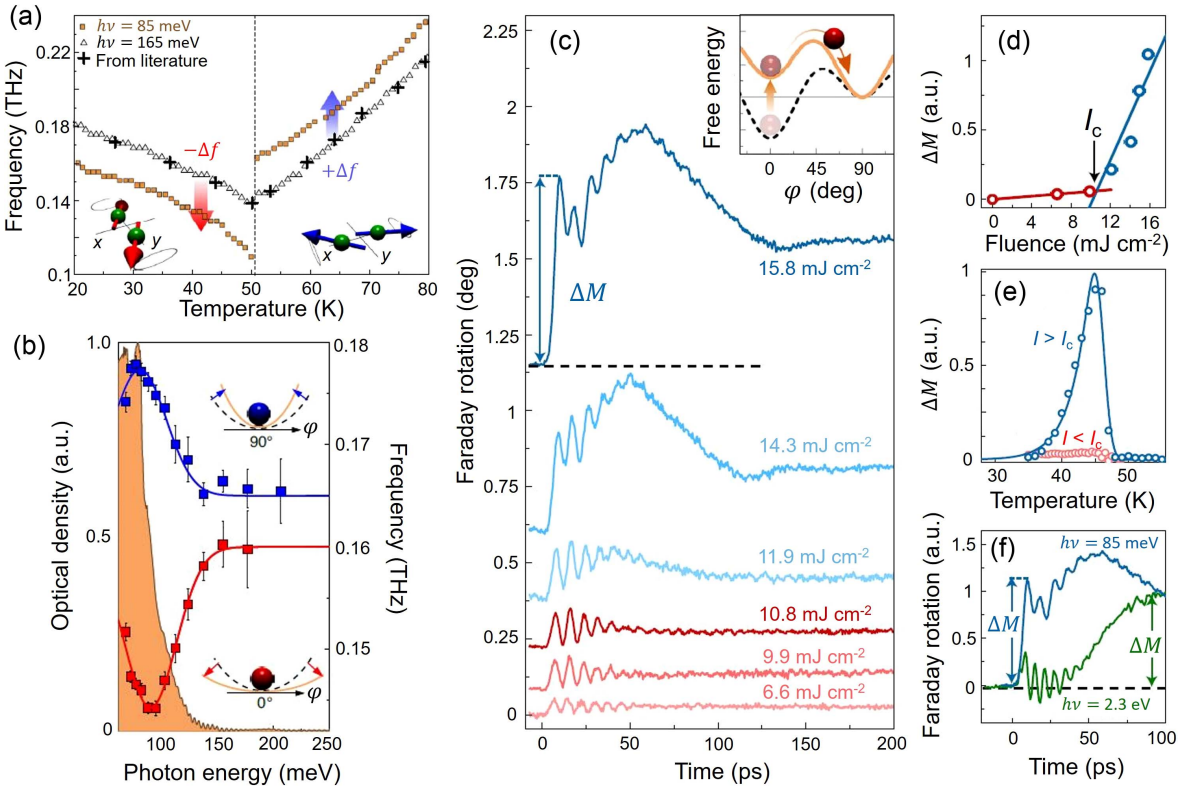

Fig. 25 Nonlinear phononic control of magnetic phases in $DyFeO_3$[238]. (a) Frequency shifts (marked by red and blue arrows) of the quasi-AFM mode due to phonon pumping. (b) Frequency shift as a function of pump photon energy. Shaded curve shows the phonon absorption spectrum. (c) Faraday rotation transients with increasing pump fluence at 45 K. (d) Offset versus fluence. (e) Offset versus temperature for fluences below (red) and above (blue) the threshold. I_c denotes the fluence threshold. (f) Phonon pumping versus charge pumping (ultrafast heating). Reproduced with permission from Ref. [238].

Fig. 25(c)] to induce the SRT. The ultrafast heating mechanism was ruled out through a control experiment where the pump photon energy was tuned to be resonant with the charge gap. As shown in Fig. 25(f), starting from the same initial condition, charge excitation (which is known to generate ultrafast heating) is considerably slower in creating the ΔM offset, compared with the phonon driving scenario. This points again to the usefulness of the dynamical lattice control approach. One interesting detail is that the switched magnetic phase persists for hundreds of ps, even after B_{1u} has stopped ringing and thus A_g distortion is expected to be absent. Similar phenomenology of magnetic dynamics extending beyond the rectified lattice response has also been observed in another experiment[206]. Further work is needed to clarify the underlying mechanism.

The quadratic–linear anharmonic coupling of the type $V_{\text{anh}} \propto (Q_{B_{1u}})^2 Q_{A_g}$ employed by Afanasiev *et al.*[238] creates a distortion along an A_g coordinate, which does not break the symmetry of the crystal. More dramatic dynamical effects are expected if the rectified distortion has an irrep that breaks some symmetries. Radaelli[239] has pointed out that the only scenario in which this can happen for quadratic–linear coupling $V_{\text{anh}} \propto (Q_{\text{IR}})^2 Q_{\text{R}}$ is when the IR active phonon is a degenerate phonon. On the other hand, Juraschek *et al.*[240] have proposed symmetry-breaking nonlinear phononics through trilinear anharmonic coupling, $V_{\text{anh}} \propto Q_{\text{IR}_1} Q_{\text{IR}_2} Q_{\text{R}}$, where IR_1 and IR_2 are two distinct phonons driven by the laser. This does not necessarily require two laser beams in an experiment, especially for orthorhombic systems such as $RFeO_3$.

Juraschek *et al.*[240] have pointed out that since the lattice constants along x and y axes in $RFeO_3$ are similar, the in-plane IR phonons of B_{3u} (polarization along x) and B_{2u} (polarization along y) symmetries are nearly degenerate. This enables driving both B_{3u} and B_{2u} phonons to large amplitudes by aligning the pump polarization in between the x and y axes. The criterion in Eq. (17) can be satisfied with $V_{\text{anh}} \propto Q_{B_{2u}} Q_{B_{3u}} Q_{B_{1g}}$. Notably, the R distortion now has B_{1g} symmetry, which breaks the x–z and y–z mirror planes of the crystal. What makes the proposal more interesting is that the direction of the rectified B_{1g} distortion can be manipulated by the relative phase between B_{3u} and B_{2u} oscillations; this is a feature not afforded by quadratic–linear anharmonic coupling. Using $ErFeO_3$ as an example, the first-principles calculations in Fig. 26 show phonon dynamics under laser driving with different in-plane polarizations. While the A_g distortion (resulting from quadratic–linear coupling) has a fixed sign for 45 deg and −45 deg polarizations, the B_{1g} distortion (from trilinear coupling) clearly switches sign. The possibility of directional control of ultrafast symmetry-breaking lattice distortions has thus been demonstrated.

In fact, an experiment that attempts to simultaneously pump the B_{3u} and B_{2u} phonons in $ErFeO_3$ has already been

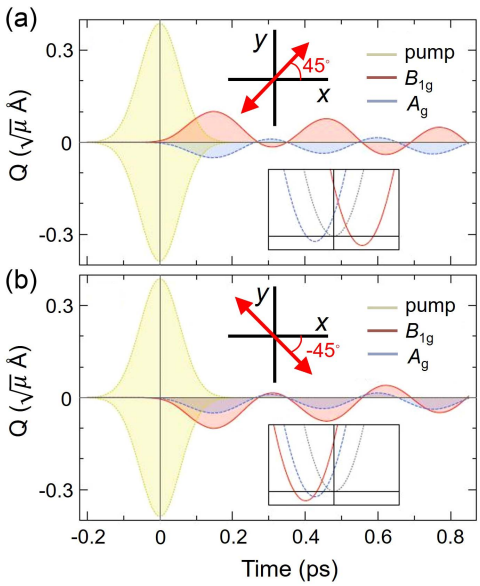

Fig. 26 Evolution of the amplitude of the two Raman modes with (a) 45 deg and (b) –45 deg pump polarizations. Notice the sign change of the B_{1g} mode[240]. Insets show shifts of the free-energy minima of the Raman modes. Reproduced with permission from Ref. [240].

performed by Nova *et al.*[241]. However, instead of observing prominent effects of nonlinear phononics, they discovered a new phonomagnetic effect that was later interpreted within the framework of dynamical multiferroicity[242]. As shown in Fig. 27(a), intense THz fields resonantly drive the two B_u phonons with orthogonal polarizations in a z-cut $ErFeO_3$ in the Γ_4 phase. With appropriate choices of amplitudes and phases, a superposition of the two phonons can provide circular trajectories for the oxygen atoms. Time-reversal symmetry is broken by the circularly polarized phonons, perturbing the magnetic DOF. Coherent quasi-AFM magnon oscillations are excited, whose amplitudes are proportional to the product of the B_{3u} and B_{2u} phonon amplitudes, while no magnon is observed when the pump polarization aligns with one of the crystal axes (driving only one of the two phonons); see Fig. 27(b). Considering the selection rule for the quasi-AFM mode, the magnon excitation can be understood as a result of the generation of a transient effective magnetic field along the z axis from the circularly polarized phonons in the x–y plane. The effective magnetic field, written as $H_z^{\text{eff}} = -i\alpha_{xyz}Q_{ux}Q_{uy}$, resembles the form of IFE in Table 2, with the only difference that the phonon coordinates replace the laser electric fields in the original expression. The phenomenon is therefore termed the phonon IFE[243].

Juraschek *et al.*[242] later placed the phonon IFE in a general framework called dynamical multiferroicity. They pointed out that, in a way similar to how symmetry arguments predict a spatially varying magnetization $\boldsymbol{M}$ to produce polarization $\boldsymbol{P}$ as $\boldsymbol{P} \sim \boldsymbol{M} \times (\nabla \times \boldsymbol{M})$, the reciprocal effect, where $\boldsymbol{P}$ produces $\boldsymbol{M}$, should also be allowed. The authors provided

$$\boldsymbol{M} \sim \boldsymbol{P} \times (\partial_t \boldsymbol{P}). \tag{19}$$

Therefore, a time-varying polarization should be able to generate a finite magnetization.

Applying this expression to the experiment by Nova *et al.*[241], one can write the in-plane polarizations induced by in-plane phonons as

$$\boldsymbol{P} = \begin{pmatrix} P_1(t) \\ P_2(t) \end{pmatrix} = \begin{pmatrix} A_1 \sin(\omega_1 t) \\ A_2 \sin(\omega_2 t) \end{pmatrix}, \tag{20}$$

where A_1 (A_2) and ω_1 (ω_2) are the amplitude and frequency of the B_{3u} (B_{2u}) phonon, respectively. From Eq. (19), this gives

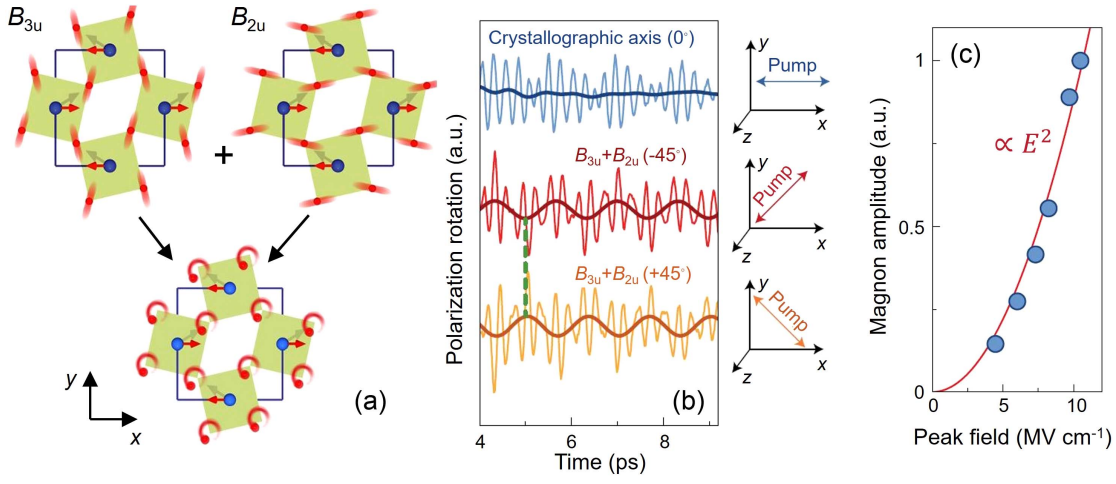

Fig. 27 Phonon IFE in $ErFeO_3$[241]. (a) Eigenvectors of in-plane IR phonons, and their superposition. (b) Time-resolved Faraday rotation transients under different THz pump polarizations. Oscillations contain fast Raman phonons and the slow quasi-AFM magnon (outlined by thick solid curves). No magnon is observed when the pump polarization aligns with a crystal axis. (c) Quadratic dependence of magnon amplitude on the pump field. Reproduced with permission from Ref. [241].

$$\boldsymbol{M}(t) \sim \left[\frac{\omega_+}{2}\sin(\omega_- t) - \frac{\omega_-}{2}\sin(\omega_+ t)\right] A_1 A_2 \hat{z}, \tag{21}$$

where there are two oscillation components. The one at the difference frequency $\omega_- = \omega_1 - \omega_2$ oscillates with a larger amplitude ($\propto \omega_+$), while the other at the sum frequency $\omega_+ = \omega_1 + \omega_2$ oscillates with a smaller amplitude ($\propto \omega_-$). In $ErFeO_3$, $\omega_1/2\pi = 17$ THz, $\omega_2/2\pi = 16.2$ THz, giving the large-amplitude oscillation of $\boldsymbol{M}(t)$ to be at $\omega_-/2\pi = 0.8$ THz. Juraschek *et al.*[242] mentioned that the frequency of $\boldsymbol{M}(t)$ satisfies the resonant condition with the quasi-AFM mode (0.75 THz) of $ErFeO_3$, which explains the observation of magnons by Nova *et al.*[241]. Furthermore, the fact that $\boldsymbol{M}(t)$ in Eq. (21) is along the crystal z axis and is proportional to the product A_1A_2 is consistent with the phonon IFE picture and the observation of the quadratic dependence of the magnon amplitude on the pump field [Fig. 27(c)].

Phonomagnetic effects therefore present themselves as a powerful alternative for achieving laser manipulation of magnetic order, and a variety of phenomena are expected, since every photomagnetic effect in Table 2 can have a phonon analog. Furthermore, realistic calculations have shown that for comparable pulse energies, phonomagnetic effects can sometimes generate considerably larger effective fields compared with photomagnetic effects[243]. This further widens the applicability of this technique to dynamical material engineering.

4.4 Rare-Earth Pathways

An alternative approach for inducing SRTs in $RFeO_3$ is to resonantly pump a certain resonant transition of the R^{3+} ions. The magnetic anisotropy of $RFeO_3$ is determined by the magnetic coupling between the R^{3+} and Fe^{3+} moments. While the spin of Fe^{3+} can be viewed as a constant, the moment of R^{3+} is a sensitive function of temperature, owing to the thermal population of the ions within its crystal-field-split levels (separated by ~meV, which is the thermal energy scale of a few tens of Kelvin). The temperature dependence thus enters the $R^{3+} - Fe^{3+}$ coupling, and thereby causes the strong temperature dependence of magnetic anisotropy. An idea then arises, asking whether magnetic anisotropy can be transiently manipulated by a nonthermal distribution of R^{3+} in its crystal-field-split levels driven by laser pulses.

Baierl *et al.*[244] have verified this proposal in $TmFeO_3$. The $^3H_6$ ground state of the Tm^{3+} ions in $TmFeO_3$ is fully split by the low-symmetry crystal-field into singlets with energy separations of the order of 1–10 meV; see Subsection 3.2. When an intense THz pulse resonantly excites the electric-dipole-active transitions between the crystal-field-split levels, the Tm^{3+} ions are driven into an excited state with a nonthermal population distribution; see Fig. 28(a). This affects the strength of $Tm^{3+} - Fe^{3+}$ coupling, leading to a modification to the magnetic anisotropy and setting a new easy axis for the Fe^{3+} spins. Since the new easy axis deviates from that in equilibrium, magnon oscillations are launched, as shown by the Faraday rotation traces in Fig. 28(b). Notably, as the intensity of the pump THz field increases (up to 0.3 T in peak magnetic field), the time-domain magnon waveform clearly develops nonlinearity, with an increasingly prominent low-frequency component emerging from a fast-oscillating background. A frequency-domain analysis of the magnon modes shows that it is the quasi-FM mode that follows a nonlinear amplitude scaling relation with the pump field [Figs. 28(c) and 28(d)]. The nonlinear excitation of magnons falls outside the description of the Zeeman-torque-type excitation in the weak THz field limit, and therefore, is a unique manifestation of THz-field-induced magnetic anisotropy change. What further corroborates this interpretation is the temperature dependence of the nonlinearity in exciting the quasi-FM mode. Since the static anisotropy is close to zero in the SRT temperature range, laser-induced anisotropy modification is expected to be dominant in the Γ_{24} phase; this is indeed observed [Fig. 28(e)].

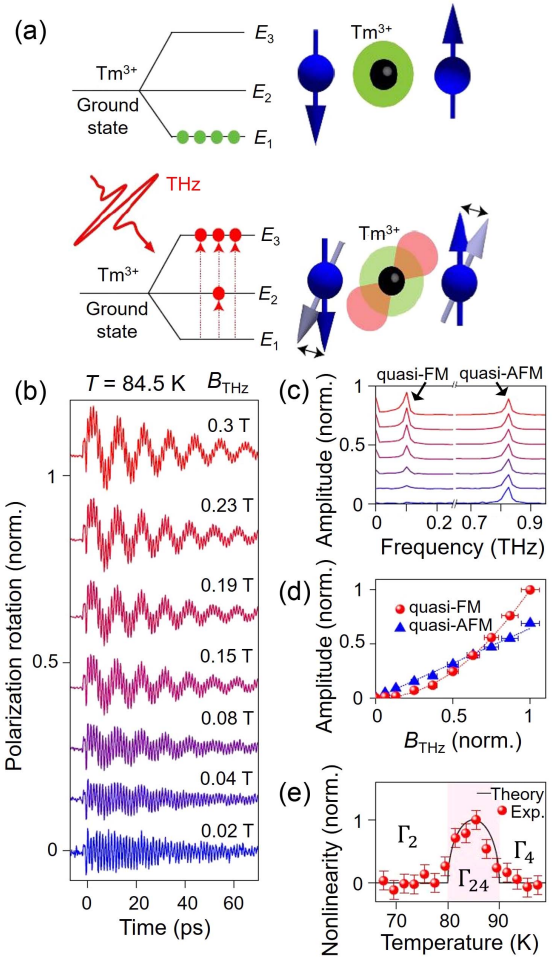

Fig. 28 Nonlinear excitation of magnons by pumping rare-earth crystal-field transitions[244]. (a) Intense THz pump repopulates Tm^{3+} ions within its crystal-field levels, which in turn modifies the magnetic anisotropy. (b) Faraday rotation transients under increasing THz pump fields. (c) Fourier transform of (b). (d) Spectral weights of the quasi-FM and quasi-AFM modes extracted from (c). (e) Nonlinearity of quasi-FM excitation versus temperature. Reproduced with permission from Ref. [244].

Laser-induced SRTs through the rare-earth pathway and the ultrafast heating pathway both rely on modification of the magnetic anisotropy. However, the advantage of the rare-earth pathway is that it is more direct, and the onset of anisotropy modification is expected to be instantaneous. On the contrary, in the case of ultrafast heating, one would need to rely on the R^{3+}–lattice coupling [Fig. 18(e)], whose speed is sometimes bottlenecked in certain R^{3+} species.

Recently, Fitzky *et al.*[245] have compared the rise times of anisotropy modification for the rare-earth pathway and the ultrafast heating pathway. As shown in Fig. 29(a), in a z-cut $Sm_{0.7}Er_{0.3}FeO_3$ crystal, mid-IR pump fields centered at 25 THz and 33 THz were used to pump optical phonons and Sm^{3+} $^6H_{5/2} \rightarrow {}^6H_{7/2}$ transitions, respectively. The temperature was tuned to the SRT range to cause the effect of laser-induced magnetic anisotropy change to stand out. Within the SRT range (310–330 K), the orientation of the easy axis for spins can be directly correlated with the anisotropy; this scenario is similar to that proposed by Baierl *et al.*[244]. The offset structure developed in a Faraday rotation signal probes laser-induced spin rotation, which, on the scale of a 100 ps window, looks similar for 25 THz pumping and 33 THz pumping [Fig. 29(b)]. However, a closer comparison of the time dynamics in Fig. 29(c) shows that the onset of spin rotation is much quicker for the 33 THz pump than for the 25 THz pump. Such dynamics of spin rotation directly reveal the time scale for setting the transient magnetic anisotropy. As shown in Fig. 29(d), the rise time of anisotropy modification is nearly zero (instantaneous) for the 33 THz pump but can be as long as 20 ps for the 25 THz pump for certain temperatures. The 20 ps rise time is exactly the time needed for the lattice heat generated by the 25 THz phonon pumping to be transferred to the Sm^{3+} subsystem [Fig. 29(a), dashed arrow], as expected for the ultrafast heating scenario. This observation therefore shows that rare-earth pumping is a more direct pathway of manipulating magnetic anisotropy and realizing a laser-induced SRT.

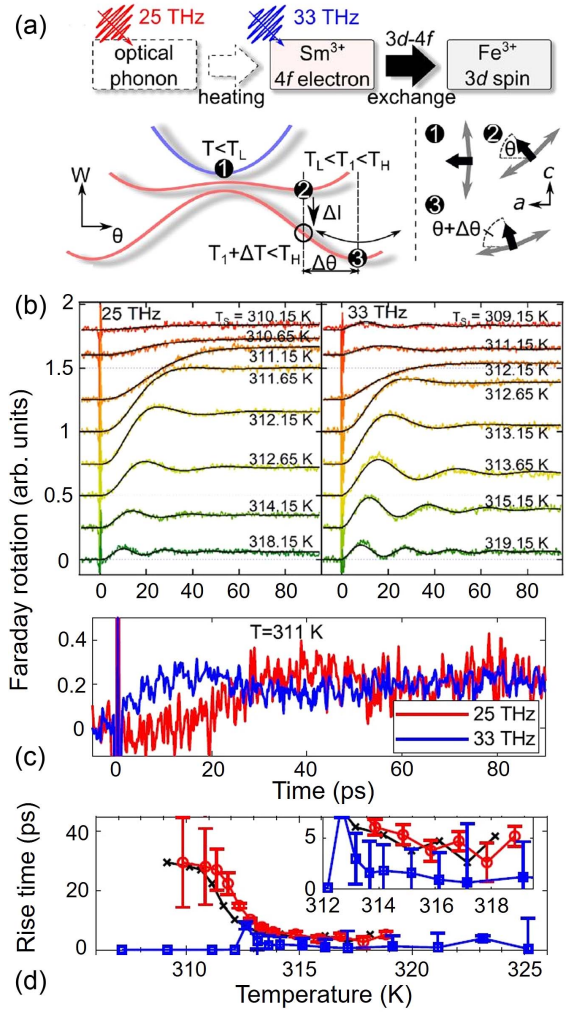

Fig. 29 Comparing the onset of magnetic anisotropy due to rare-earth pumping and phonon pumping[245]. (a) Pathway that leads to anisotropy modification. 25 THz pump drives optical phonons, while 33 THz pump drives Sm^{3+} atomic transitions. Lower: anisotropy energy landscape within the SRT temperature range. Orientation of the easy axis is parameterized by θ. Under laser illumination, the easy axis switches to a new direction of $\theta + \Delta\theta$. (b) Faraday rotation transients at various temperatures within the SRT range for a 25 THz pump and a 33 THz pump. (c) Detailed comparison of the rise time of the offset signal. (d) Rise time for establishing anisotropy for the two types of pumps. Blue: 33 THz pump. Red: 25 THz pump. Inset zooms into the 312–320 K range. Reproduced with permission from Ref. [245].

Laser-induced SRTs represent just one of the many examples where R^{3+}–Fe^{3+} interaction can be utilized to achieve interesting physics in $RFeO_3$. In a broader context, it points to a variety of possibilities towards engineering magnetic properties of compounds that harbor both a rare-earth subsystem and a transition-metal spin system; examples include relaxation of optical selection rules of electromagnons[246], cooperative quantum coupling[169] that we will cover in depth in Section 6, and coherent manipulation of spin-wave amplitudes[247]. The R^{3+}–Fe^{3+} interaction is therefore a property that one should always keep in mind while developing protocols for laser control of $RFeO_3$.

4.5 Floquet Pathways

In recent years, Floquet engineering has emerged as a promising tool for controlling quantum many-body systems. The idea is to utilize time-periodic driving conditions to modulate orbital states and dynamically renormalize microscopic interaction parameters in quantum materials, thereby achieving active control of their properties or eliciting novel functionalities that are inaccessible in equilibrium. Since the oscillating electromagnetic fields of radiation provide an ideal source of time-periodic potentials, Floquet engineering of quantum materials in the context of light–matter interaction has invoked a variety of novel ideas and concepts, including band structure engineering[29,248–252], electronic topology[253–255], magnetic correlations[213,215,256–259], and discrete time crystals[260]. Floquet engineering of magnetism is arguably the most exciting proposal with practical applications.

Here, we will first briefly introduce the basics of Floquet theory, following Refs. [261,262]. Given a time-periodic Hamiltonian $H(t) = H(t+T)$, where T is the period, the evolution of the system can be expanded in the basis of Floquet states $|\psi_n(t)\rangle$. Since the Schrödinger equation of $H(t)$ can be viewed as a time-domain analog to the problem of solving a spatially periodic Hamiltonian [which gives the Bloch theorem $\varphi_k(x) = e^{-ikx}u(x)$ for crystals], the solution to $H(t)$ is similar in format to the Bloch's theorem. The ansatz reads

$$|\psi_n(t)\rangle = e^{-i\varepsilon_n t/\hbar}|\phi_n(t)\rangle, \tag{22}$$

where ε_n is the quasienergy, and $|\phi_n(t)\rangle$ is a periodic function $|\phi_n(t)\rangle = |\phi_n(t+T)\rangle$ that plays the same role as $u(x)$ in the Bloch theorem. We then write $|\phi_n(t)\rangle$ in Fourier series in terms of harmonics of the driving frequency, $\omega = 2\pi/T$, as

$$|\phi_n(t)\rangle = \sum_m e^{-im\omega t}|\phi_n^{(m)}\rangle, \tag{23}$$

where $|\phi_n^{(m)}\rangle$ is the coefficient of the mth harmonic. By using Eqs. (22) and (23), the time-dependent Schrödinger equation becomes

$$(\varepsilon_n + m\hbar\omega)|\phi_n^{(m)}\rangle = \sum_{m'} H^{(m-m')}|\phi_n^{(m')}\rangle, \tag{24}$$

where $H^{(m)} = (1/T)\int_0^T \mathrm{d}t e^{im\omega t}H(t)$ are the Fourier components of the Hamiltonian. Derivation of Eq. (24) suggests that the time-dependent problem has been converted into a time-independent one in an enlarged Floquet space.

The solutions for the quasienergy in Eq. (24) can be obtained by diagonalizing the matrix equation[262]

$$\mathcal{H}\varphi_n = \varepsilon_n\varphi_n, \tag{25}$$

where

$$\mathcal{H} = \begin{pmatrix} & H^{(-1)} & H^{(-2)} & \\ H^{(1)} & H^{(0)} - m\hbar\omega & H^{(-1)} & H^{(-2)} \\ H^{(2)} & H^{(1)} & H^{(0)} - (m+1)\hbar\omega & H^{(-1)} \\ & H^{(2)} & H^{(1)} & \end{pmatrix},$$

$$\varphi_n = \begin{pmatrix} \vdots \\ |\phi_n^{(m)}\rangle \\ |\phi_n^{(m+1)}\rangle \\ \vdots \end{pmatrix}. \tag{26}$$

The enlarged basis vector φ_n is constructed by stacking up $|\phi_n^{(m)}\rangle$ for various orders. Furthermore, each entry of $\mathcal{H}$ in Eq. (26) represents a matrix of dimension d, which is the dimension of the original Hilbert space specified by $H(t)$. The dimension of $\mathcal{H}$ should be infinite due to the infinite number of Floquet sectors, but to perform diagonalization, the matrix needs to be truncated up to the Nth Floquet sector (while making sure that N is large enough to make the results converge), so the dimension of the actual matrix to diagonalize would be $N \times d$.

Using the method above, Mentink *et al.*[256] have theoretically proposed Floquet engineering of exchange interactions between spins in Mott insulators. The minimal Hubbard model for a Mott insulator reads

$$H = -t_0\sum_{\langle ij\rangle\sigma} c_{i\sigma}^\dagger c_{j\sigma} + U\sum_j n_{j\uparrow}n_{j\downarrow}, \tag{27}$$

where t_0 is the nearest-neighbor hopping, $c^\dagger$ (c) is the electron creation (annihilation) operator, $\sigma = \uparrow, \downarrow$ is the spin index, U is the onsite Coulomb repulsion, and n is the density operator. The authors considered a two-site cluster model filled with two electrons (half filling), which is exactly solvable, and later found that the simple model is able to capture all the essential Floquet physics that would be expected for a full lattice[256]. Therefore, we will consider only the two-site model here.

In the atomic limit ($t_0 = 0$), the electronic states are $|\uparrow,\downarrow\rangle$ and $|\downarrow,\uparrow\rangle$ at $E_1 = 0$, and $|\uparrow\downarrow,0\rangle$ and $|0,\uparrow\downarrow\rangle$ at $E_2 = U$. Turning on the hopping term ($t_0 \neq 0$) lifts the degeneracy, producing the singlet state at $E_S = -4t_0^2/U$ and the triplet state at $E_T = 0$ as the lowest-energy states; their energy separation $E_T - E_S$ is twice the exchange interaction, $2J_{ex}$. The periodic light field drive is considered by using a Peierls substitution $t_0 \to t_0 \exp[ieaA_{ij}(t)]$, where e is the electron charge, a is the lattice constant, and A is the vector potential of light. The new time-dependent Hamiltonian can be used to derive the mth Fourier component $H^{(m)}$, which can then be plugged into Eq. (26) for a full solution of the quasienergies (among which E_T and E_S are most important).

Figures 30(a) and 30(b) show how E_T, E_S, and $J_{ex} = (E_T - E_S)/2$ depend on the Floquet parameter $\mathcal{E} = eaE/\hbar\omega$ (E being the light field amplitude), which is nothing but the ratio of the Bloch frequency to the driving frequency. Depending on the pump frequency ω and the range, the Floquet drive can lead to either an increase or decrease in J_{ex}, representing strengthening or weakening of the AFM correlation. For certain regimes of $\mathcal{E} > 1$, the sign of J_{ex} is reversed upon increasing field strength, suggesting a transition into an FM-type correlation. Since dynamical modification of J_{ex} is expected to cause dramatic impacts on the magnetic order, this set of calculations[256], derived from the simple cluster model and light-induced hopping renormalization, has profound implications to future experimental attempts. An important guidance one can obtain, for example, manifests in the choice of pump photon energy. In experiments, because pump fields used in Floquet engineering are usually strong, it is essential to tune the pump energy (ω) to be off resonance with the charge gap (U) to avoid heating effects arising from charge excitation processes. Figure 30(b) further compares the distinct effects of overgap ($\omega > U$) and subgap ($\omega < U$) pumps in the small $\mathcal{E}$ regime. The overgap pump initially decreases J_{ex} while the subgap pump initially increases J_{ex}; this provides the opportunity for bidirectional control of exchange interaction by adjusting the pumping frequency.

On the other hand, Chaudhary *et al.*[263] have taken the orbital DOF into account and proposed the concept of orbital Floquet engineering of magnetism. For most Mott insulating crystals, say, TM compounds, the spin exchange between TM spins is mediated by ligand ions. In addition, TM ions, being placed

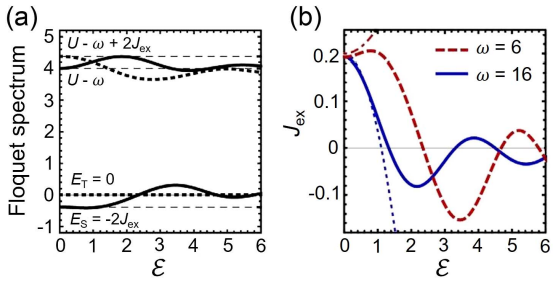

Fig. 30 Floquet spectrum and exchange interaction energy of a two-site cluster Hubbard model[256]. (a) Energy-level structure versus the Floquet parameter $\mathcal{E}$. (b) Exchange interaction versus $\mathcal{E}$ for two pumping frequencies. The unit is the hopping amplitude t_0. Onsite repulsion is assumed to be $U = 10$. The red dashed-dotted line and blue dashed line are obtained with perturbation theory (valid for $\mathcal{E} \ll 1$). Reproduced with permission from Ref. [256].

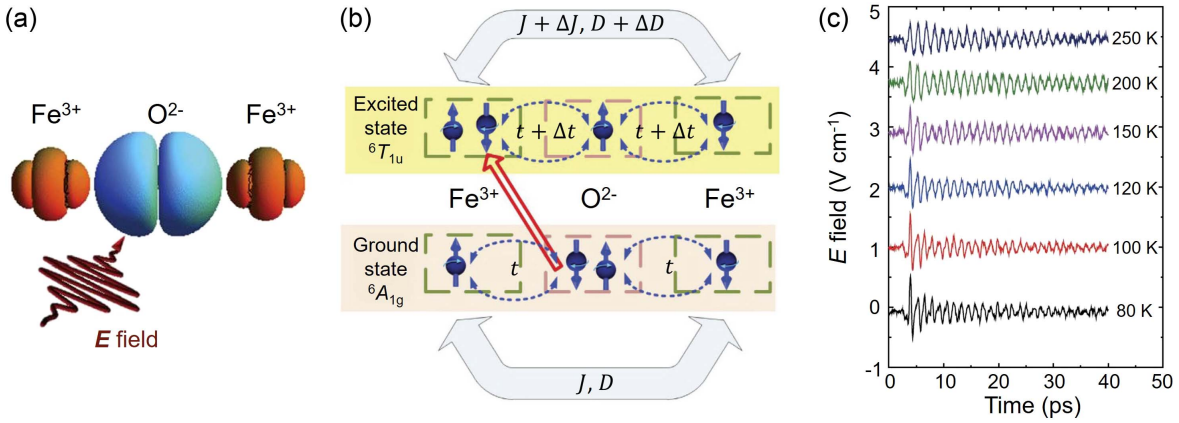

Fig. 31 Floquet modification of exchange interaction in $RFeO_3$[123]. (a) Infrared pump pulses (centered at 1.55 eV) nonresonantly drive a Fe-O-Fe cluster. (b) Ultrafast modification of exchange interaction is due to virtual charge transfer arising from light-induced orbital state mixing. (c) Temperature-dependent THz emission signal for $ErFeO_3$. Reproduced with permission from Ref. [123].

in strong crystal-field environments themselves, can have distinct orbital ground states and energy-level configurations. Therefore, supplying Floquet drives to either ligand orbitals or TM orbitals is expected to cause orbital inter-mixing, and in turn, modify the exchange interaction J_{ex}. Using fourth-order perturbation theory, Chaudhary *et al.*[263] have given analytical expressions of $\Delta J_{ex}/J_{ex}$, the percentage change in J_{ex}, due to various types of laser drives. After taking realistic parameters into account, they found that both schemes (pumping ligands or pumping TMs) are challenging for experiments, due to either insufficient transition dipole moments or the requirement to use unusually high pumping frequencies, which, in most experimental situations, cause significant heating effects. However, they found that orbital hybridization caused by vibrational motions arising from certain coherent Raman phonons can produce large $\Delta J_{ex}/J_{ex}$; the required pumping conditions are also realistic. Since the time periodicity of the Floquet drive in this case is supplied by coherent phonons rather than laser fields, the proposal represents a unique example of "phonon Floquet physics."

To date, there has been limited success in experimental demonstrations of Floquet engineering of magnetism. Using $RFeO_3$ as a material platform, Mikhaylovskiy *et al.*[123] have reported THz emission signatures of Floquet modification of exchange interactions. As shown in Fig. 31(a), the superexchange interaction between Fe^{3+} spins in $RFeO_3$ is mediated by O^{2-} ligands. A nonresonant laser drive creates virtual excitations to the excited level, that is, the charge-transferred orbital configuration of the Fe-O-Fe cluster [Fig. 31(b)]. This leads to Rabi splittings and a coherent mixing of the ground state and the excited state of the cluster, thereby providing an instantaneous modification to the exchange interaction. Mikhaylovskiy *et al.*[123] proposed that the coherent light–spin interaction should obey the interaction Hamiltonian

$$H_I = I_{opt}\alpha\sum_{i,j}(\boldsymbol{S}_i \cdot \boldsymbol{S}_j) + 2I_{opt}\boldsymbol{\beta} \cdot \sum_{i,j}(\boldsymbol{S}_i \times \boldsymbol{S}_j), \tag{28}$$

where I_{opt} is light intensity, and α and $\boldsymbol{\beta}$ are scalar and vector coefficients, respectively. When H_I is added to the equilibrium spin Hamiltonian of $RFeO_3$, the first (second) term in H_I leads to an effective change to the symmetric (antisymmetric) exchange integral, $\Delta J = \alpha I_{opt}$ ($\Delta \boldsymbol{D} = \boldsymbol{\beta} I_{opt}$). As the ratio D/J determines the canting angle of Fe^{3+} spins, the Floquet engineered ratio, $(D + \Delta D)/(J + \Delta J)$, would deviate from the equilibrium value (D/J), providing an impulsive torque to change the canting angle, and thereby, launching the quasi-AFM mode. As shown in Fig. 31(c), the quasi-AFM mode is indeed observed in THz emission measurements performed on $ErFeO_3$. The mode amplitude does not show prominent dependence on temperature, even across the SRT; this is in contrast to quasi-FM magnons typically launched by ultrafast heating, where the magnon amplitude is largest around the SRT temperature. Furthermore, a unique feature of the interaction Hamiltonian in Eq. (28) is that the interaction is isotropic, meaning that it depends only on the light intensity, but remains insensitive to the pump light polarization and propagation direction. This is also found to be consistent with experiments[123], and distinguishes the Floquet mechanism from photomagnetic effects such as the IFE and ICME, which rely sensitively on the helicity and polarization of the pump light.

Floquet engineering of magnetism is a rapidly developing field. With theoretical models that take more material details into account, say, through first-principles calculations[215], the proposed novel phenomena would be closer to experimental demonstrations. On the experimental side, in addition to ultrafast optics, a variety of time-resolved scattering techniques[116,258,264] may have the capability to detect the coherent manipulation of magnetic order, fostering more ways for experiment–theory comparisons. This field is therefore expected to see more interesting results and fruitful collaborations in the future.

5 Antiferromagnetic Spintronics and Coherent Magnonic Control

Spintronics refers to a field of study that aims to harness electron spins as the information carrier in computational devices[2,3,265]. Spintronic devices and systems are expected to bring revolutionary developments to multiple technological applications related to magnetism, including magnetic recording, sensing, and logical applications, and are believed to hold the

potential to complement the existing semiconductor-based microelectronic industry in next-generation information technology. In the past, the choice of material platforms for performing specific spintronic tasks has predominately been solid-state crystals or films with FM ordering[266–269]. However, the past 10 years has witnessed a surging interest in promoting AFM materials to take this central role, establishing the subfield of AFM spintronics[4,5,67–69,270,271].

Several notable advantages have been identified for antiferromagnet-based spintronics compared to their ferromagnet counterparts. Their imperviousness to external magnetic field fluctuations improves the robustness of information storage. They are more naturally abundant, meaning a wider variety of materials with distinct properties are within the library to choose from. Further, their intrinsically faster response times, set by the magnon frequency and the exchange energy scale, are expected to increase the operation speeds of devices by up to three orders of magnitude.

Experimental efforts to date have been devoted to finding methods for efficiently reading and writing AFM states, in which AFM insulators and metals play different roles. For AFM metals, such as Mn_2Au and CuMnAs, significant attention has been paid to using electrical current as a direct switch of AFM states. Breakthrough discoveries for efficient switching protocols include spin–transfer torque and spin–orbit torque[272,273], both of which can generate staggered local effective fields that are commensurate with the periodicity of AFM sublattices, and thereby, incur much more efficient switching than external uniform fields. On the other hand, AFM insulators are particularly suitable for magnonics applications[4,7]. This subfield of spintronics is concerned with what comes after a spin perturbation (in the form of magnons) is made to an AFM material, and how the magnon excitation can be utilized to the largest extent to transport and process information, especially under the general framework of wave-based computing technologies. Insulators are well suited for magnonics due to their capability of maintaining spin coherence and minimizing energy dissipation due to Ohmic losses. In addition, AFM insulators also find more frequent applications in interfacing optical systems with magnonic devices, since magnons can be selectively excited by THz radiation while accidental excitation of charge carriers is suppressed.

$RFeO_3$ clearly falls under the category of AFM insulators that possess huge application potential in THz-frequency magnonic devices. Therefore, the purpose of this section is to review various tools discovered so far for exciting, propagating, and manipulating coherent magnons in $RFeO_3$, with special emphasis on how they can facilitate realistic applications. Topics for this review are restricted to $RFeO_3$ systems and include coherent magnon amplitude control through double-pulse interference, magnon-polaritons and magnon propagation effects, $RFeO_3$/FM metal heterostructuring as a means for efficient magnon excitation and SRT control, and finally, nonlinear magnonics. Most of these topics are still at the fundamental physics level. To meet the demands of industrial technology, a number of challenges at both device and system levels need to be addressed[274]. Spin–charge interconversion between metallic and insulating AFM components and interfacing these spintronic subsystems with CMOS electronics remain as two important issues. In addition, the fact that AFM spintronics operates in the THz frequency range poses the need to develop, on a parallel channel, on-chip THz components and ultrafast circuits, for device miniaturization and scalability. Nevetheless, the fundamental physics principles presented here provide important clues for engineers to take the most important steps towards the goal.

Before going into the detailed discussion, we first demonstrate the high quality factors (Q factors) of the $RFeO_3$ magnons. This is the most important fact because none of the proposals in magnonics that follow would be possible without a demonstrated record of ultrahigh Q factors of magnons in the host materials. Figure 32(a) is a table that summarizes magnon frequencies f and linewidths Δf [in full width at half maximum (FWHM)], and the corresponding Q factors $Q = f/\Delta f$ for various $RFeO_3$ crystals at room temperature. The data were obtained in the last century by a frequency-domain far-IR spectroscopy instrument with an outstanding frequency resolution, and were summarized by Balbashov *et al.*[140]. $YFeO_3$ stands out by showing $Q > 300$ for the quasi-FM mode and $Q > 250$ for the quasi-AFM mode. More recently, an even higher value of $Q > 1000$ has been demonstrated by Watanabe *et al.*[275] in a

(a)

Crystals	quasi-FM mode			quasi-AFM mode		
	f (GHz)	Δf (GHz)	Q	f (GHz)	Δf (GHz)	Q
$YFeO_3$	299.4	0.9	332. 7	526.8	2.1	250.8
$TmFeO_3$	402	7.5	53.6	698	8.4	83.1
$DyFeO_3$	379.5	10.5	36.1	510	10.5	48.6
$GdFeO_3$	305	12	25.4	605.7	13	46.6
$HoFeO_3$	378	15	25.2	597	9	66.3
$ErFeO_3$	377	8	47.1	673	7	96.1
$TbFeO_3$	322	20	16.1	537	15	35.8

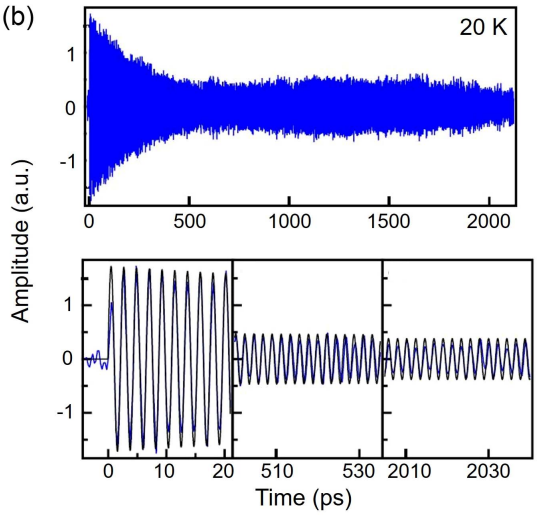

Fig. 32 High Q factors of THz magnons in $RFeO_3$. (a) Table summarized using data from Ref. [140], which lists frequency f, linewidth Δf (in FWHM), and Q factor for quasi-FM and quasi-AFM magnons in various $RFeO_3$ crystals at room temperature. (b) Long-lived temporal oscillations due to quasi-FM magnons in $ErFeO_3$ at 20 K[275]. The bottom row shows zoom-in views of –4–21 ps, 500–535 ps, and 2005–2040 ps. Reproduced with permission from Ref. [275].

high-quality $ErFeO_3$ crystal cooled to 20 K; see Fig. 32(b) for a time-domain quasi-FM oscillation signal that lasts for at least 2 ns. Such a high Q factor readily exceeds typical Q factors (of 10–100) for other model AFM insulators such as oxides NiO/MnO[276,277] and difluorides $MnF_2/FeF_2/CoF_2$[278,279], and even approaches that of yttrium iron garnet[280–282], a material widely applied in microwave magnonics due to its exceptionally low damping rates. The high Q factor ensures good spatial and temporal coherence, thereby setting the stage for $RFeO_3$ to play a central role in THz-frequency magnonic devices in the future.

5.1 Magnon Amplitude Control through Double-Pulse Interference

We first describe previous work demonstrating control of magnon amplitude by interference effects. To observe this phenomenon directly in the time domain using ultrashort laser pulses, it is important to first clarify a concept called the FID, which we briefly mentioned in Section 3 but did not elaborate on. FID signals appear in the context of interaction between an ensemble of two-level systems (TLSs) with a pulsed light field whose frequency is tuned near resonance with TLS spacing. For spin systems (since they are TLSs, with spin up and down being the two levels), the status of the spin ensemble can be represented by a Bloch vector, which develops a tilt away from its equilibrium orientation after the impulsive laser–spin interaction. The Bloch vector then precesses around the equilibrium orientation, leading to emission of a light field that persists until the Bloch vector decays back to the equilibrium state. The FID is defined as the subsequent emission field by the oscillating Bloch vector after the impulsive laser drive.

Coherent control of magnons refers to coherent control of FID signals arising from magnon oscillations, which is useful in magnonic logic gates compatible with wave-based computation protocols[6–10]. When binary data are encoded into the magnon amplitude, a Mach–Zender-type interferometer setup, depicted in Fig. 33(a), can be used to achieve NOT and XNOR gates[7,283]. The idea is to split a magnon wave into two branches, each complemented by a phase shifter, and combine the phase-shifted signals from the two branches into one at the output. Such an interferometer setup can be effectively demonstrated by an optical experiment with double-pulse pumping capabilities, as we discuss below.

Yamaguchi *et al.*[284] have demonstrated coherent control of magnon FID signals through interference in a double-pulse pumping experiment on $YFeO_3$. Two THz pulses with controllable delay excite two sets of FID oscillations with a controllable phase shift, exactly mimicking the two branches of magnons that propagate within a Mach–Zender-type interferometer. The detector reads a superposition of the two FID signals in the time domain. The pump polarization is first aligned along a direction of the crystal to enable simultaneous excitation of both quasi-FM and quasi-AFM modes by a single pulse. As shown in Fig. 33(b), when double-pulse pumping is used, one of the two modes can be selectively suppressed by destructive interference, which is achieved by setting the inter-pulse time delay to be half-integer multiples of the magnon oscillation period. The authors then switched to a new configuration where only the quasi-FM mode can be excited, and the coherent control of FID amplitude through constructive or destructive interference is again demonstrated; see Figs. 33(c) and 33(d) for how time- and frequency-domain FID amplitudes evolve with inter-pulse delay. In addition, energy restoration back to the radiation field due to destructive interference of magnons is also demonstrated. As shown in Fig. 33(e), when the second pulse is examined, its integrated energy (represented by the peak) is higher for the double-pulse pumping scenario in which the magnon launched by the first pulse is quenched by the second pulse

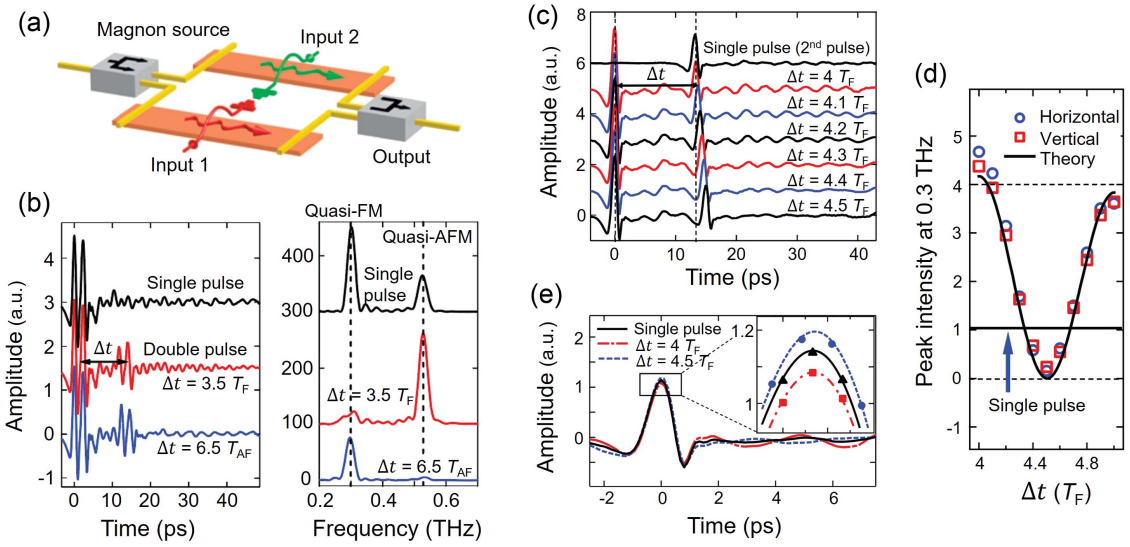

Fig. 33 Double-pulse coherent control of magnons in $YFeO_3$[284]. (a) Mach–Zender-type interferometer setup used to achieve NOT and XNOR gates[7,283]. (b) Double-pulse pumping experiment on an *x*-cut crystal. Left: time-domain signals with single-pulse and double-pulse excitations. Right: Fourier transform of the FID signal. (c) Coherent control of the quasi-FM mode in a *z*-cut crystal. THz electric field is parallel along the *y* axis. (d) Fourier transform of the FID signal in (c) versus inter-pulse time delay. (e) Energy lost in the magnon sector due to destructive interference is restored back to the second pulse. Reproduced with permission from Refs. [7,284].

due to destructive interference. This suggests that the energy lost in the spin sector is transferred back to the radiation field, manifesting as an energy gain by the second pulse.

Jin *et al.*[285] have subsequently developed another protocol that enables a double-pulse coherent control experiment by using only a single THz pulse. The key idea is to utilize the crystal anisotropy to split the pulse in two with perpendicular polarizations and mismatched velocities. As shown in Fig. 34(a), a THz pulse incident onto a z-cut $YFeO_3$ crystal is polarized in the x–y plane; the angle formed by the THz electric vector and the y axis is θ. In this configuration, only the quasi-FM mode can be excited, and tuning θ leads to a branching of power according to

$$E_x(0) = E_{\mathrm{THz}}^{\mathrm{in}} \sin\theta,$$
$$E_y(0) = E_{\mathrm{THz}}^{\mathrm{in}} \cos\theta, \tag{29}$$

where $E_x(0)$ and $E_y(0)$ represent the electric field amplitude along x and y axes at the incident surface, respectively, and $E_{\mathrm{THz}}^{\mathrm{in}}$ is the incident field amplitude. The fields E_x and E_y then propagate with distinct speeds in the crystal with thickness d, so that at the exit,

$$E_x(d) = E_{\mathrm{THz}}^{\mathrm{in}} \sin\theta e^{-\alpha_x d/2} e^{i\omega n_x d/c},$$
$$E_y(d) = E_{\mathrm{THz}}^{\mathrm{in}} \cos\theta e^{-\alpha_y d/2} e^{i\omega n_y d/c}, \tag{30}$$

where $\alpha_{x(y)}$ and $n_{x(y)}$ are the absorption coefficient and refractive index along the x (y) axis, respectively, ω is the angular frequency, and c is the speed of light. The output THz signal at the exit can be derived as follows:

$$E_{\mathrm{THz}}^{\mathrm{out}} = E_x(d)\sin\theta + E_y(d)\cos\theta$$
$$= E_{\mathrm{THz}}^{\mathrm{in}} e^{-\alpha_y d/2}[\cos^2\theta e^{i\omega(n_x-n_y)d/c} e^{-(\alpha_x-\alpha_y)d} + \sin^2\theta]. \tag{31}$$

This equation provides an analytical expression useful for realizing coherent control. Figures 34(b) and 34(c) show how the FID signal varies with θ. The on/off ratio of the FID amplitude reaches three and can be explained well by Eq. (31) by using realistic parameters for the refractive index and absorption coefficient.

Double-pulse coherent control experiments using ideas similar to the two examples above have been demonstrated with various types of excitations, including magnetic resonances[276], phonons[286–288], and charge excitations[289]. All these studies have helped establish a complete picture of wave-based logical gates that operate based on the linear superposition principle.

5.2 Magnon-Polaritons and Magnon Propagation

Another key subject of research in magnonics is the transport of information carried by magnons from one place to another[290]. This can be done through two methods. One is to first attempt converting the energy stored in magnons into photons, and then to propagate the photons to transfer the information. The method requires fabrication of a hybrid magnon–photon coupled device to form the so-called magnon-polaritons[291–294]. The second method is to utilize the intrinsic propagation effect of magnons themselves to transfer information. Therefore, this subsection aims to review magnon-polaritons and magnon propagation effects in $RFeO_3$. The reason for arranging these two topics together is that they are not fundamentally distinct effects from the level of physical principles. Some magnon-polariton devices do not offer confinement in all spatial dimensions, and therefore, allow polariton propagation along certain directions. Furthermore, for magnons propagating in a magnetic crystal, their magnetic dipoles are spontaneously coupled to a light field even in free space, which makes polaritonic effects appear. We will discuss below how polaritonic effects cross over to propagation effects as the spatial confinement is released step by step. These unique observations have been well established in $RFeO_3$ due to the high spatial and temporal coherence of magnon excitations afforded by the material system.

Sivarajah *et al.*[295] have realized magnon–phonon-polaritons in a $LiNbO_3 - ErFeO_3$ cavity. The device, depicted in Fig. 35(a), consists of a two-layer structure with a polished $ErFeO_3$ crystal stacked on top of a $LiNbO_3$ wafer. Through holes of a hexagonal lattice were drilled on the structure by femtosecond laser machining; three sites were intentionally left undrilled to create a defect in the photonic crystal, supporting a cavity mode. Through ISRS, a 3 eV pump laser beam directed into the cavity excited coherent phonon-polaritons in $LiNbO_3$, whose magnetic field component aligns parallel to the canted moment in the adjacent $ErFeO_3$ layer and therefore couples

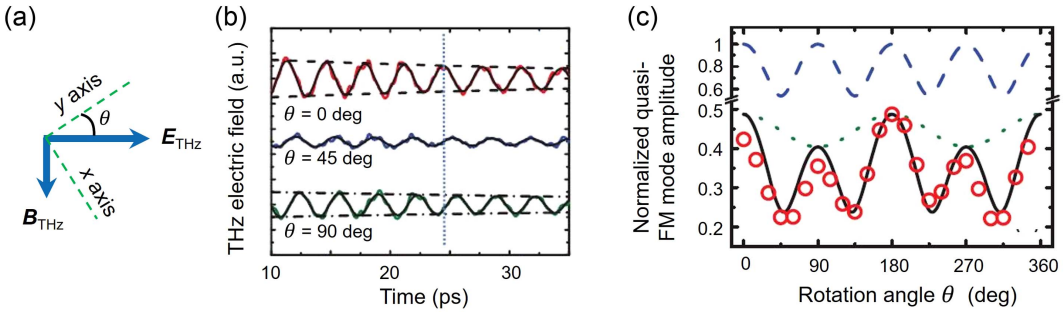

Fig. 34 Single-pulse coherent control of magnons in $YFeO_3$[285]. (a) Polarization configuration. (b) FID signal versus the polarization angle θ. (c) FID signal amplitude (derived from Fourier transform, shown in red circles) versus θ. Black solid line is model calculation using Eq. (31). Blue dashed and green dotted lines consider either the birefringence or the dichroism (but not both). Reproduced with permission from Ref. [285].

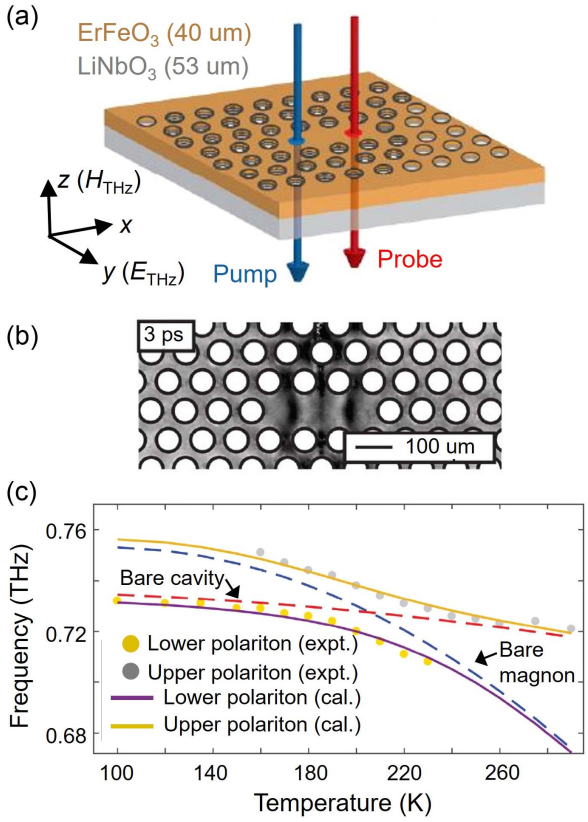

Fig. 35 Magnon–phonon-polaritons in a photonic crystal cavity[295]. (a) Experimental configuration. (b) Electro-optic sampling imaging of the cavity mode 3 ps after pump excitation. (c) Anticrossing branches of the magnon–phonon-polariton. Temperature is adjusted to detune the magnon and the phonon-polariton frequencies. Gray and yellow markers: data. Solid lines: polariton branches. Dashed lines: mode frequencies assuming no coupling. Reproduced with permission from Ref. [295].

to its quasi-FM magnon mode. The spatial and temporal profiles of the magnon–phonon-polariton were mapped out by electro-optic sampling microscopy [Fig. 35(b)]. Utilizing the different temperature dependences of the magnon mode in $ErFeO_3$ and the phonon-polariton mode in $LiNbO_3$, the authors performed a temperature scan to achieve resonance frequency detuning, as shown in Fig. 35(c). Around the temperature range where the magnon mode (red dashed) and the phonon-polariton mode (blue dashed) are supposed to intersect in frequency, two coupled modes appear with a frequency splitting of 16 GHz, suggesting the formation of strongly coupled magnon–phonon-polaritons.

Cavity magnon-polaritons based on $RFeO_3$ have also been demonstrated by Bialek *et al.*[296]. They performed normal-incidence THz transmission experiments on a polycrystalline $DyFeO_3$ disk sample. The front and back surfaces of the sample provided the cavity confinement and the Fabry–Pérot cavity modes. As shown in Fig. 36, the scan was performed in the high temperature range around the Fe^{3+} ordering temperature, where both quasi-FM and quasi-AFM modes soften significantly according to $f \propto (1 - T/T_N)^{\beta}$, with $\beta \sim 1/3$. The THz setup was a continuous-wave spectrometer based on frequency extensions to a vector network analyzer, and the measurement

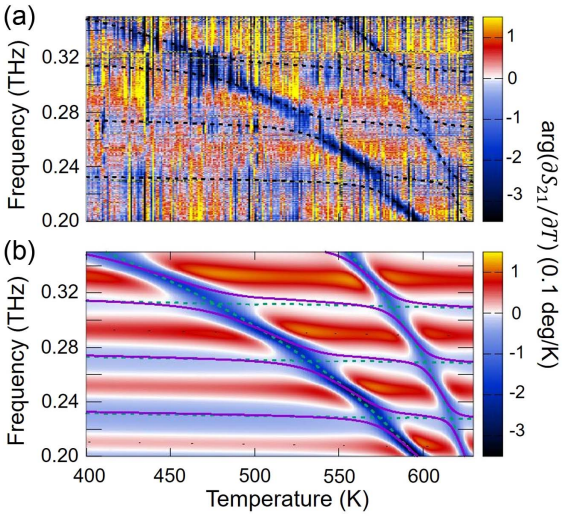

Fig. 36 Magnon-polaritons in a Fabry–Pérot cavity[296]. (a) Experimental phase shift of $\partial S_{21}/\partial T$. Dashed lines mark the polariton modes. (b) Model simulations. Dashed green lines: uncoupled modes. Modes with strong (weak) temperature dependence are magnon (cavity) modes. Purple solid lines: polariton modes. Reproduced with permission from Ref. [296].

quantity was the temperature-differential S parameter $\partial S_{21}/\partial T$. Both the experimental data [Fig. 36(a)] and numerical simulations of the phase of $\partial S_{21}/\partial T$ [Fig. 36(b)] show clear avoided crossing features in the eigenmodes of the sample; these are hallmarks of polariton modes formed by strong coupling between the magnons and the Fabry–Pérot cavity modes.

The two examples above both represent magnon-polaritons in fully confined cavities. However, magnon-polaritons can also exist in a structure that supports propagation, such as in a waveguide. This has also been demonstrated by Sivarajah *et al.*[295], in a $LiNbO_3$−$ErFeO_3$ device that had a layered structure similar to that shown in Fig. 35(a), only that all the air holes were removed to lift the spatial confinement in the slab plane; see Fig. 37(a). Such a waveguide device therefore allowed propagation (the wave vector can be continuously varied) within the sample plane, but still confined the field in the out-of-plane direction, due to the index mismatch of the slab with the surrounding environment. The pump was shaped into a line that, when directed onto the bare $LiNbO_3$ region, excited phonon-polaritons through ISRS. The phonon-polaritons then propagated into the $ErFeO_3$−$LiNbO_3$ region and coupled to the quasi-AFM magnons in $ErFeO_3$. A 2D Fourier transformation directly gave the dispersion relation of the polariton [Fig. 37(b)] when the authors used the probe to sample the polariton field spatially and temporally. The dispersion relation showed two prominent near-linear dispersive lines outside the light cone that were identified as the first two transverse-electric modes of the polariton waveguide. The signature of strong coupling to magnons was again found by zooming into the frequency window around the quasi-AFM frequency [red oval enclosed region in Fig. 37(b)] and observing the mode anticrossings [Fig. 37(c)]. The coupling strength of the magnon–phonon-polariton in this waveguide structure reached 20 GHz.

Having observed waveguide-based magnon-polaritons, one natural question that arises is whether polaritonic effects can still be seen within a simple setup where magnons propagate freely

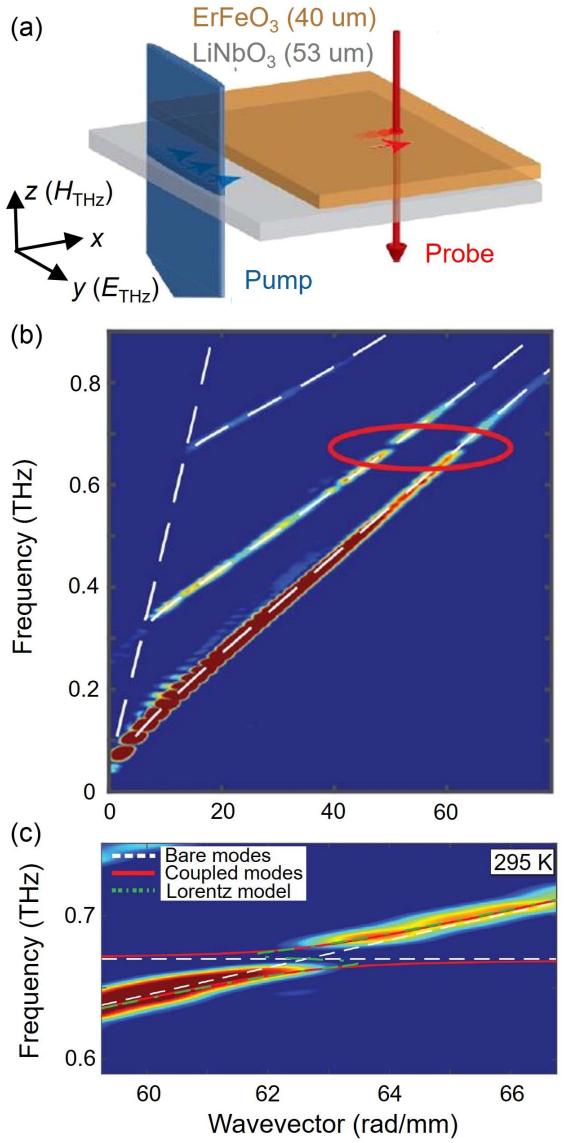

Fig. 37 Magnon–phonon-polaritons in a hybrid waveguide[295]. (a) Experimental configuration. (b) Dispersion relation of transverse-electric phonon-polariton modes. (c) Zoom-in view of the red-oval-enclosed region, where polariton branches form an anticrossing pattern. Reproduced with permission from Ref. [295].

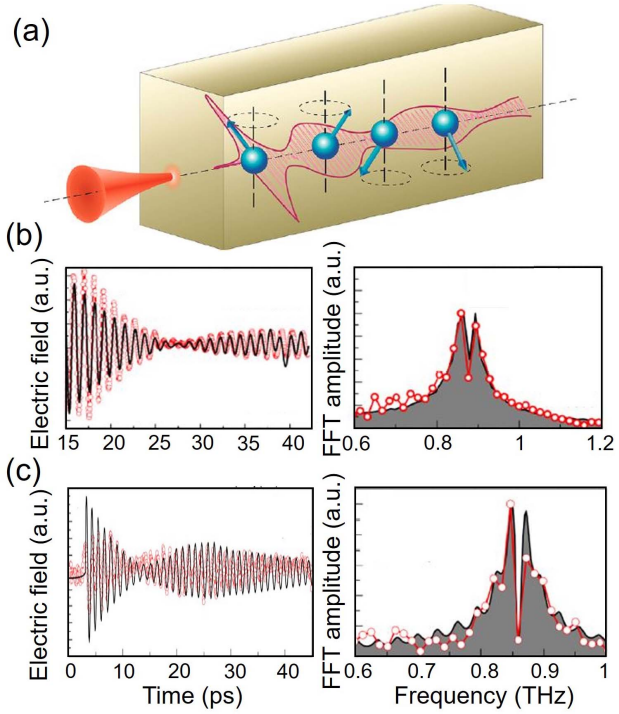

Fig. 38 Signatures of magnon-polaritons in free space[297]. (a) As optically excited magnons propagate in a $TmFeO_3$ crystal, they couple with a free-space light field and form polariton modes. (b) FID signal in transmission experiments (left) and its Fourier transform (right). (c) Emission fields in THz emission experiment (left) and its Fourier transform (right). Simulation results (black lines and gray shades) are overlaid on data (red hollow circles). Temperature: 40 K. Reproduced with permission from Ref. [297].

in a magnetic crystal, with all photonic confinements removed. Grishunin *et al.*[297] investigated this problem by performing THz transmission and emission experiments in a $TmFeO_3$ crystal [Fig. 38(a)]. By using an appropriate crystal cut and polarization configuration, they selectively excited the quasi-AFM magnon. Surprisingly, both the FID signal (in the transmission experiment) and the emitted THz field (in the emission experiment) developed beating patterns when the measurement time window became longer than 50 ps [Figs. 38(b) and 38(c)]. The time-domain beating suggests a frequency splitting of the quasi-AFM mode, which can be interpreted as the upper and lower branches of magnon-polaritons in the dispersion relation, where the light line is expected to intersect the magnon line; the interpretation is supported by a match between experiment and a classical electromagnetic simulation without any adjustable parameter [Figs. 38(b) and 38(c)]. Interestingly, the polariton branches could be observed only for crystals that are thick enough, indicating that it arises from a delicate energy exchange process between magnons and photons as magnons are propagating through the crystal. It sets the requirement that both a long interaction length and a long interaction time between magnons and photons are needed for polaritonic effects to stand out in free-space magnonic devices. A similar observation has also been made recently by Baydin *et al.*[298].

One may notice that the magnon propagation effect Grishunin *et al.*[297] pointed out is exclusively associated with the phase velocity. The group velocity is assumed to be near zero because optically excited magnons are expected to have very small momenta. This statement holds true for most systems employed so far where coherent magnons are launched through optical methods. A true demonstration of the transport of an optically excited magnon wave packet at a high group velocity therefore would be of high scientific value. This task has recently been achieved by Hortensius *et al.*[299] using a $DyFeO_3$ crystal.

As shown in Fig. 39(a), the key idea of Hortensius *et al.*[299] that enabled launching high-k (k: wave vector) magnons optically was to tune the pump photon energy up to the strongly absorbing charge-transfer peak for which the penetration depth is very small (~50 nm). This resulted in confining the pump excitation (including pump-excited magnons) within a very thin layer of the sample, promoting the upper limit of the wave vector that becomes accessible. The way the authors discerned the

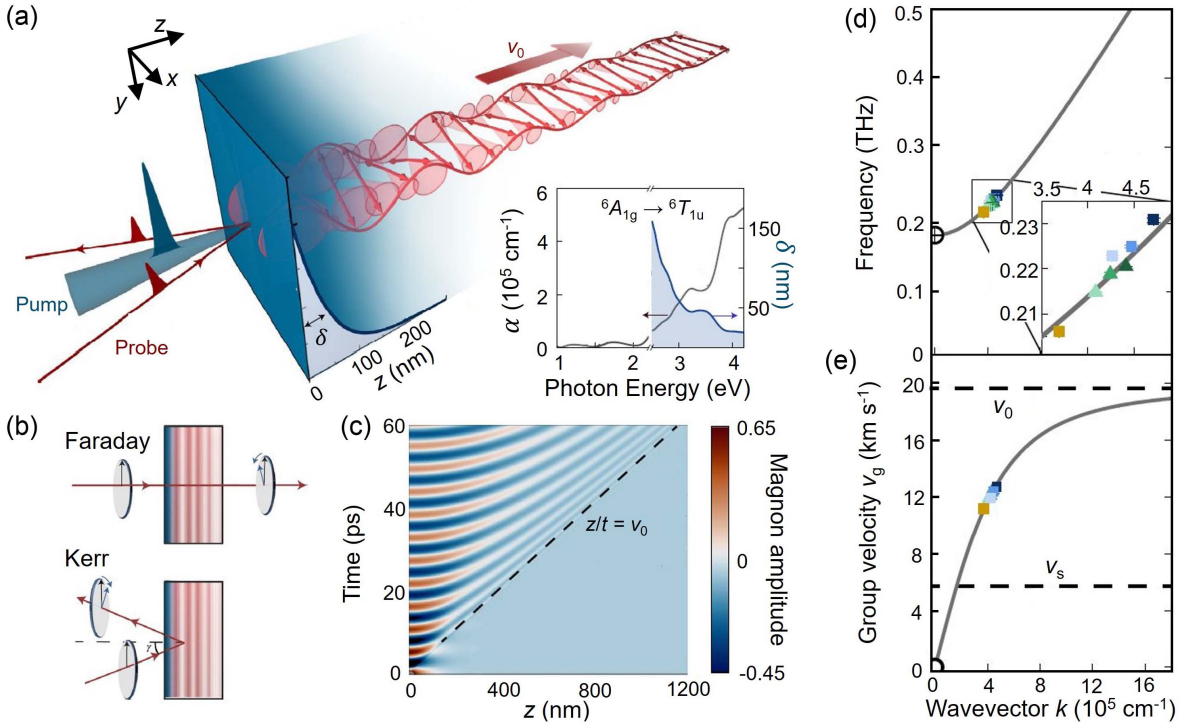

Fig. 39 Demonstration of magnon propagation at a supersonic group velocity[299]. (a) High-k magnons can be excited if pump excitation is confined in a very small penetration depth. Inset: penetration depth and absorption coefficient versus photon energy. (b) Within the Faraday and Kerr measurement geometries, the Kerr geometry is sensitive to high-k modes. (c) Simulated chirping of the magnon wave packet. (d) Reconstruction of the magnon dispersion relation by probe-wavelength-dependent measurements using the Kerr geometry. (e) Group velocity plot obtained from the dispersion. Colored markers: experimental data. Black dashed lines: sound velocity v_s and limiting group velocity v_0. Reproduced with permission from Ref. [299].

high-k magnons was through the peculiar observation that the quasi-AFM magnon frequency measured by time-resolved Kerr rotation was consistently higher than that obtained from time-resolved Faraday rotation [Fig. 39(b)]. This result was interpreted by considering the magnon dispersion

$$\omega_k = \sqrt{\omega_0^2 + (v_0 k)^2}, \tag{32}$$

where ω_k (ω_0) is the magnon frequency at finite k (zone center) probed in Kerr (Faraday) geometry, and $v_0 \approx 20$ km/s is the limiting group velocity. What makes Kerr geometry sensitive to finite-k modes is the Bragg condition that relates the probe wavelength λ_0 with the bright wave vector k_m through

$$k_m = 2k_0 n(\lambda_0) \cos\gamma, \tag{33}$$

where $k_0 \cos\gamma$ is the surface-normal component of the wave vector of the probe beam, and $n(\lambda_0)$ is the index of refraction at λ_0. This means that, although the initial magnon excitation contains a broad spectrum of k [see Fig. 39(c) for how the wave packet gets quickly chirped as time elapses], for a given λ_0, only one k_m component is detected (and therefore "bright"), giving $\omega_{k_m} = \sqrt{\omega_0^2 + (v_0 k_m)^2}$. The authors performed a series of probe-wavelength- and angle-dependent measurements on the magnon frequency to map out the dispersion within a certain range of k [Fig. 39(d)], and the slope of the dispersion around these data points determined the group velocity defined as

$$v_g = (\partial\omega_k/\partial k)|_{k=k_m}. \tag{34}$$

Figure 39(e) shows v_g versus k, and quantitatively gives the supersonic v_g that is achieved by the high-k magnon modes observed in this experiment.

The rapidly developing research on magnon-polaritons and magnon propagation effects in $RFeO_3$ is expected to open a new avenue for versatile design and control of future magnonic devices that operate in the THz frequency range.

5.3 Heterostructuring and Exchange-Biased Interfaces

A useful strategy in constructing functional spintronic devices is to place two magnetic materials in proximity, typically by depositing two layers of films together to form a heterostructure[300–303]. The exchange coupling between spins at the interface changes the spin states in both layers, and therefore, provides a tuning knob for magnetic control. The most common usage of AFM materials in magnetic heterostructures is to form an exchange bias device[304]. In a heterostructure where an AFM layer is adjacent to a soft FM layer, the exchange coupling causes a shift in the magnetic hysteresis loop of the FM layer. Since the AFM state cannot be easily perturbed by external magnetic

fields, once the AFM spin state is set, the direction and magnitude of the loop shift will be determined, causing a robust pinning of the FM layer magnetization at zero magnetic field. In this subsection, we review efforts to study FM/$RFeO_3$ heterostructures and the unique properties they provide for magnonic applications and SRT control.

Tang *et al.*[305] have discovered unusually efficient magnon excitation by optical pulses in a Fe/$RFeO_3$ (R = Er or Dy) heterostructure. One of their sample structures consisted of a 3.5-nm-thick FM Fe film deposited on top of a polished *x*-cut crystal of $ErFeO_3$, and another 2-nm-thick nonmagnetic Cu layer coated on Fe as the protective layer. Static characterization of the soft Fe film using the longitudinal magneto-optical Kerr effect (MOKE) revealed a clear exchange bias effect; see the shift of the hysteresis loop in Fig. 40(a) from zero under a weak magnetic field applied along the *z* axis of the $ErFeO_3$ crystal. Figure 40(b) shows results of time-resolved MOKE measurements on the same sample at room temperature ($ErFeO_3$ in Γ_4 phase). Oscillations are observed, whose amplitudes are considerably larger than that from a bare $ErFeO_3$ substrate (without the Fe film coating) under the same experimental conditions. Through a Fourier-domain analysis, they found that the oscillations arise from a superposition of multiple mode excitations including the quasi-FM magnon mode, an impurity mode, and a low-frequency coherent phonon mode; measurements on a heterostructure fabricated on a *z*-cut crystal demonstrated efficient excitation of the quasi-AFM mode as well (quasi-AFM observable only in *z*-cut samples due to a selection rule). The extraordinarily efficient magnon excitation in Fe/$RFeO_3$ heterostructures opens up opportunities in magnonic applications. Its microscopic mechanism should be distinct from ultrafast laser-induced heating, because otherwise it would be expected only around and slightly below the SRT temperature (Subsection 4.1). In the mechanism that the authors proposed [Fig. 40(c)], interfacial AFM exchange interactions cant the macroscopic moments of $RFeO_3$ out of the sample plane. Pump excitation quenches the interfacial exchange transiently, making the moments experience a restoring force back to the in-plane *z* axis, which is the orientation expected for a bare $RFeO_3$ substrate without the Fe capping layer. This mechanism enables launching magnon modes efficiently across the entire temperature range.

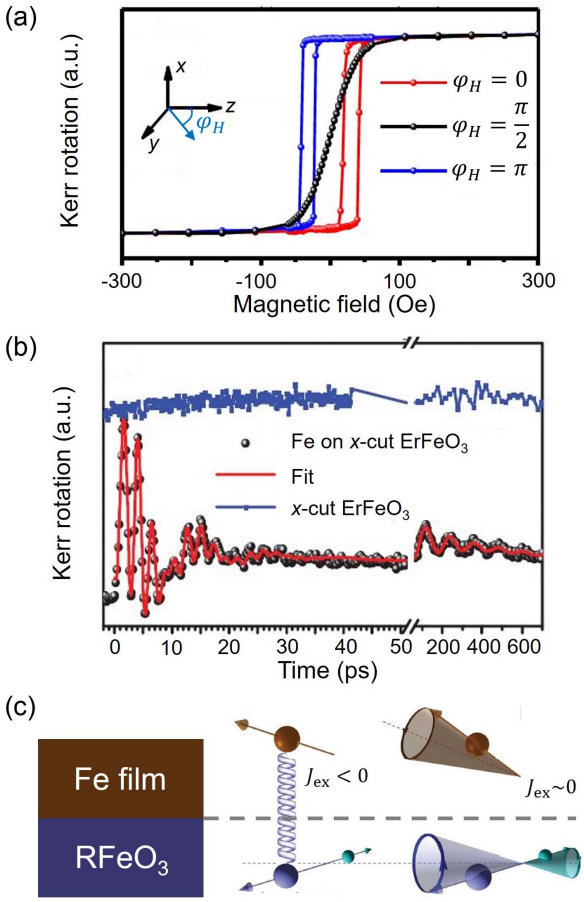

Fig. 40 Efficient magnon excitation in Fe/$RFeO_3$ heterostructure[305]. (a) Magnetic hysteresis loops of the Fe/$ErFeO_3$(100) sample for various field orientations. Fields never exceed the coercive field of $RFeO_3$. (b) Time-resolved MOKE transients for Fe/$ErFeO_3$(100) and the bare $ErFeO_3$(100) substrate under comparable pump fluences. (c) Proposed microscopic mechanism that explains efficient magnon excitation across a wide temperature range. Spins are canted initially due to interfacial exchange (left). Quenching of exchange by optical pulses leads to a restoring force and thereby launches magnons (right). Reproduced with permission from Ref. [305].

Joly *et al.*[306] have explored the possibility of triggering an SRT in the FM layer through coupling to the SRT in $RFeO_3$ in a FM/$RFeO_3$ heterostructure. As shown in Fig. 41(a), the sample consisted of a *y*-cut $SmFeO_3$, on top of which an FM 2-nm-thick Co film and a 1-nm-thick Pt protective layer were deposited. $SmFeO_3$ undergoes a $\Gamma_4 \rightarrow \Gamma_2$ SRT between 460 K and 470 K, so a 90 deg in-plane spin rotation is expected for a *y*-cut crystal. A circularly polarized X-ray beam, whose energy is resonant with the Co L_3-edge, impinged on the sample with grazing incidence (16 deg). X-ray magnetic circular dichroism (XMCD) directly reveals spin alignment in the Co film, with XMCD being finite only when spins have finite projections to the propagation direction of the X-ray beam. Figure 41(b) shows a set of temperature-dependent XMCD images taken in two incident geometries. When the X-ray propagates parallel to the *x* axis (*z* axis), the image shows high (low) contrast at 300 K but low (high) contrast at 485 K. Since a high image contrast indicates the coexistence of strong XMCD signals with opposite signs, it directly proves that (1) spins are along the current X-ray propagation direction, and (2) magnetic domains are formed in the Co film. Figure 41(b) therefore shows an SRT with spins parallel to the *x* axis at 300 K and to the *z* axis at 485 K in the Co film. This coincides with the SRT in $SmFeO_3$, and therefore, provides the proof for spin interlocking at the interface.

Using the XMCD image contrast as an indicator of spin orientation of the Co film, Joly *et al.*[306] also attempted to induce a correlated SRT through laser-induced heating. Figure 41(c) shows maps analogous to Fig. 41(b), and only the heating source is a ps laser beam; the temperature was set to 425 K, which is slightly below the SRT temperature in $SmFeO_3$. An SRT in the Co film that occurs in tandem with the SRT in $SmFeO_3$ upon static laser heating is again observed. Furthermore, Le Guyader *et al.*[307] later extended this work to the dynamical realm by providing time resolution to the experiment. They adjusted the sample temperature to be initially within the SRT range, used an optical pulse to provide transient heating, and collected the XMCD images by a time-delayed X-ray pulse.

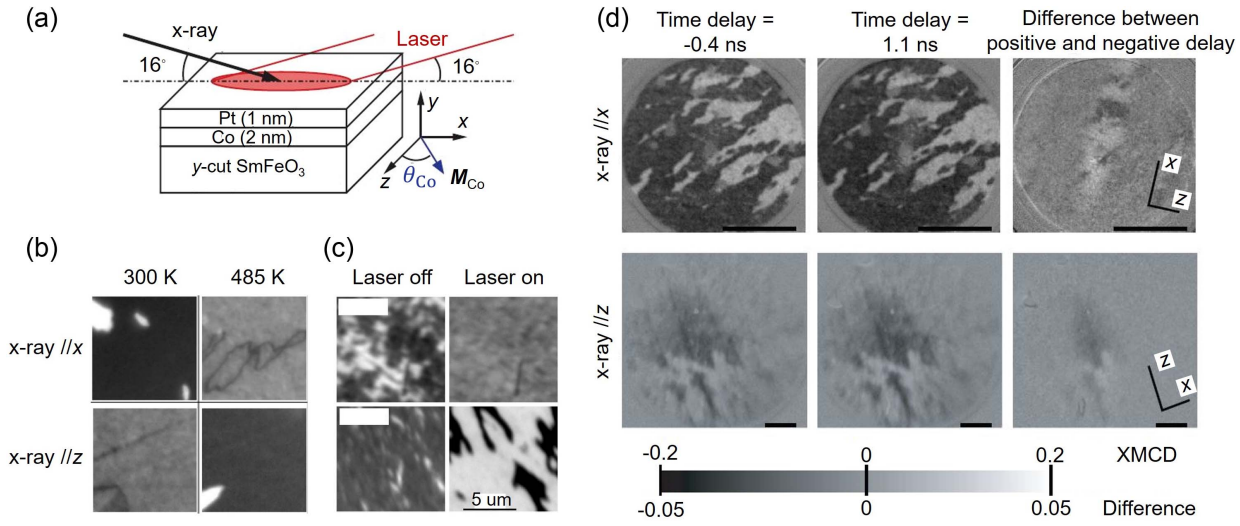

Fig. 41 Correlated SRT in $Co/SmFeO_3$ heterostructure[306,307]. (a) Experimental configuration. (b) Heating-induced SRT in the Co film probed by XMCD imaging. (c) Analogous maps to (b) except that heating is supplied by a laser beam. (d) Time-resolved XMCD images before and after a pulsed optical pump, and the pump-induced change obtained by a subtraction. Reproduced with permission from Refs. [306,307].

Figure 41(d) shows images before and after time zero, and their subtractions, for the two incident geometries. The subtraction highlights the pump-induced change, and one can tell that pumping causes a decrease (increase) in the image contrast for an X-ray propagating along the x axis (z axis). Although the change is small, it reflects a spin rotation by a few degrees from the x axis to the z axis caused by the optical pump. The rotation builds up within sub-100 ps, and a more accurate measurement of the rotation time is needed with a better instrumental resolution. Investigating an SRT in an FM film exchange-locked to an AFM material provides opportunities to interrogate the ultimate speed limit of spin switching in FM materials. The experiments carried out by this series of work here are expected to reveal much insight towards this goal.

5.4 Nonlinear Magnonics

In this subsection, we examine novel phenomena that arise when the spin oscillation amplitude becomes so large that the assumption of a harmonic magnetic potential is no longer valid. In these cases, anharmonicity sets in, and in the second quantization formulism, it is equivalent to considering the magnon–magnon scattering as the number of magnons increases[308]. On the application side, nonlinear magnonics is crucial because it enables the control of a magnon wave by another magnon wave, which is the fundamental working principle to construct all-magnon data processing units such as magnon transistors[309]. In addition, nonlinearity during magnon propagation also facilitates the generation of magnon solitons and bullets[310,311], opening up the possibility of long-distance magnon-based data transfer without distortion[7].

In the past, exciting large-amplitude THz-frequency magnons in AFM materials such as $RFeO_3$ was challenging. However, the recent advances of various types of techniques for generating intense THz radiation have opened up new possibilities to perform an in-depth study of the subject; see Subsection 2.2.2. We provide two examples below that demonstrate nonlinear magnonics in $RFeO_3$.

One type of anharmonic potential is a potential with two local minima separated by a shallow barrier. Assuming that the equilibrated system is initially in a valley, increasing the magnon oscillation amplitude will lead to further and further excursions of the system from the local minimum, until the spins gain large enough energy to overcome the barrier and switch to the other valley. This suggests transitioning of the magnetic configuration to a metastable state, a phenomenon in which both the spin switching effect and nonlinear magnonics manifest.

Schlauderer *et al.*[312] have demonstrated all-coherent spin switching in a double-well potential system in $TmFeO_3$, providing evidence for extreme nonlinearity of magnons. Being aware that the magnetic field component of THz pulses is too weak to excite large-amplitude magnons, the authors adopted the scheme discovered by Baierl *et al.*[244] (reviewed in Subsection 4.4), where THz-field driving of the electric-dipole-active CFTs of Tm^{3+} supplies an anisotropy torque to Fe^{3+} spins to generate large-amplitude quasi-FM magnons. A gold bowtie antenna was fabricated on the crystal to provide further electric field enhancement within the feed gap [Fig. 42(a)]. The crystal was set at a temperature in the middle of the SRT (within the Γ_{24} phase), where the equilibrium spin orientation should be such that the AFM vector is at an intermediate angle between the x axis and z axis [Fig. 42(b)]. There are four energy-equivalent domain types consistent with the configuration, but two were selected to be more favorable energetically as a magnetic field was applied, forming the two local minima of the desired double-well potential. With the angle between the AFM vector and the x axis denoted by ϕ, the two minima are expected to be centered at ϕ_0 with $-\pi/2 < \phi_0 < 0$, and ϕ_1 with $0 < \phi_1 < \pi/2$ [Fig. 42(c)].

As Schlauderer *et al.*[312] increased the THz pump-field strength and probed the magnon dynamics within the feed

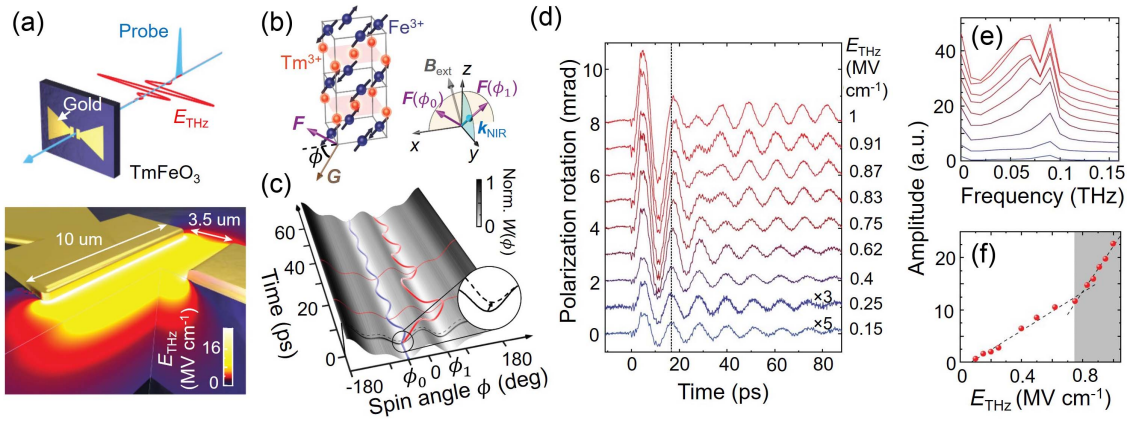

Fig. 42 Nonlinearity of magnons as evidence for all-coherent spin switching[312]. (a) Experimental configuration. (b) Spin orientations in the Γ_{24} phase and the two potential energy minima centered at ϕ_0 and ϕ_1. (c) Spin trajectories with (red curve) and without (blue curve) spin switching. Inset: modification to the potential due to an impulsive THz drive. (d) Fluence dependence of Faraday rotation transients. Dashed line highlights the phase shift. (e) Fourier transform of signals in (d). (f) Fluence dependence of the long-lived offset signal. Gray area marks the fluence range higher than the switching threshold. Reproduced with permission from Ref. [312].

gap using time-resolved Faraday rotation measurements, they observed a beating pattern developing on the oscillation signal, accompanied by a phase flip [Fig. 42(d)]. Fourier transform of the oscillations revealed an asymmetric splitting of the quasi-FM magnon mode, proving the existence of magnon nonlinearity. At the onset of peak splitting, the Faraday rotation signal also gained a long-lived offset, suggesting spin switching to a new metastable state. All these observations, being consistent with a microscopic model, are signatures of spin switching from ϕ_0 to ϕ_1 as the quasi-FM magnon amplitude surpasses a threshold at which the excursion of the system from equilibrium is large enough to overcome the barrier. They also engineered the height of the potential barrier through temperature or magnetic field tuning and observed behaviors consistent with the interpretation. Their demonstration of ballistic switching provides a scalable approach to switching magnetic bits with the least amount of energy dissipation.

For systems that appear distant from a phase transition (and therefore the double-well model does not apply), magnon nonlinearity can also set in when spins sample a large enough phase space on the Bloch sphere during magnon oscillations. Two-dimensional (2D) coherent spectroscopy, which is a technique frequently used on bio-chemical molecular systems to analyze lattice anharmonicity and vibronic couplings, is an ideal tool to be applied here for studying spin anharmonicity. The difference, however, is that this method needs to operate in the THz frequency range, which is much less common than 2D IR spectroscopy performed in the mid-IR range.

Lu *et al.*[313] have used 2D THz coherent spectroscopy to reveal magnon nonlinearity in $YFeO_3$. As shown in Fig. 43(a), the experiment was carried out by directing two intense THz pulses, labeled A and B, onto a $YFeO_3$ crystal and measuring the transmitted fields. If we denote the interpulse time delay by τ, and the measurement time delay after the second pulse (pulse B) by t, the 2D time-domain nonlinear signal field $B_{NL}(t,\tau)$ is written as

$$B_{NL}(t,\tau) = B_{AB}(t,\tau) - B_A(t,\tau) - B_B(t,\tau), \quad (35)$$

where $B_{AB}(t,\tau)$ is the total field in the presence of both pulses, and $B_A(t,\tau)$ [$B_B(t,\tau)$] is the field with the pulse A (B) only. The subtraction in Eq. (35) therefore cancels all signals of linear order and those that do not depend simultaneously on both pulses [Fig. 43(b)]. A 2D Fourier transform of $B_{AB}(t,\tau)$ gives $B_{AB}(f,\nu)$, which is the standard 2D spectrum as a function of excitation frequency ν and detection frequency f. The magnitude spectra of $B_{AB}(f,\nu)$ for measurements focusing on quasi-AFM and quasi-FM frequency ranges are shown in Figs. 43(c) and 43(d), respectively.

A total of six types of peaks are resolved[313], which can be ascribed to distinct nonlinear processes. The rephasing (R), nonrephasing (NR), pump–probe (PP), and two-quantum (2Q) peaks all arise from $\chi^{(3)}$ processes. A general 2D spectroscopy experiment probing $\chi^{(3)}$ processes requires three pump pulses. Since only two are used in this experiment, one needs to view one of the pulses here as the superposition of two (each with partial amplitude, and zero delay) to complete the analysis of the various possibilities of three-pulse interaction. In addition, $\chi^{(2)}$ processes that can be ascribed to second-harmonic generation (SHG) and THz rectification (TR) are also observed. All these nonlinear processes are graphically presented in terms of double-sided Feynman diagrams in Fig. 43(e), and we will not describe each of them at length here since the diagrams contain all the essential information about the field–spin interaction sequence, and standard textbooks provide procedures to interpret them[314].

Being able to resolve six types of nonlinear field–spin interactions is the unique capability afforded by 2D THz spectroscopy[315–321], and multidimensional spectroscopy is sometimes viewed as "the ultimate ultrafast spectroscopy experiment." As more intense THz sources and more elegant ways to manipulate THz beams are being developed, this general technique is expected to see further development[322]. The traditional power of 2D spectroscopy in revealing anharmonic potentials and anharmonic couplings between resonances is broadly useful for a large array of exotic quantum magnets[323,324] to provide valuable insight into the fundamental physics of magnetism.

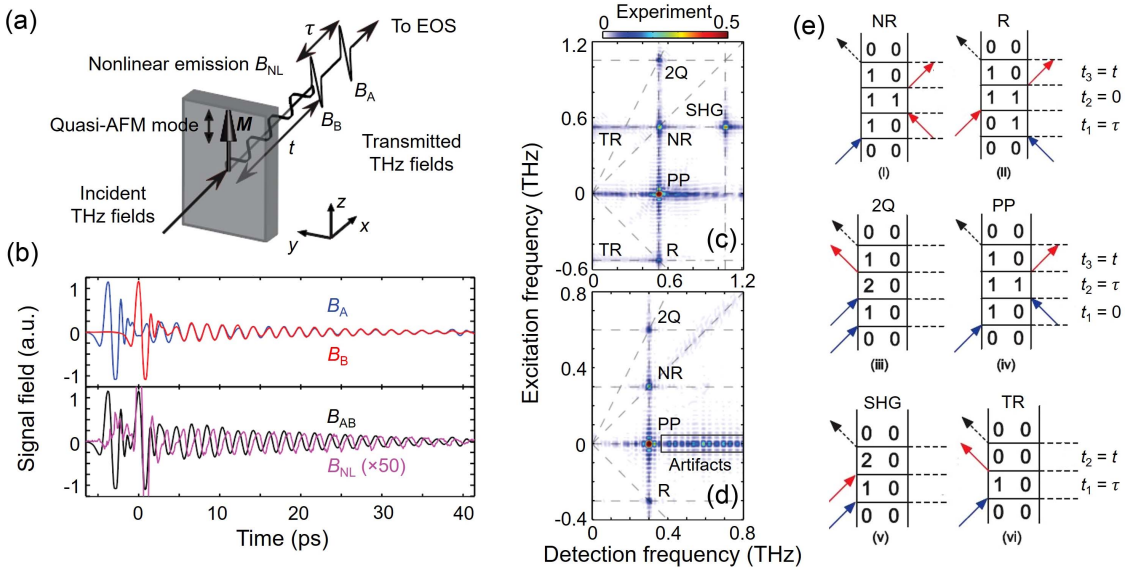

Fig. 43 2D coherent THz spectroscopy[313]. (a) Experimental configuration. (b) Various signal fields with either a single pulse or double pulses. The nonlinear signal $B_{NL}(t,\tau)$ is obtained by a subtraction process achieved in the experiment by a differential chopping detection method. (c), (d) 2D magnitude spectra of $B_{AB}(f,\nu)$ for measurements focusing on the quasi-AFM and quasi-FM frequency ranges. (e) Double-sided Feynman diagrams showing the excitation pathways of various nonlinear processes marked in (c) and (d). Blue and red arrows represent interactions with pulses A and B, respectively. Black dashed arrow represents the measured emission field. Reproduced with permission from Ref. [313].

6 Ultrastrong Cooperative Magnetic Coupling and the Dicke Phase Transition

In Subsection 5.2, we discussed a few experimental attempts to observe and analyze magnon-polaritons based on $RFeO_3$ systems. These are hybrid excitations formed by the strong coupling of THz magnons in $RFeO_3$ crystals with photons from the surrounding environment (cavity/waveguide/free space). When describing the light–matter coupling as being "strong," we referred to the criterion that the frequency splitting of the polariton modes is large enough to be resolved from the polariton linewidths[73,325], so that at least one full cycle of light–matter energy exchange that arises from Rabi flopping can stand out from damping.

In this section, we focus on another series of THz-frequency phenomena in $RFeO_3$ systems that are again closely related to both magnetism and light–matter coupling. There are two important aspects, however, that distinguish these phenomena from those in Subsection 5.2, and make them extraordinary. The first is that they reside in the USC regime of light–matter interaction[73,74]. This is a regime where the coupling strength needs to not only overcome the decay rate but also become a sizable fraction of the natural frequencies of the uncoupled light and matter[326–332]. The quantitative argument translates to the fact that light and matter mix to an extreme degree, and unusual phenomena that are crucial for quantum applications are expected to arise[333–336]. Second, although the phenomena we are about to discuss reveal unprecedented information on light–matter coupled systems, they do not really require a standard polaritonic setup, in which a carefully designed photonic cavity should be fabricated to enclose a crystal supporting matter excitations. Instead, they are matter–matter coupled systems that are capable of simulating light–matter coupled Hamiltonians. The role cavity photons play in a standard polaritonic system is taken by a collective bosonic matter excitation, which ultrastrongly couples with another matter excitation in the same material. These condensed-matter quantum simulators provide opportunities to reveal novel phenomena that are predicted for light–matter coupling Hamiltonians but have so far remained difficult to access.

To illustrate why $RFeO_3$ can be such quantum simulators of light–matter coupling Hamiltonians in the USC regime, and what exact problems they address, we arrange our presentation below according to a designed sequence. We will first provide an introduction to the fundamentals of light–matter coupling models, and then describe the predictions related to the Dicke SRPT in the USC regime. A discussion will then follow addressing why a Dicke SRPT in equilibrium is difficult to achieve in genuine quantum-optical systems, and how $Er^{3+}-Fe^{3+}$ interactions in $ErFeO_3$ are an ideal platform to simulate a magnonic SRPT in equilibrium. Finally, we will show that even an $RFeO_3$ system without $R^{3+}-Fe^{3+}$ magnetic coupling, such as $YFeO_3$, can simulate the anisotropic Hopfield model by forcing quasi-FM and quasi-AFM modes to couple through a properly oriented external magnetic field. The unusual aspects associated with the counter-rotating term within the simulated Hamiltonian cause large-amplitude ground-state squeezing, which is expected to be useful in decoherence-free quantum applications.

6.1 Ultrastrong Light–Matter Coupling

To describe the unusual physical phenomena in the USC regime of light–matter interaction, we first introduce the model that describes N identical two-level atoms (with ground state $|g\rangle$ and

excited state $|e\rangle$) interacting with a single-mode light field in a photonic cavity[337] [Figs. 44(a) and 44(b)]. The first-quantized Hamiltonian that describes the atomic ensemble reads $H_{\rm at} = \sum_{j=1}^{N} \frac{\hat{\boldsymbol{p}}_j^2}{2m} + \hat{U}_j$, where $\hat{\boldsymbol{p}}_j$ is the electron momentum of the jth atom, m is the electron mass, and $\hat{U}_j$ is the potential energy. Coupling of the ensemble with the light field can be described by the Peierls substitution $\hat{\boldsymbol{p}}_j \to \hat{\boldsymbol{p}}_j - e\hat{\boldsymbol{A}}(\boldsymbol{r}_j)$, where $\hat{\boldsymbol{A}}(\boldsymbol{r}_j)$ is the vector potential at the atomic position $\boldsymbol{r}_j$. This gives

$$H_{\rm at} \to H_{\rm at} + H_{\rm int} + H_{A^2}. \tag{36}$$

The light–matter interaction term $H_{\rm int}$ and the A^2-term H_{A^2} read

$$\begin{aligned} H_{\rm int} &= -\sum_{j=1}^{N} \frac{e}{m} \boldsymbol{p}_j \cdot \boldsymbol{A}_0 (a^\dagger + a), \\ H_{A^2} &= \sum_{j=1}^{N} \frac{e^2}{2m} |\boldsymbol{A}_0|^2 (a^\dagger + a)^2, \end{aligned} \tag{37}$$

where $\boldsymbol{A}_0$ is the amplitude of $\hat{\boldsymbol{A}}(\boldsymbol{r}_j)$, and a ($a^\dagger$) is the photon annihilation (creation) operator. These two terms can be rewritten in the second-quantized form

$$\begin{aligned} H_{\rm int} &= -i\hbar\Omega_0 (a^\dagger + a) b^\dagger + \text{h.c.}, \\ H_{A^2} &= \hbar D (a^\dagger + a)^2, \end{aligned} \tag{38}$$

where the collective atomic excitation operator $b^\dagger$ is defined as

$$b^\dagger = \frac{1}{\sqrt{N}} \sum_{j=1}^{N} (|e\rangle\langle g|)_j, \tag{39}$$

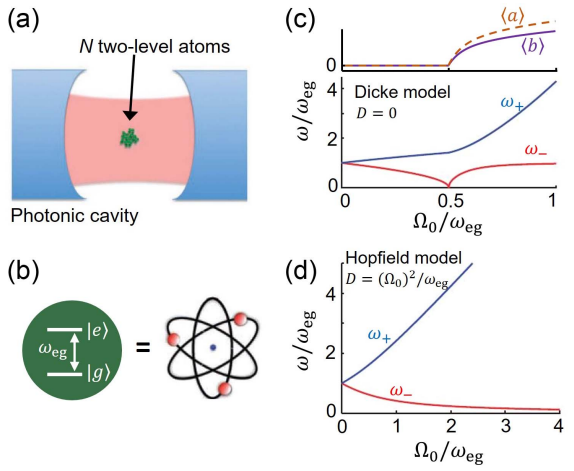

Fig. 44 Light–matter interaction setup for studying the Dicke phase transition in the USC regime[337]. (a) N atoms in a photonic cavity. (b) Diagram of an individual atom. (c) Static cavity and matter fields (upper)[338] and polariton frequencies versus coupling strength (lower) calculated from the Dicke model. (d) Same as the lower panel of (c), but for the Hopfield model (full Hamiltonian retaining the A^2-term). Reproduced with permission from Ref. [337].

the Rabi frequency as an indicator of the light–matter coupling strength is

$$\Omega_0 = \frac{\omega_{\rm eg}}{\hbar} \boldsymbol{d}_{\rm eg} \cdot \boldsymbol{A}_0 \sqrt{N}, \tag{40}$$

and the coefficient for the A^2-term is

$$D = (\Omega_0)^2/\omega_{\rm eg}. \tag{41}$$

Here, $\omega_{\rm eg}$ ($\boldsymbol{d}_{\rm eg}$) represents the frequency difference (transition dipole) between the ground state and the excited state of the two-level atoms.

By writing the atomic Hamiltonian as $H_{\rm at} = \hbar\omega_{\rm eg} b^\dagger b$ and the photonic Hamiltonian as $H_{\rm cav} = \hbar\omega_{\rm cav} a^\dagger a$ ($\omega_{\rm cav}$ is the frequency of the photonic mode), and using the expressions in Eq. (38), we obtain the total Hamiltonian as the sum

$$H = H_{\rm cav} + H_{\rm at} + H_{\rm int} + H_{A^2}. \tag{42}$$

There are a few important aspects about this Hamiltonian. The first is the appearance of terms proportional to $(ab^\dagger - a^\dagger b)$ and $(a^\dagger b^\dagger - ab)$ in the interaction Hamiltonian $H_{\rm int}$; the former are known as co-rotating terms and the latter as counter-rotating terms. Co-rotating terms correspond to resonant absorption ($ab^\dagger$) and emission ($a^\dagger b$) processes, while counter-rotating terms either create ($a^\dagger b^\dagger$) or annihilate (ab) two excitations simultaneously, and therefore, correspond to nonresonant processes that do not conserve the excitation number. Second, when the light–matter coupling strength is much smaller than the energy spacing of the TLSs ($\Omega_0/\omega_{\rm eg} \ll 1$), it is legitimate to neglect the counter-rotating terms in $H_{\rm int}$ [known as the rotating-wave approximation (RWA)] and the entire A^2-term H_{A^2} (since it appears higher order in terms of $\Omega_0/\omega_{\rm eg}$), making the remainder of the Hamiltonian fully diagonalizable. These approximations are not valid in the USC regime, in which Ω_0 becomes so large that $\Omega_0/\omega_{\rm eg} \sim 1$. Third, the $\Omega_0/\omega_{\rm eg} \sim 1$ criterion for the USC regime is usually considered to be demanding to realize experimentally, but the appearance of the $\sqrt{N}$ enhancement factor in Eq. (40) provides an opportunity to boost Ω_0 simply by increasing the number of atoms in the cavity. The $\sqrt{N}$ enhancement points to the collective nature of Ω_0, since it suggests that N atoms cooperatively contribute to the coupling so that the ensemble can be viewed as one giant combined oscillator whose dipole is $\sqrt{N}$ times stronger than individual dipoles[291,327,339]. This effect is reminiscent of the collective radiative decay of atoms predicted by Dicke's model of superradiance[340], and thus, is named Dicke cooperativity. Finally, based on Dicke cooperativity, a number of solid-state systems that host numerous numbers of oscillators (large $\sqrt{N}$) with huge dipole moments (large $\boldsymbol{d}_{\rm eg}$) have been used to reach the USC regime[292,327,339]; comprehensive reviews on this topic exist[73,74].

One can then proceed to analyze the total Hamiltonian in Eq. (42) to discover the unusual phenomena associated with the USC regime. In 1973, Hepp and Lieb[341] as well as Wang and Hioe[342] studied the thermodynamic properties of the Dicke model, using a simplified Hamiltonian adopting the RWA and dropping the A^2-term. They discovered a second-order phase transition at large enough Ω_0 and low enough temperature, across which a static photonic field and an atomic polarization appear simultaneously. This is a significant result known

as the Dicke SRPT. Despite its original prediction as a finite-temperature classical transition, the model was shown in the zero-temperature limit to host a quantum phase transition as one increases Ω_0; see the zero-temperature expectation values of photon and matter operators plotted versus Ω_0 in Fig. 44(c) and the order parameter onset at $\Omega_0/\omega_{eg} = 0.5$.

The SRPT can be understood as the outcome of critical mode softening. Starting from the total Hamiltonian in Eq. (42), eigenfrequencies of the model can be obtained by a Hopfield–Bogoliubov transformation[337] to convert the Hamiltonian into the diagonalized form

$$H = \hbar\sum_{i=\pm}\omega_i P_i^\dagger P_i + \text{Const.}, \tag{43}$$

where P_i are polaritonic operators ($i = \pm$, representing upper or lower polariton) given by

$$P_i = u_i^{\text{ph}} a + u_i^{\text{el}} b + v_i^{\text{ph}} a^\dagger + v_i^{\text{el}} b^\dagger, \tag{44}$$

satisfying the bosonic commutation relations $[P_+, P_+^\dagger] = [P_-, P_-^\dagger] = 1$ and $[P_+, P_-^\dagger] = [P_+, P_-] = 0$. The coefficient vectors $(u_i^{\text{ph}}, u_i^{\text{el}}, v_i^{\text{ph}}, v_i^{\text{el}})^T$ and the polaritonic frequencies ω_i are, respectively, the eigenvectors and eigenvalues of the matrix

$$M = \begin{pmatrix} \omega_{\text{cav}} + i2D & -i\Omega_0 & -2D & -i\Omega_0 \\ i\Omega_0 & \omega_{\text{eg}} & -i\Omega_0 & 0 \\ 2D & -i\Omega_0 & -(\omega_{\text{cav}} + i2D) & -i\Omega_0 \\ -i\Omega_0 & 0 & i\Omega_0 & -\omega_{\text{eg}} \end{pmatrix}. \tag{45}$$

Polariton frequencies calculated by using this method assuming $D = 0$ (neglecting the A^2-term) and $\omega_{\text{cav}} = \omega_{\text{eg}}$ (zero detuning) are shown in the lower panel of Fig. 44(c). As Ω_0 increases, the coupling makes the polariton branches move apart from each other. The energy gap is linear versus Ω_0 initially, but the softening of the lower polariton branch ω_- accelerates upon further increasing Ω_0, until it softens to zero frequency at $\Omega_0/\omega_{\text{eg}} = 0.5$; this is the exact point where a quantum phase transition into the SRPT is achieved.

However, the conspicuous flaw in the Hamiltonian assumed by the early proposal of the SRPT was the RWA and the neglect of the A^2-term, since they, as we have mentioned, are not simplifications that can be made when $\Omega_0/\omega_{\text{eg}} \sim 0.5$, even though such a large coupling strength is needed for the transition to occur. In particular, when the A^2-term H_{A^2} is included, calculations show that the lower polariton frequency would only approach but never reach zero [Fig. 44(d)], no matter how large it becomes. This means that the SRPT should be forbidden for the full model; the underlying reason can be traced back to the oscillator strength sum rule and the gauge invariance[343]. Later, the assumed conditions for proving the inaccessibility of an SRPT are clarified, which are reduced to the statement that an SRPT in thermal equilibrium can never be achieved for minimally coupled (Peierls substituted) systems under the dipole approximation[344]. This is known as the no-go theorem for the SRPT, which appears in the discussion of later works[345–347].

Because the unique ground state afforded by the SRPT is appealing, a question then arises asking whether it is possible to circumvent the no-go theorem. A variety of proposals have been put forward, aiming to breach at least one of the assumptions used to derive the theorem. A nonequilibrium scheme of laser-driven atoms to mimic the Dicke model (without the A^2-term) was proposed and later demonstrated experimentally[348,349]. Early proposals recommended inclusion of the spin DOF in the light–matter interaction[350]. A few studies have searched for certain superconducting circuit diagrams for which the oscillator strength sum rule does not apply[337,351]. More recent studies aim to harness spatially varying electric fields in multimode cavities to achieve light–matter coupling beyond the dipole approximation[345,352].

6.2 Magnonic Superradiant Phase Transition in $ErFeO_3$

Despite the large variety of proposals of carefully designed light–matter coupled systems aiming at invalidating the no-go theorem, an experimental demonstration of the SRPT in thermal equilibrium has remained elusive. This, on one hand, calls for more quantum-controllable experimental systems that allow easier detection of potential superradiant ground states[353–355], but on the other hand, suggests the necessity of a more overturning strategy that falls outside the scope of existing proposals.

Since the essence of the Dicke model is the coupling of an ensemble of TLSs with a boson field, the boson field being a photonic mode confined in a cavity, it would be interesting to think whether the model can be simulated by a near-equivalent quantum system where another collective boson field in matter, such as magnons, plays the role of photons, to couple to the TLSs. The advantage of such a mapping would be twofold. The first is that the matter boson field (that plays the role of photons) and the TLSs can both reside in one material system, and a photonic cavity is not required. This significantly improves the experimental accessibility for simultaneous probing of order parameters in both sectors across a potential SRPT. Second, when magnons are used to replace photons, one could use electron spins as TLSs, and the resulting spin–magnon coupling is ensured to neither be minimally coupled (since the charge DOF is not involved) nor be describable in any sense by the dipole approximation (since the dominant interaction is the exchange interaction). This implies that both of the necessary conditions for the no-go theorem are likely to be violated in a spin–magnon interaction system and therefore opens up a unique possibility to achieve an SRPT in thermal equilibrium.

$RFeO_3$ crystals are ideal spin–magnon interacting systems that can be used as the desired quantum simulator of the Dicke Hamiltonian. Taking $ErFeO_3$ as an example, the situation is depicted in Fig. 45. The quasi-FM magnon mode of Fe^{3+} plays the role of the cavity photonic mode in the Dicke model, while Er^{3+} ions have the appropriate energy-level structure be treated as TLSs. Within a low-symmetry crystal field, spin–orbit

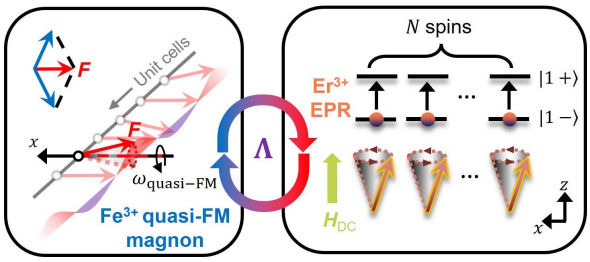

Fig. 45 Spin–magnon interaction in $ErFeO_3$[169]. Quasi-FM oscillations of Fe^{3+} are resonantly coupled with the EPR of N Er^{3+} spins at a rate of Λ. Reproduced with permission from Ref. [169].

coupled states of Er^{3+} ions ($4f^{11}$) split into Kramers doublets (Subsection 3.2). In the low-temperature limit, only the ground state doublet $|1-\rangle$ and $|1+\rangle$ would be relevant as thermal excitation cannot populate the higher doublets; these states mimic a two-level atom with $|g\rangle = |1-\rangle$ and $|e\rangle = |1+\rangle$. The transition between $|1-\rangle$ and $|1+\rangle$ is the electron paramagnetic resonance (EPR) of Er^{3+}, whose frequency is tunable by an external magnetic field. Because Fe^{3+} and Er^{3+} are known to be coupled by exchange interactions[80], Fe^{3+} magnons and Er^{3+} EPR will couple; the coupling strength, denoted by Λ here, is equivalent to Ω_0 in Eq. (38).

To ensure that the spin–magnon interaction in $ErFeO_3$ is a faithful simulator of the Dicke model, Li *et al.*[169] have performed an experiment to search for Dicke cooperativity, a key trait in the original Dicke Hamiltonian that enables a $\sqrt{N}$-fold scale-up of Ω_0. Figure 46(a) shows THz absorption spectra for a z-cut $ErFeO_3$ crystal at 45 K (Γ_2 phase) at various external magnetic fields ($H_{DC}\|z$). The constant-frequency line at 0.39 THz is assigned to be the Fe^{3+} quasi-FM, and the line that increases linearly with H_{DC} is the Er^{3+} EPR. At lower temperatures, anticrossings begin to develop around the zero-detuning magnetic fields where the Fe^{3+} magnon and Er^{3+} EPR are close in frequency [Fig. 46(b)]; the frequency splitting at zero detuning is quantitatively proportional to Λ, the spin–magnon coupling strength. With decreasing temperature, it is observed that anticrossings become more prominent, suggesting that Λ

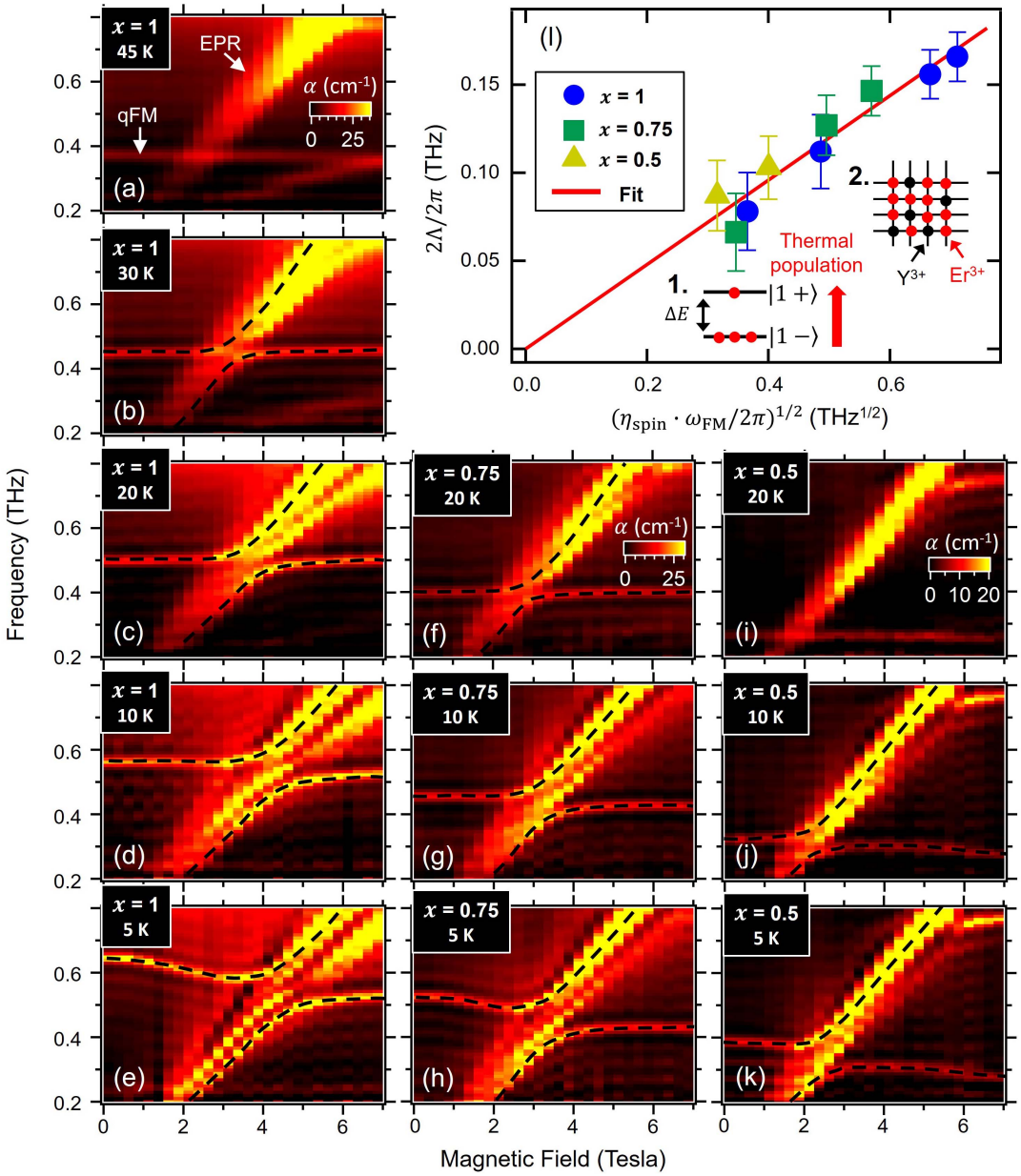

Fig. 46 Evidence for Dicke cooperativity in magnetic interactions[169]. (a)–(k) THz absorption spectra of $ErFeO_3$ crystal under a z-oriented external magnetic field at various temperatures and Y^{3+} doping levels. (l) The coupling rate shows proportionality with the square root of Er^{3+} density. Inset shows two types of mechanisms that tune the effective spin density of Er^{3+}. Reproduced with permission from Ref. [169].

increases [Figs. 46(b)–46(e)]. Furthermore, at a constant temperature, doping the crystal with nonmagnetic Y^{3+} ($Er_xY_{1-x}FeO_3$) is also able to tune Λ, with Λ decreasing as the Er^{3+} concentration x decreases [compare Fig. 46(c) with 46(f) and 46(i), 46(d) with 46(g) and 46(j), 46(e) with 46(h) and 46(k)].

Li *et al.*[169] interpreted the tunability of Λ both by temperature and by Y^{3+} doping as an indicator of Dicke cooperativity, because, as discussed below, both experimental control knobs are effectively tuning the Er^{3+} spin density n_{spin}. As shown in the inset of Fig. 46(l), temperature tuning changes the thermal distribution of Er^{3+} within its $|1-\rangle$ and $|1+\rangle$ states; the lower the temperature, the more spins populate the lower $|1-\rangle$ state, which effectively increases the number of excitable Er^{3+} spins according to $\tanh(-\Delta E/k_BT)$, where ΔE is the energy separation, and k_BT is the thermal energy. Second, in experiments using $Er_xY_{1-x}FeO_3$ (x being Er^{3+} concentration) crystals, nonmagnetic Y^{3+} doping simply reduces the Er^{3+} density through dilution without changing the crystal and magnetic structure of the sample. Putting these facts together, the Er^{3+} spin density that can contribute to spin–magnon coupling is subject to a correction factor $\eta_{\text{spin}} = x \cdot \tanh(-\Delta E/k_BT)$, which contains both temperature and doping information. Indeed, when one plots Λ versus $\sqrt{\eta_{\text{spin}}}$, the data points from all temperature- and doping-dependent measurements fall onto a single line that passes through the origin, evidencing the $\Omega_0 \propto \sqrt{N}$ relation of Dicke cooperativity; see Fig. 46(l), and note the additional $\sqrt{\omega_{\text{FM}}}$ factor, where ω_{FM} is the quasi-FM frequency that comes from the vacuum field amplitude of magnons.

The observation of Dicke cooperativity suggests that Er^{3+} spins as TLSs are cooperatively coupled with the Fe^{3+} magnons in $ErFeO_3$. Furthermore, the extracted Λ from Fig. 46(k) occupies a considerable fraction of the magnon/EPR resonance frequency, proving that spin–magnon coupling is in the USC regime. In addition, as discussed before, the model is known to violate a few key premises used to derive the no-go theorem. All of these add favorably to the necessary conditions to achieve an SRPT in thermal equilibrium.

What would an SRPT for a spin–magnon coupled system look like then? Spontaneous appearance of a static light field and an atomic polarization in the light–matter coupled superradiant ground state straightforwardly translates to spin ordering in a spin–magnon coupled system. And just like how ordering sets in both sectors that participate in the coupling in the Dicke model, an SRPT in $ErFeO_3$ would be a cooperative spin ordering involving both Er^{3+} and Fe^{3+} subsystems. Within the well-known temperature-dependent magnetic phase diagram of $ErFeO_3$ (Fig. 3), one indeed can identify a phase transition ($\Gamma_2 \to \Gamma_{12}$) at 4 K, known as the low-temperature phase transition (LTPT), across which Er^{3+} spins develop AFM order along the z axis, and the AFM vector of the Fe^{3+} spins rotates in the y–z plane; see Figs. 47(a) and 47(b).

Bamba *et al.*[356] have theoretically demonstrated that the LTPT in $ErFeO_3$ is in fact an SRPT for a spin–magnon coupled system. The term "magnonic SRPT" was given to the phenomenon to distinguish it from the standard light–matter coupled SRPT. A spin model Hamiltonian taking into account the Fe^{3+} subsystem, Er^{3+} subsystem, and $Fe^{3+} - Er^{3+}$ spin interactions was established:

$$H = H_{\text{Fe}} + H_{\text{Er}} + H_{\text{Fe-Er}}. \tag{46}$$

The Fe^{3+} Hamiltonian, written as

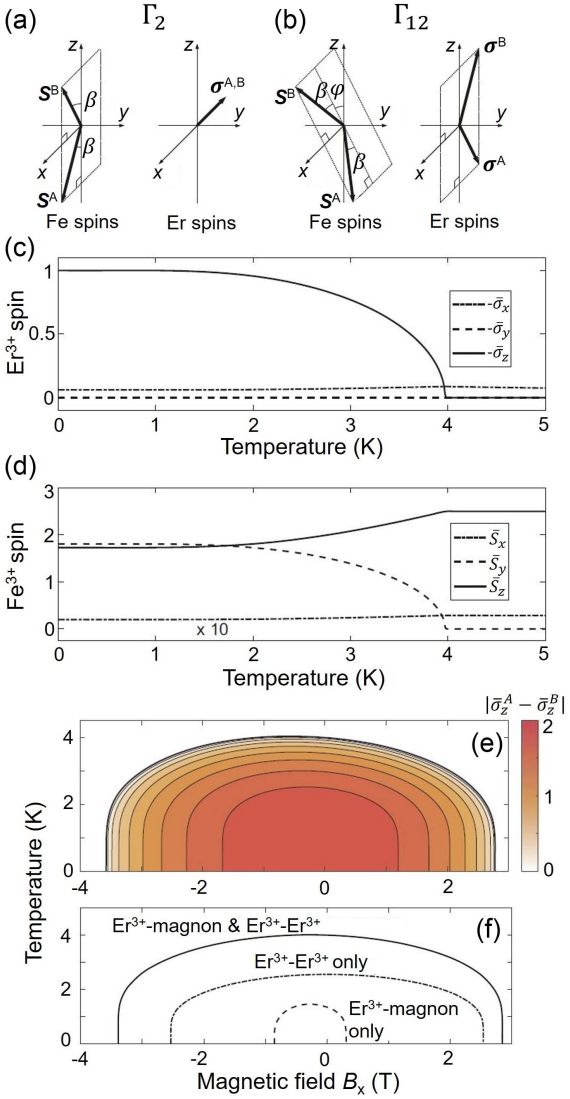

Fig. 47 Magnonic superradiant phase transition in $ErFeO_3$[356]. (a), (b) $\Gamma_2 \to \Gamma_{12}$ LTPT, across which Er^{3+} develops AFM order and Fe^{3+} spins rotate in the b–c plane. Averaged spin components of (c) Er^{3+} and (d) Fe^{3+} versus temperature calculated via the mean-field method. (e) Temperature–field phase diagram for $\boldsymbol{B}^{\text{DC}} \| x$, highlighting the phase boundary of LTPT, calculated by the mean-field method. (f) Phase boundaries calculated from the extended Dicke Hamiltonian, by selectively including certain terms in the Hamiltonian. Solid: both the Er^{3+}–magnon and $Er^{3+}-Er^{3+}$ interactions are included. Dashed-dotted: only the $Er^{3+}-Er^{3+}$ interaction is included. Dashed: only the Er^{3+}–magnon interaction is included. Reproduced with permission from Ref. [356].

$$H_{\text{Fe}} = \sum_{s=A,B}\sum_{i=1}^{N_0} \mu_B \hat{\boldsymbol{S}}_i^s \cdot g^{\text{Fe}} \cdot \boldsymbol{B}^{\text{DC}} + J_{\text{Fe}} \sum_{\text{n.n}} \hat{\boldsymbol{S}}_i^A \cdot \hat{\boldsymbol{S}}_{i'}^B - D_y^{\text{Fe}} \sum_{\text{n.n}} (\hat{S}_{i,z}^A \hat{S}_{i',x}^B - \hat{S}_{i',z}^B \hat{S}_{i,x}^A) - \sum_{s=A,B}\sum_{i=1}^{N_0} [A_x (\hat{S}_{i,x}^s)^2 + A_z (\hat{S}_{i,z}^s)^2 + A_{xz} \hat{S}_{i,x}^s \hat{S}_{i,z}^s], \tag{47}$$

includes (in the order given in the equation) the field–spin Zeeman interaction, the isotropic exchange interaction summed over the nearest neighbors (n.n), the antisymmetric DM interaction summed over the n.n, and the single-ion anisotropy. The treatment follows the two-sublattice ($s = A$ and B within a unit cell) description first developed by Herrmann[107] [same as Eq. (4), but added by the Zeeman term], where $\hat{\boldsymbol{S}}_i^s$ represents the Fe^{3+} spin operator for sublattice s within the ith unit cell, a total of N_0 unit cells are considered, μ_B is the Bohr magneton, g^{Fe} is the g-factor tensor, $\boldsymbol{B}^{DC}$ is the external static magnetic field, J_{Fe} (D_y^{Fe}) is the symmetric (DM) exchange constant, and A_x, A_z, and A_{xz} are anisotropy energies. The Er^{3+} Hamiltonian

$$H_{Er} = \sum_{s=A,B}\sum_{i=1}^{N_0}\frac{1}{2}\mu_B\hat{\boldsymbol{R}}_i^s\cdot g^{Er}\cdot\boldsymbol{B}^{DC} + J_{Er}\sum_{n.n}\hat{\boldsymbol{R}}_i^A\cdot\hat{\boldsymbol{R}}_{i'}^B \tag{48}$$

consists of field–spin Zeeman interaction and isotropic $Er^{3+}-Er^{3+}$ interactions. Here, the Er^{3+} spins are modeled to have two sublattices in each unit cell ($s = A$ and B) described using vectors of Pauli operators $\hat{\boldsymbol{R}}_i^s = \hat{\boldsymbol{\sigma}}_i^s \equiv (\hat{\sigma}_{i,x}^s, \hat{\sigma}_{i,y}^s, \hat{\sigma}_{i,z}^s)^t$, g^{Er} is the Er^{3+} g-factor tensor, and J_{Er} is the $Er^{3+}-Er^{3+}$ exchange constant. Finally, the $Fe^{3+}-Er^{3+}$ interaction term, which is responsible for the spin–magnon interaction in the Dicke-like Hamiltonian, reads

$$H_{Er-Fe} = \sum_{s,s'=A,B}\sum_{i=1}^{N_0}[J\hat{\boldsymbol{R}}_i^s\cdot\hat{\boldsymbol{S}}_i^{s'} + \boldsymbol{D}^{s,s'}\cdot(\hat{\boldsymbol{R}}_i^s\times\hat{\boldsymbol{S}}_i^{s'})], \tag{49}$$

where the interaction is considered to be closed in each unit cell, and J and $\boldsymbol{D}^{s,s'}$ are the isotropic and antisymmetric $Er^{3+}-Fe^{3+}$ exchange constants, respectively. Symmetry properties of the crystal reduces $\boldsymbol{D}^{s,s'}$ so they can be described by only two scalars D_x and D_y as

$$\begin{aligned}
\boldsymbol{D}^{A,A} &= (D_x, D_y, 0)^{\mathrm{T}},\\
\boldsymbol{D}^{A,B} &= (-D_x, -D_y, 0)^{\mathrm{T}},\\
\boldsymbol{D}^{B,A} &= (-D_x, D_y, 0)^{\mathrm{T}},\\
\boldsymbol{D}^{B,B} &= (D_x, -D_y, 0)^{\mathrm{T}}.
\end{aligned} \tag{50}$$

By using Eqs. (46)–(50), one is able to obtain a complete picture of the thermodynamic properties of the system. Mean-field calculations correctly predict the order parameter onsets of both Er^{3+} and Fe^{3+} subsystems across the LTPT; see Figs. 47(c) and 47(d) for the thermal averaged values of Er^{3+} spins $\bar{\boldsymbol{\sigma}}^{A/B}$ and Fe^{3+} spins $\boldsymbol{S}^{A/B}$ versus temperature at zero magnetic field. The fact that $\bar{\sigma}_z = \bar{\sigma}_z^A = -\bar{\sigma}_z^B$ becomes finite suggests the development of collinear AFM order in the Er^{3+} subsystem along the z axis, while the exchange of weight between $\bar{S}_z = -\bar{S}_z^A = \bar{S}_z^B$ and $\bar{S}_y = \bar{S}_y^A = -\bar{S}_y^B$ suggests rotation of the Fe^{3+} AFM vector within the y–z plane; these match the experimental phenomenology of the LTPT. Furthermore, mean-field calculations with $\boldsymbol{B}^{DC}\|x$ give the phase diagram shown in Fig. 47(e), in which the color intensity encodes the AFM order parameter within the Er^{3+} sector. Application of a magnetic field destabilizes the low-temperature Γ_{12} phase by restoring the system back to the Γ_2 phase; this again agrees with previous experimental findings[91,357].

To establish the relation of the spin model of $ErFeO_3$ with the Dicke model in the context of quantum optics and SRPT, Bamba *et al.*[356] rewrote the overall spin Hamiltonian Eqs. (46)–(50) into the second quantized form

$$\begin{aligned}
H = &\sum_{K=0,\pi}\hbar\omega_K\hat{a}_K^\dagger\hat{a}_K + E_x\hat{\Sigma}_x^+ + \sum_{\xi=x,y,z}g_\xi^{Er}\mu_B B_\xi^{DC}\hat{\Sigma}_\xi^+\\
&+\frac{4z_{Er}J_{Er}}{N_0}\hat{\Sigma}^A\cdot\hat{\Sigma}^B + \frac{\sqrt{2}\hbar g_x}{\sqrt{N_0}}(a_\pi^\dagger + a_\pi)\hat{\Sigma}_x^+\\
&+\frac{i\sqrt{2}\hbar g_y}{\sqrt{N_0}}(a_0^\dagger - a_0)\hat{\Sigma}_y^+ + \frac{\sqrt{2}\hbar g_{y'}}{\sqrt{N_0}}(a_\pi^\dagger + a_\pi)\hat{\Sigma}_y^-\\
&+\frac{i\sqrt{2}\hbar g_z}{\sqrt{N_0}}(a_\pi^\dagger - a_\pi)\hat{\Sigma}_z^- + \frac{\sqrt{2}\hbar g_{z'}}{\sqrt{N_0}}(a_0^\dagger + a_0)\hat{\Sigma}_z^+.
\end{aligned} \tag{51}$$

The two Fe^{3+} magnons with frequency ω_K are written as creation ($\hat{a}_K^\dagger$) and annihilation ($\hat{a}_K$) operators, with $K = 0$, π denoting the FM and AFM modes, respectively. $E_x = h\times 0.023$ THz is the zero-field splitting of the Er^{3+} EPR mode. $\hat{\Sigma}^{A/B} \equiv \frac{1}{2}\sum_{i=1}^{N_0}\hat{\boldsymbol{R}}_i^{A/B}$ is the large-spin operator for Er^{3+}, with $\hat{\Sigma}^{\pm} \equiv \hat{\Sigma}^A \pm \hat{\Sigma}^B$. g_x, g_y, $g_{y'}$, g_z, and $g_{z'}$ are coefficients for terms that couple one of the Fe^{3+} magnon fields with an Er^{3+} large-spin component, and can be calculated by a material parameter set already known through prior experiments. Estimates of energy scales enable certain coupling terms to be dropped, but the coupling term led by the g_z coefficient, the first term on line 3 of Eq. (51), is the most important because it relates the Fe^{3+} quasi-AFM magnon ($a_\pi^\dagger - a_\pi$) with the z-axis AFM vector ($\hat{\Sigma}_z^-$) of the Er^{3+} spins, which develop spontaneous order across an LTPT. Equation (51) formally resembles the Dicke Hamiltonian in quantum optics, but it extends the quantum optical model in complexity because it involves multiple magnon modes (as opposed to the single-mode description in the Dicke model) and the magnon–spin interactions are anisotropic; Bamba *et al.*[356] named it an extended, multi-mode, and anisotropic Dicke model. Furthermore, the key feature of Eq. (51) is that the A^2-term does not appear for spin–spin exchange interactions, giving the model significant potential to host a magnonic SRPT.

To investigate whether the LTPT is a magnonic SRPT, Bamba *et al.*[356] adopted a semiclassical method with the extended, multi-mode, and anisotropic Dicke model, which fully reproduced the thermodynamic properties predicted by the mean-field calculations. Furthermore, they switched on and off certain terms in the Hamiltonian to distinguish impacts from different terms on the phase boundary of the LTPT. As shown in Fig. 47(f), the LTPT temperature remains finite even when the $Er^{3+}-Er^{3+}$ exchange interaction is eliminated, suggesting that the $Er^{3+}-Fe^{3+}$ interaction alone is able to cause the LTPT. While the $Er^{3+}-Er^{3+}$ interaction energy scale (J_{Er}) is identified to play a significant role in describing the Er^{3+} AFM phase boundary, it is only by including the $Er^{3+}-Fe^{3+}$ interaction that one can describe simultaneous ordering of both Er^{3+} and Fe^{3+} across the LTPT. These results determine the nature of the LTPT to be magnonic SRPT, representing the first-time demonstration of the long-sought SRPT in thermal equilibrium.

Building upon the extended, multi-mode, and anisotropic Dicke Hamiltonian [Eq. (51)], Marquez Peraca *et al.*[358] have discovered an additional field-induced phase emerging from the low-temperature phase diagram when an external magnetic

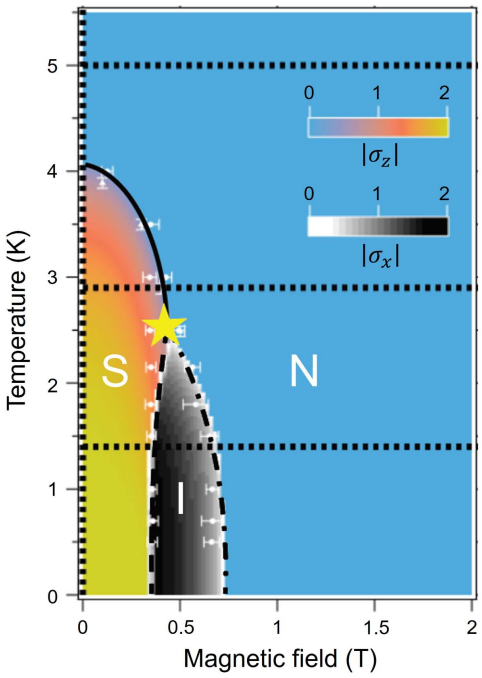

Fig. 48 Temperature-field phase diagram for $\boldsymbol{B}^{DC}\|z$[358]. Between the normal "N" phase and the superradiant "S" phase, a new intermediate "I" phase emerges. The S-to-I transition is first-order. The S-to-N and I-to-N transitions are both second-order.

field is applied along the z axis of the $ErFeO_3$ crystal. The Γ_{12} phase, described as the magnonic superradiant phase, is denoted as the "S" phase, while the normal Γ_2 phase is denoted as the "N" phase. As shown in Fig. 48, for temperatures above 2.5 K, an increase of the magnetic field simply shrinks the S phase boundary in a fashion similar to the $\boldsymbol{B}^{DC}\|x$ case shown in Fig. 47(e). However, when the system is cooled below 2.5 K, an intermediate phase, labeled "I," emerges. This phase exhibits a strong Er^{3+} AFM order parameter $\bar{\sigma}_x = \bar{\sigma}_x^A - \bar{\sigma}_x^B$ along the x axis of the crystal, as opposed to the strong σ_z component in the S phase. Computation of the free-energy landscape suggests that the S-to-I phase transition is a first-order spin–flop transition where the ordered Er^{3+} spins abruptly switch their easy axis from z to x as the magnetic field increases. If the field increases further, an I-to-N transition occurs, and the transition is shown to be second order. Low-temperature magneto-spectroscopy data were found to be in agreement with the theoretical phase diagram. The appearance of the I phase from the extended Dicke Hamiltonian highlights the richness of the magnon SRPT model that goes beyond the standard Dicke model in quantum optics.

6.3 Quantum Simulation of the Anisotropic Hopfield Model and Two-Mode Vacuum Squeezing

In addition to the magnon SRPT, $RFeO_3$ systems have been applied in a broader context as quantum simulators of cooperative light–matter Hamiltonians. Recently, Makihara *et al.*[359] have used $YFeO_3$ to demonstrate the unusual properties of magnon squeezing that arises from an anisotropic Hopfield Hamiltonian. Here, the word "anisotropic" has a different meaning from the anisotropic Dicke model of $ErFeO_3$ mentioned in Subsection 6.2, which describes the direction-dependent coupling of Er^{3+} moments with Fe^{3+} magnons. In $YFeO_3$, Y^{3+} is nonmagnetic, so it would not couple to Fe^{3+} magnons. Instead, the "anisotropy" here refers to the fact that the coupling strengths characterizing the co-rotating terms and the counter-rotating terms in the interaction Hamiltonian are different. Following this definition, the standard Dicke Hamiltonian [Eq. (38)] is isotropic because the co-rotating terms $(ab^\dagger - a^\dagger b)$ and the counter-rotating terms $(a^\dagger b^\dagger - ab)$ share the same coupling coefficient Ω_0.

Makihara *et al.*[359] achieved the anisotropic Hopfield Hamiltonian by applying a magnetic field misaligned from the crystal axis of $YFeO_3$ and harnessing the resultant USC between quasi-FM and quasi-AFM modes of the Fe^{3+} spins. As shown in Fig. 49(a), an external magnetic field is applied at an

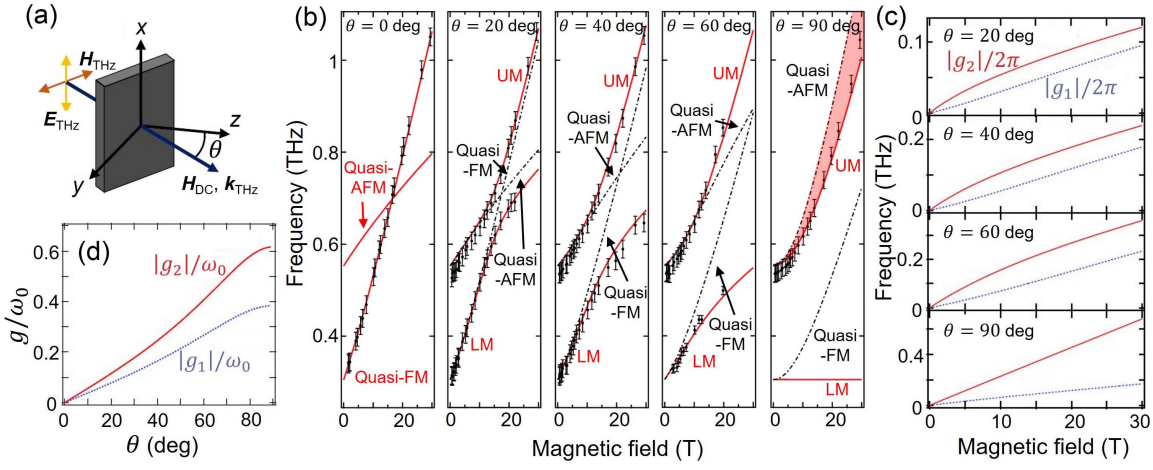

Fig. 49 $YFeO_3$ as a quantum simulator of the anisotropic Hopfield Hamiltonian[359]. (a) Experimental geometry. (b) Experimental mode frequencies (with error bars) versus magnetic field for various tilt angles θ. Theoretical mode calculations using the full Hamiltonian (red solid) and decoupled Hamiltonian (black dashed) are overlaid. (c) g_1 and g_2 versus field for various θ. (d) g_1 and g_2 versus θ at the zero-detuning magnetic field. Reproduced with permission from Ref. [359].

intermediate angle θ between the y axis and z axis, and a THz pulse whose magnetic field polarizes along the x axis propagates through the crystal to probe the magnon frequencies and magnon–magnon coupling. The external field required to observe sizable magnon–magnon coupling should be as large as 30 T, which was supplied by a unique table-top pulsed magnet[138,360] coupled with a broadband optical cryostat.

We first explain qualitatively why magnon–magnon coupling is induced by a misaligned magnetic field. At zero field, or finite fields aligned along the z axis ($\theta = 0$), the two-fold rotation around the z axis (C_{2z}) is a symmetry operator of the crystal (Γ_4 phase). The operator C_{2z} is therefore within the group of the Schrödinger equation, and any eigen-mode of the spin Hamiltonian must be characterized as either even or odd under the operation. The quasi-FM (quasi-AFM) mode is odd (even) under C_{2z}. Magnon–magnon coupling would not occur at $\theta = 0$ since they are both eigen-modes that diagonalize the Hamiltonian. When $\theta \neq 0$, the magnetic field causes a tilt in the spin structure that breaks C_{2z}. Quasi-FM and quasi-AFM modes, which according to definition should still retain their transformation properties under C_{2z}, are no longer well-defined eigen-modes, and thus would couple to one another. Makihara *et al.*[359] worked out the mathematics and showed that when the equation of motion is written using the basis of the FM vector $\boldsymbol{F} = \boldsymbol{S}^A + \boldsymbol{S}^B$ and AFM vector $\boldsymbol{G} = \boldsymbol{S}^A - \boldsymbol{S}^B$, where $\boldsymbol{S}^A$ and $\boldsymbol{S}^B$ are the two Fe^{3+} sublattices [Eqs. (1) and (3)]; the time dynamics of the fluctuations of the $\boldsymbol{F}$ and $\boldsymbol{G}$ vectors, $\delta\boldsymbol{F}$ and $\delta\boldsymbol{G}$, obey

$$\begin{bmatrix} \delta\dot{F}_x \\ \delta\dot{F}_y \\ \delta\dot{G}_x \\ \delta\dot{G}_y \end{bmatrix} = 2\gamma \sin\beta_z \begin{bmatrix} 0 & 2A_y & D_{yx} & 0 \\ -2A_x & 0 & 0 & -D_{xy} \\ D_{xy} & 0 & 0 & 2B_y \\ 0 & -D_{yx} & -2B_x & 0 \end{bmatrix} \begin{bmatrix} \delta F_x \\ \delta F_y \\ \delta G_x \\ \delta G_y \end{bmatrix}, \tag{52}$$

where γ is the gyromagnetic ratio, β_z is the static tilt angle of $\boldsymbol{S}^{A/B}$ from the a–b plane, and A_x, A_y, B_x, B_y, D_{xy}, and D_{yx} are coefficients calculated from spin model parameters. The 4×4 matrix can be divided into four blocks of 2×2 matrices. Blocks involving A_x, A_y, B_x, and B_y couple only components within $\delta\boldsymbol{F}$ or $\delta\boldsymbol{G}$, while off-diagonal blocks that contain D_{xy} and D_{yx} (which are functions of θ) couple $\delta\boldsymbol{F}$ with $\delta\boldsymbol{G}$.

As shown in Fig. 49(b), as θ progressively increases from zero to $\pi/2$, the modes identified by experiment show stronger repulsions, that is, the coupled modes (red solid, labeled by UM and LM) show larger frequency separations from the uncoupled quasi-FM and quasi-AFM modes (black dashed). The uncoupled modes are calculated by setting $D_{xy} = D_{yx} = 0$ in Eq. (52). Counterintuitive behavior emerges for $\theta = \pi/2$, where the upper mode (UM) becomes redshifted, rather than blueshifted from the coupled mode; see the red shaded region, which is not expected for the standard Hopfield Hamiltonian [Figs. 44(c) and 44(d)]. Makihara *et al.*[359] pointed out that the reason is that the spin Hamiltonian, when mapped to the Hopfield Hamiltonian,

$$H = \hbar\omega_{0a}\left(\hat{a}^\dagger\hat{a} + \frac{1}{2}\right) + \hbar\omega_{0b}\left(\hat{b}^\dagger\hat{b} + \frac{1}{2}\right) + i\hbar g_1(\hat{a}\hat{b}^\dagger - \hat{a}^\dagger\hat{b}) + i\hbar g_2(\hat{a}^\dagger\hat{b}^\dagger - \hat{a}\,\hat{b}), \tag{53}$$

is anisotropic. Here, $\hat{a}$ ($\hat{a}^\dagger$) and $\hat{b}$ ($\hat{b}^\dagger$) are annihilation (creation) operators for the decoupled quasi-FM and quasi-AFM magnons, respectively, and g_1 and g_2 are coupling coefficients for the co-rotating and counter-rotating terms, respectively. The redshifted UM originates from an exceptionally large g_2, for which the polariton frequencies are dominated by the vacuum Bloch–Siegert shift[328] that arises from the counter-rotating terms of the Hamiltonian. Analytical calculations of g_1 and g_2 versus field for various θ values are plotted in Fig. 49(c). For all $\theta \neq 0$, $g_2 > g_1$, and $g_2 - g_1$ becomes more prominent when θ approaches $\pi/2$ and at stronger fields, which corroborates the observation of the anomalous frequency shifts in Fig. 49(b). Figure 49(d) shows g_1 and g_2 versus θ at the zero-detuning magnetic fields, again exhibiting consistency with this understanding.

Achieving the anisotropic Hopfield Hamiltonian [Eq. (53)] possessing tunable g_1 and g_2 with $g_2 > g_1$ is a unique finding of this work, and is expected to open up opportunities to search for more exotic quantum phenomena. In particular, the exceptionally large counter-rotating terms will amplify the two-mode vacuum squeezing of the coupled ground state. Makihara *et al.*[359] defined a generalized magnon annihilation operator from $\hat{a}$ and $\hat{b}$,

$$\hat{c}_{\phi,\psi} = \hat{a}\cos\phi + e^{i\psi}\hat{b}\sin\phi, \tag{54}$$

and a quadrature by this operator as

$$\hat{X}_{\phi,\psi,\varphi} = (\hat{c}_{\phi,\psi}e^{i\varphi} + \hat{c}^\dagger_{\phi,\psi}e^{-i\varphi})/2, \tag{55}$$

where ϕ, ψ, and φ are phase factors. With the help of the Hopfield–Bogoliubov transformation, the variance $\langle 0|(\hat{X}_{\phi,\psi,\varphi})^2|0\rangle$ with respect to the coupled ground state $|0\rangle$ was minimized to find the optimal ϕ, ψ, and φ. They found that the fluctuation of the quadrature can be reduced by up to 5.9 dB at 30 T for $\theta = \pi/2$, which is a direct consequence of the large counter-rotating terms under these experimental conditions.

Building upon the same line of theory, Hayashida *et al.*[338] further discovered perfect intrinsic vacuum squeezing at an SRPT critical point. They started from a standard Dicke Hamiltonian, performed the Holstein–Primakov transformation, and defined the two-mode annihilation operator and the associated quadrature in a way similar to Eqs. (54) and (55). They tuned ϕ, ψ, and φ to minimize the quadrature for every light–matter coupling strength Ω_0, and plotted the optimized quadrature versus Ω_0/ω_{eg} as in Fig. 50. At the SRPT critical point, the $\Omega_0/\omega_{eg} = 0.5$ point at which the lower polariton softens to zero frequency, the optimized quadrature vanishes, suggesting perfect squeezing. The single-mode quadrature associated with $\hat{X}_{0,0,\pi/2}$ also exhibits suppressed fluctuations, despite being incomplete. The product of the optimized quadrature with its orthogonal always gives 1/4, satisfying the uncertainty principle.

The two-mode vacuum squeezing is useful for applications such as quantum metrology and decoherence-robust quantum information technology[361]. Its realization in Dicke-like models in thermal equilibrium (i.e., instrinsic squeezing) presents a unique advantage compared to standard photon squeezing protocols, which usually rely on out-of-equilibrium approaches[362,363]. The squeezing should also be resilient against thermal fluctuations at finite temperatures. Future research

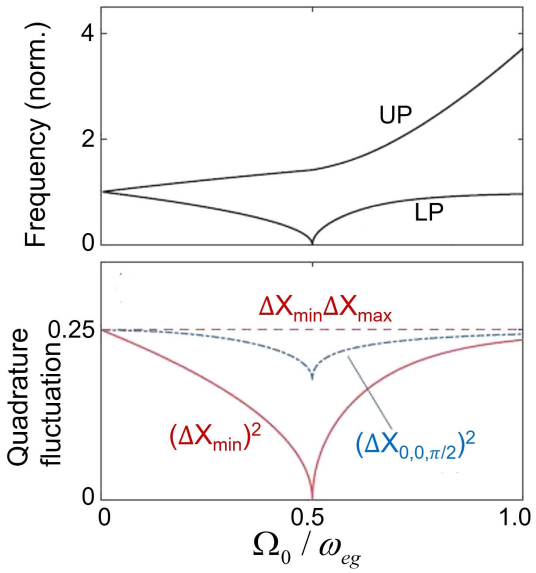

Fig. 50 Perfect intrinsic squeezing at an SRPT critical point[338]. Minimized quadrature fluctuation (red) versus coupling strength shows perfect suppression at the SRPT transition point. Upper panel shows complementary polariton mode frequencies.

awaits to explore these unprecedented functionalities in more depth.

7 Summary and Outlook

In this paper, we reviewed THz-frequency phenomena associated with spin dynamics in the $RFeO_3$ class. We first discussed how one can use THz radiation to probe magnetic phase transitions in equilibrium. While the polarization selection rule of acoustic magnons is a useful indicator of spin reorientation transitions, electromagnons associated with dynamic magnetoelectric coupling appear as a unique class of excitation in noncentrosymmetric low-temperature magnetic phases. We then reviewed the scenario where laser radiation drives the system far from equilibrium, and a few emergent microscopic pathways for laser manipulation of magnetic order. Further, for AFM spintronic applications, the ability to achieve coherent quantum control over magnon dynamics is important. Thus, we reviewed a variety of protocols to manipulate coherent magnons in time and space. Finally, new insights into the connection between dynamic magnetic coupling in condensed matter systems and ultrastrong light–matter coupling in the setting of cavity quantum electrodynamics were provided; this sets the stage for novel approaches of manipulating condensed matter phases through tools and concepts in quantum optics.

In the introduction (Section 1), we mentioned that an advantage of presenting a comprehensive survey on various spintronic phenomena related to a single material class is that the connections between various physical phenomena can be identified more easily. Looking into the future, it is exactly this type of connection we seek that may enable the community to invent new protocols for active spin control and quantum phase engineering. For example, a direction emerging very recently explores the marriage of nonlinear phononics (Subsection 4.3) and nonlinear magnonics (Subsection 5.4), where multi-dimensional THz spectroscopy can be utilized to precisely characterize the strength of anharmonic phonon–phonon[317], spin–spin[322,364], or even spin–phonon interactions[278]. Second, a variety of analogies can be drawn from the idea of Floquet engineering of electronic structures (Subsection 4.5) and the notion of ultrastrong light–matter coupling in cavity quantum materials (Subsection 6.1)[71,72,294]. Their descriptions share a lot of similarities[250,328] since both investigate coherent light–matter interaction Hamiltonians; the former relies on external pump light while the latter on the cavity vacuum field. Being equipped with the knowledge of magnonic SRPTs, one might be interested in engineering unusual light-dressed magnetic states with quantum controllable counter-rotating interactions (Subsections 6.2 and 6.3). The third idea arises from the connection between electromagnons (Subsection 3.3) and the rare-earth pathway of laser manipulation of Fe^{3+} order (Subsection 4.4). Electromagnons are only starting to be understood by using THz spectroscopy probes recently, but they have not been the subject of strong-field driving in $RFeO_3$. However, since such an excitation unambiguously involves both the Fe^{3+} and R^{3+} subsystems (because symmetry can be broken only by R^{3+} ordering within the matrix of Fe^{3+} order), nonperturbative driving of this mode by intense THz radiation can potentially be even more efficient in controlling the Fe^{3+} order than the method of anisotropy torque created by driving the CFTs of R^{3+}. Indeed, spin manipulation that results from driving an electromagnon mode has been demonstrated in $TbMnO_3$[183]. Fourth, one can also explore novel device designs by leveraging the physical principles discussed here. The combination of ultralong magnon decoherence time (Section 5) and laser-manipulable magnetic phases (Section 4) opens the door for magnon waveguides and logical operation units with unprecedented optical controllability.

We believe that the above examples are merely the tip of the iceberg of potential connections one can make within the existing demonstrations of THz-frequency spintronic phenomena in $RFeO_3$. We hope that the same ideology can apply to a wider material class, to trigger a broader range of interdisciplinary efforts for fostering the field of THz spintronics and ultrafast condensed matter physics.

Acknowledgments

X. L. acknowledges support from the Caltech Postdoctoral Prize Fellowship and the Institute for Quantum Information and Matter (IQIM). J. K. acknowledges support from the Robert A. Welch Foundation through Grant No. C-1509 and the U.S. Army Research Office through Grant No. W911NF-17-1-0259.

References

1. G. A. Stewart and W. Lampl, and ATLAS Collaboration, "How to review 4 million lines of ATLAS code," *J. Phys.* **898**, 072013 (2017).
2. I. Žutić, J. Fabian, and S. Das Sarma, "Spintronics: fundamentals and applications," *Rev. Mod. Phys.* **76**, 323 (2004).
3. J. Sinova and I. Žutić, "New moves of the spintronics tango," *Nat. Mater.* **11**, 368 (2012).
4. V. Baltz *et al.*, "Antiferromagnetic spintronics," *Rev. Mod. Phys.* **90**, 015005 (2018).
5. T. Jungwirth *et al.*, "Antiferromagnetic spintronics," *Nat. Nanotechnol.* **11**, 231 (2016).
6. D. G. Feitelson, *Optical Computing: Survey for Computer Scientists* (MIT Press, 1992).
7. A. V. Chumak *et al.*, "Magnon spintronics," *Nat. Phys.* **11**, 453 (2015).

8. A. Mahmoud *et al.*, "Introduction to spin wave computing," *J. Appl. Phys.* **128**, 161101 (2020).
9. B. Lenk *et al.*, "The building blocks of magnonics," *Phys. Rep.* **507**, 107 (2011).
10. G. Csaba, Á. Papp, and W. Porod, "Perspectives of using spin waves for computing and signal processing," *Phys. Lett. A* **381**, 1471 (2017).
11. "The rise of quantum materials," *Nat. Phys.* **12**, 105 (2016).
12. P. W. Anderson, "More is different: broken symmetry and the nature of the hierarchical structure of science," *Science* **177**, 393 (1972).
13. A. Alexandradinata *et al.*, "The future of the correlated electron problem," arXiv:2010.00584 (2020).
14. M. Imada, A. Fujimori, and Y. Tokura, "Metal-insulator transitions," *Rev. Mod. Phys.* **70**, 1039 (1998).
15. H.-C. Jiang and T. P. Devereaux, "Superconductivity in the doped Hubbard model and its interplay with next-nearest hopping t'," *Science* **365**, 1424 (2019).
16. A. C. Hewson, *The Kondo Problem to Heavy Fermions* (Cambridge University Press, 1993).
17. J. Strecka and M. Jascur, "A brief account of the Ising and Ising-like models: mean-field, effective-field and exact results," arXiv:1511.03031 (2015).
18. A. Kitaev, "Anyons in an exactly solved model and beyond," *Ann. Phys.* **321**, 2 (2006).
19. F. Krausz *et al.*, "Femtosecond solid-state lasers," *IEEE J. Sel. Top. Quantum Electron.* **28**, 2097 (1992).
20. S. Backus *et al.*, "High power ultrafast lasers," *Rev. Sci. Instrum.* **69**, 1207 (1998).
21. R. D. Averitt *et al.*, "Ultrafast conductivity dynamics in colossal magnetoresistance manganites," *Phys. Rev. Lett.* **87**, 017401 (2001).
22. J. Demsar *et al.*, "Pair-breaking and superconducting state recovery dynamics in MgB_2," *Phys. Rev. Lett.* **91**, 267002 (2003).
23. J. Demsar *et al.*, "Quasiparticle relaxation dynamics in heavy fermion compounds," *Phys. Rev. Lett.* **91**, 027401 (2003).
24. N. Gedik *et al.*, "Single-quasiparticle stability and quasiparticle-pair decay in $YBa_2Cu_3O_{6.5}$," *Phys. Rev. B* **70**, 014504 (2004).
25. E. E. M. Chia *et al.*, "Quasiparticle relaxation across the spin-density-wave gap in the itinerant antiferromagnet $UNiGa_5$," *Phys. Rev. B* **74**, 140409 (2006).
26. J. Demsar, K. Biljaković, and D. Mihailovic, "Single particle and collective excitations in the one-dimensional charge density wave solid $K_{0.3}MoO_3$ probed in real time by femtosecond spectroscopy," *Phys. Rev. Lett.* **83**, 800 (1999).
27. T. Mertelj *et al.*, "Quasiparticle relaxation dynamics in spin-density-wave and superconducting $SmFeAsO_{1-x}F_x$ single crystals," *Phys. Rev. B* **81**, 224504 (2010).
28. F. Novelli *et al.*, "Witnessing the formation and relaxation of dressed quasi-particles in a strongly correlated electron system," *Nat. Commun.* **5**, 5112 (2014).
29. X. Li *et al.*, "Keldysh space control of charge dynamics in a strongly driven Mott insulator," *Phys. Rev. Lett.* **128**, 187402 (2022).
30. S. Wall *et al.*, "Quantum interference between charge excitation paths in a solid-state Mott insulator," *Nat. Phys.* **7**, 114 (2011).
31. A. Kirilyuk, A. V. Kimel, and T. Rasing, "Ultrafast optical manipulation of magnetic order," *Rev. Mod. Phys.* **82**, 2731 (2010).
32. A. Polkovnikov *et al.*, "Colloquium: nonequilibrium dynamics of closed interacting quantum systems," *Rev. Mod. Phys.* **83**, 863 (2011).
33. M. Heyl, "Dynamical quantum phase transitions: a review," *Rep. Prog. Phys.* **81**, 054001 (2018).
34. A. Mitra, "Quantum quench dynamics," *Annu. Rev. Condens. Matter Phys.* **9**, 245 (2018).
35. T. Kinoshita, T. Wenger, and D. S. Weiss, "A quantum Newton's cradle," *Nature* **440**, 900 (2006).
36. X.-C. Zhang and J. Xu, "Generation and detection of THz waves," in *Introduction to THz Wave Photonics* (Springer US, 2010), p. 27.
37. R. W. Boyd, *Nonlinear Optics* (Academic Press, 2008).
38. H. A. Hafez *et al.*, "Intense terahertz radiation and their applications," *J. Opt.* **18**, 093004 (2016).
39. H. Aoki *et al.*, "Nonequilibrium dynamical mean-field theory and its applications," *Rev. Mod. Phys.* **86**, 779 (2014).
40. U. Schollwöck, "The density-matrix renormalization group," *Rev. Mod. Phys.* **77**, 259 (2005).
41. *Fundamentals of Time-Dependent Density Functional Theory*, Vol. **837** (Springer Berlin Heidelberg, 2012).
42. G. Stefanucci and R. van Leeuwen, *Nonequilibrium Many-Body Theory of Quantum Systems: A Modern Introduction* (Cambridge University Press, 2013).
43. Y. Murakami and P. Werner, "Nonequilibrium steady states of electric field driven Mott insulators," *Phys. Rev. B* **98**, 075102 (2018).
44. N. Tancogne-Dejean, M. A. Sentef, and A. Rubio, "Ultrafast transient absorption spectroscopy of the charge-transfer insulator NiO: beyond the dynamical Franz-Keldysh effect," *Phys. Rev. B* **102**, 115106 (2020).
45. T. Oka, "Nonlinear doublon production in a Mott insulator: Landau-Dykhne method applied to an integrable model," *Phys. Rev. B* **86**, 075148 (2012).
46. M. H. Michael *et al.*, "Generalized Fresnel-Floquet equations for driven quantum materials," *Phys. Rev. B* **105**, 174301 (2022).
47. D. N. Basov *et al.*, "Electrodynamics of correlated electron materials," *Rev. Mod. Phys.* **83**, 471 (2011).
48. N. P. Armitage, "Electrodynamics of correlated electron systems," arXiv:0908.1126 (2009).
49. J. Walowski and M. Münzenberg, "Perspective: ultrafast magnetism and THz spintronics," *J. Appl. Phys.* **120**, 140901 (2016).
50. C. N. R. Rao, "Transition metal oxides," *Annu. Rev. Phys. Chem.* **40**, 291 (1989).
51. Y. Tokura, "Correlated-electron physics in transition-metal oxides," *Phys. Today* **56**, 50 (2003).
52. C. Schlenker *et al.*, "Charge density wave instabilities and transport properties of the low dimensional molybdenum bronzes and oxides," in *Low-Dimensional Electronic Properties of Molybdenum Bronzes and Oxides*, C. Schlenker, ed., Vol. **11** (Springer Netherlands, 1989), p. 159.
53. Y. Tokura and N. Nagaosa, "Orbital physics in transition-metal oxides," *Science* **288**, 462 (2000).
54. S. Dong and J.-M. Liu, "Recent progress of multiferroic perovskite manganites," *Mod. Phys. Lett. B* **26**, 1230004 (2012).
55. K. M. Shen and J. C. S. Davis, "Cuprate high-Tc superconductors," *Mater. Today* **11**, 14 (2008).
56. C. Wang and Y. Liu, "Ultrafast optical manipulation of magnetic order in ferromagnetic materials," *Nano Converg.* **7**, 35 (2020).
57. A. M. Kalashnikova, A. V. Kimel, and R. V. Pisarev, "Ultrafast opto-magnetism," *Phys. Usp.* **58**, 969 (2015).
58. C. Giannetti *et al.*, "Ultrafast optical spectroscopy of strongly correlated materials and high-temperature superconductors: a non-equilibrium approach," *Adv. Phys.* **65**, 58 (2016).
59. R. D. Averitt and A. J. Taylor, "Ultrafast optical and far-infrared quasiparticle dynamics in correlated electron materials," *J. Phys.* **14**, R1357 (2002).
60. J. Zhang and R. D. Averitt, "Dynamics and control in complex transition metal oxides," *Annu. Rev. Mater. Res.* **44**, 19 (2014).
61. M. Gandolfi *et al.*, "Emergent ultrafast phenomena in correlated oxides and heterostructures," *Phys. Scr.* **92**, 034004 (2017).
62. A. de la Torre *et al.*, "Colloquium: nonthermal pathways to ultrafast control in quantum materials," *Rev. Mod. Phys.* **93**, 041002 (2021).
63. R. Mankowsky, M. Först, and A. Cavalleri, "Non-equilibrium control of complex solids by nonlinear phononics," *Rep. Prog. Phys.* **79**, 064503 (2016).

64. A. S. Disa, T. F. Nova, and A. Cavalleri, "Engineering crystal structures with light," *Nat. Phys.* **17**, 1087 (2021).
65. T. Oka and S. Kitamura, "Floquet engineering of quantum materials," *Annu. Rev. Condens. Matter Phys.* **10**, 387 (2019).
66. M. Bukov, L. D'Alessio, and A. Polkovnikov, "Universal high-frequency behavior of periodically driven systems: from dynamical stabilization to Floquet engineering," *Adv. Phys.* **64**, 139 (2015).
67. P. Němec *et al.*, "Antiferromagnetic opto-spintronics," *Nat. Phys.* **14**, 229 (2018).
68. O. Gomonay *et al.*, "Antiferromagnetic spin textures and dynamics," *Nat. Phys.* **14**, 213 (2018).
69. E. V. Gomonay and V. M. Loktev, "Spintronics of antiferromagnetic systems (review article)," *Low Temp. Phys.* **40**, 17 (2014).
70. J. Lu *et al.*, "Two-dimensional spectroscopy at terahertz frequencies," *Top. Curr. Chem.* **376**, 6 (2018).
71. F. Schlawin, D. M. Kennes, and M. A. Sentef, "Cavity quantum materials," *Appl. Phys. Rev.* **9**, 011312 (2022).
72. J. Bloch *et al.*, "Strongly correlated electron–photon systems," *Nature* **606**, 41 (2022).
73. P. Forn-Díaz *et al.*, "Ultrastrong coupling regimes of light-matter interaction," *Rev. Mod. Phys.* **91**, 025005 (2019).
74. A. F. Kockum *et al.*, "Ultrastrong coupling between light and matter," *Nat. Rev. Phys.* **1**, 19 (2019).
75. R. L. White, "Review of recent work on the magnetic and spectroscopic properties of the rare-earth orthoferrites," *J. Appl. Phys.* **40**, 1061 (1969).
76. E. F. Bertaut, "Representation analysis of magnetic structures," *Acta Cryst.* **24**, 217 (1968).
77. M. S. Dresselhaus, G. Dresselhaus, and A. Jorio, *Group Theory: Application to the Physics of Condensed Matter* (Springer-Verlag, 2008).
78. T. Yamaguchi and K. Tsushima, "Magnetic symmetry of rare-earth orthochromites and orthoferrites," *Phys. Rev. B* **8**, 5187 (1973).
79. E. Li *et al.*, "Spin switching in single crystal $PrFeO_3$ and spin configuration diagram of rare earth orthoferrites," *J. Alloys Compd.* **811**, 152043 (2019).
80. T. Yamaguchi, "Theory of spin reorientation in rare-earth orthochromites and orthoferrites," *J. Phys. Chem. Solids* **35**, 479 (1974).
81. M. P. Zic *et al.*, "Coupled spin waves and crystalline electric field levels in candidate multiferroic $ErFeO_3$," *J. Appl. Phys.* **130**, 014102 (2021).
82. R. M. Bozorth, V. Kramer, and J. P. Remeika, "Magnetization in single crystals of some rare-earth orthoferrites," *Phys. Rev. Lett.* **1**, 3 (1958).
83. G. Gorodetsky, B. Sharon, and S. Shtrikman, "Magnetic properties of an antiferromagnetic orthoferrite," *J. Appl. Phys.* **39**, 1371 (1968).
84. S. J. Yuan *et al.*, "First-order spin reorientation transition and specific-heat anomaly in $CeFeO_3$," *J. Appl. Phys.* **114**, 113909 (2013).
85. C. Ritter, M. Ceretti, and W. Paulus, "Determination of the magnetic structures in orthoferrite $CeFeO_3$ by neutron powder diffraction: first order spin reorientation and appearance of an ordered Ce-moment," *J. Phys.* **33**, 215802 (2021).
86. G. P. Vorob'ev *et al.*, "Unusual nature of spin reorientation in $HoFeO_3$," *Zh. Eksp. Teor. Fiz* **95**, 1049 (1989).
87. A. M. Balbashov *et al.*, "Anomalies of high-frequency magnetic properties and new orientational transitions in $HoFeO_3$," *JETP* **68**, 629 (1989).
88. X. Zeng *et al.*, "Terahertz time domain spectroscopic investigation of spin reorientation transitions in $HoFeO_3$," *Opt. Express* **23**, 31956 (2015).
89. A. K. Ovsianikov *et al.*, "Magnetic phase diagram of $HoFeO_3$ by neutron diffraction," *J. Magn. Magn. Mater.* **557**, 169431 (2022).
90. K. P. Belov *et al.*, "On the character of phase transitions in $ErFeO_3$," *Phys. Status Solidi* **36**, 415 (1976).
91. A. M. Kadomtseva, I. B. Krynetski, and V. M. Matveev, "Nature of the spontaneous and field-induced low-temperature orientational transitions in erbium orthoferrite," *JETP* **52**, 732 (1980).
92. G. Deng *et al.*, "The magnetic structures and transitions of a potential multiferroic orthoferrite $ErFeO_3$," *J. Appl. Phys.* **117**, 164105 (2015).
93. M. Marezio, J. P. Remeika, and P. D. Dernier, "The crystal chemistry of the rare earth orthoferrites," *Acta Cryst.* **26**, 2008 (1970).
94. D. L. Wood, J. P. Remeika, and E. D. Kolb, "Optical spectra of rare-earth orthoferrites," *J. Appl. Phys.* **41**, 5315 (1970).
95. S. M. Shapiro, J. D. Axe, and J. P. Remeika, "Neutron-scattering studies of spin waves in rare-earth orthoferrites," *Phys. Rev. B* **10**, 2014 (1974).
96. N. Koshizuka and K. Hayashi, "Raman scattering from magnon excitations in $RFeO_3$," *J. Phys. Soc. Jpn.* **57**, 4418 (1988).
97. Z. Y. Zhao *et al.*, "Ground state and magnetic phase transitions of orthoferrite $DyFeO_3$," *Phys. Rev. B* **89**, 224405 (2014).
98. J. Zaanen, G. A. Sawatzky, and J. W. Allen, "Band gaps and electronic structure of transition-metal compounds," *Phys. Rev. Lett.* **55**, 418 (1985).
99. T. Arima, Y. Tokura, and J. B. Torrance, "Variation of optical gaps in perovskite-type 3*d* transition-metal oxides," *Phys. Rev. B* **48**, 17006 (1993).
100. N. Singh, J. Y. Rhee, and S. Auluck, "Electronic and magneto-optical properties of rare-earth orthoferrites $RFeO_3$ (R = Y, Sm, Eu, Gd and Lu)," *J. Korean Phy. Soc.* **53**, 806 (2008).
101. A. M. Clogston, "Interaction of magnetic crystals with radiation in the range 104–105 cm^{-1}," *J. Appl. Phys.* **31**, S198 (1960).
102. H. C. Gupta, M. Kumar Singh, and L. M. Tiwari, "Lattice dynamic investigation of Raman and infrared wavenumbers at the zone center of orthorhombic $RFeO_3$ (R = Tb, Dy, Ho, Er, Tm) perovskites," *J. Raman Spectrosc.* **33**, 67 (2002).
103. G. V. S. Rao, C. N. R. Rao, and J. R. Ferraro, "Infrared and electronic spectra of rare earth perovskites: ortho-chromites, -manganites and -ferrites," *Appl. Spectrosc.* **24**, 436 (1970).
104. S. Venugopalan *et al.*, "Magnetic and vibrational excitations in rare-earth orthoferrites: a Raman scattering study," *Phys. Rev. B* **31**, 1490 (1985).
105. M. C. Weber *et al.*, "Raman spectroscopy of rare-earth orthoferrites $RFeO_3$ (R = La, Sm, Eu, Gd, Tb, Dy)," *Phys. Rev. B* **94**, 214103 (2016).
106. S. E. Hahn *et al.*, "Inelastic neutron scattering studies of $YFeO_3$," *Phys. Rev. B* **89**, 014420 (2014).
107. G. F. Herrmann, "Resonance and high frequency susceptibility in canted antiferromagnetic substances," *J. Phys. Chem. Solids* **24**, 597 (1963).
108. G. F. Herrmann, "Magnetic resonances and susceptibility in orthoferrites," *Phys. Rev.* **133**, A1334 (1964).
109. R. M. White, R. J. Nemanich, and C. Herring, "Light scattering from magnetic excitations in orthoferrites," *Phys. Rev. B* **25**, 1822 (1982).
110. N. Koshizuka and K. Hayashi, "Temperature dependences of one-magnon light scattering in $RFeO_3$," *J. Magn. Magn. Mater.* **31–34**, 569 (1983).
111. J. R. Shane, "Resonance frequencies of the orthoferrites in the spin reorientation region," *Phys. Rev. Lett.* **20**, 728 (1968).
112. Z. Q. Qiu and S. D. Bader, "Surface magneto-optic Kerr effect," *Rev. Sci. Instrum.* **71**, 1243 (2000).
113. A. B. Schmidt *et al.*, "Spin-dependent electron dynamics in front of a ferromagnetic surface," *Phys. Rev. Lett.* **95**, 107402 (2005).
114. A. Scholl *et al.*, "Ultrafast spin dynamics of ferromagnetic thin films observed by fs spin-resolved two-photon photoemission," *Phys. Rev. Lett.* **79**, 5146 (1997).
115. C. Stamm *et al.*, "Femtosecond modification of electron localization and transfer of angular momentum in nickel," *Nat. Mater.* **6**, 740 (2007).

116. M. P. M. Dean *et al.*, "Ultrafast energy- and momentum-resolved dynamics of magnetic correlations in the photo-doped Mott insulator Sr_2IrO_4," *Nat. Mater.* **15**, 601 (2016).
117. D. G. Mazzone *et al.*, "Laser-induced transient magnons in $Sr_3Ir_2O_7$ throughout the Brillouin zone," *Proc. Natl. Acad. Sci. U.S.A.* **118**, e2103696118 (2021).
118. A. V. Kimel *et al.*, "Ultrafast non-thermal control of magnetization by instantaneous photomagnetic pulses," *Nature* **435**, 655 (2005).
119. R. Iida *et al.*, "Spectral dependence of photoinduced spin precession in $DyFeO_3$," *Phys. Rev. B* **84**, 064402 (2011).
120. H. Regensburger, R. Vollmer, and J. Kirschner, "Time-resolved magnetization-induced second-harmonic generation from the Ni(110) surface," *Phys. Rev. B* **61**, 14716 (2000).
121. B. Koopmans *et al.*, "Ultrafast magneto-optics in nickel: magnetism or optics?" *Phys. Rev. Lett.* **85**, 844 (2000).
122. G. P. Zhang *et al.*, "Paradigm of the time-resolved magneto-optical Kerr effect for femtosecond magnetism," *Nat. Phys.* **5**, 499 (2009).
123. R. V. Mikhaylovskiy *et al.*, "Ultrafast optical modification of exchange interactions in iron oxides," *Nat. Commun.* **6**, 8190 (2015).
124. L. Prochaska *et al.*, "Singular charge fluctuations at a magnetic quantum critical point," *Science* **367**, 285 (2020).
125. X. Li *et al.*, "Observation of photoinduced terahertz gain in GaAs quantum wells: evidence for radiative two-exciton-to-biexciton scattering," *Phys. Rev. Lett.* **125**, 167401 (2020).
126. G. Bossé *et al.*, "Low energy electrodynamics of the Kondo-lattice antiferromagnet $CeCu_2Ge_2$," *Phys. Rev. B* **85**, 155105 (2012).
127. N. J. Laurita *et al.*, "Singlet-triplet excitations and long-range entanglement in the spin-orbital liquid candidate $FeSc_2S_4$," *Phys. Rev. Lett.* **114**, 207201 (2015).
128. B. Cheng *et al.*, "Dielectric anomalies and interactions in the three-dimensional quadratic band touching Luttinger semimetal $Pr_2Ir_2O_7$," *Nat. Commun.* **8**, 2097 (2017).
129. E. Baldini *et al.*, "Discovery of the soft electronic modes of the trimeron order in magnetite," *Nat. Phys.* **16**, 541 (2020).
130. L. Pan *et al.*, "A measure of monopole inertia in the quantum spin ice $Yb_2Ti_2O_7$," *Nat. Phys.* **12**, 361 (2016).
131. X. Zhang *et al.*, "Hierarchy of exchange interactions in the triangular-lattice spin liquid $YbMgGaO_4$," *Phys. Rev. X* **8**, 031001 (2018).
132. P. Chauhan *et al.*, "Tunable magnon interactions in a ferromagnetic spin-1 chain," *Phys. Rev. Lett.* **124**, 037203 (2020).
133. R. Matsunaga *et al.*, "Light-induced collective pseudospin precession resonating with Higgs mode in a superconductor," *Science* **345**, 1145 (2014).
134. H. Chu *et al.*, "Phase-resolved Higgs response in superconducting cuprates," *Nat. Commun.* **11**, 1793 (2020).
135. K. W. Kim *et al.*, "Ultrafast transient generation of spin-density-wave order in the normal state of $BaFe_2As_2$ driven by coherent lattice vibrations," *Nat. Mater.* **11**, 497 (2012).
136. F. Y. Gao *et al.*, "Snapshots of a light-induced metastable hidden phase driven by the collapse of charge order," *Sci. Adv.* **8**, eabp9076 (2022).
137. M. Mitrano *et al.*, "Possible light-induced superconductivity in K_3C_{60} at high temperature," *Nature* **530**, 461 (2016).
138. X. Li *et al.*, "Terahertz Faraday and Kerr rotation spectroscopy of $Bi_{1-x}Sb_x$ films in high magnetic fields up to 30 tesla," *Phys. Rev. B* **100**, 115145 (2019).
139. K. A. Cremin *et al.*, "Photoenhanced metastable c-axis electrodynamics in stripe-ordered cuprate $La_{1.885}Ba_{0.115}CuO_4$," *Proc. Natl. Acad. Sci. U.S.A.* **116**, 19875 (2019).
140. A. M. Balbashov *et al.*, "Submillimeter spectroscopy of antiferromagnetic dielectrics: rare-earth orthoferrites," in *High Frequency Processes in Magnetic Materials* (World Scientific, 1995), p. 56.
141. A. M. Balbashov *et al.*, "High-frequency magnetic properties of dysprosium orthoferrite," *JETP* **61**, 573 (1985).
142. A. M. Balbashov *et al.*, "Soft mode and energy gap in spin-wave spectrum in a second-order orientational phase transition. AFMR in $YFeO_3$," *JETP* **66**, 174 (1987).
143. A. Baydin *et al.*, "Time-domain terahertz spectroscopy in high magnetic fields," *Front. Optoelectron.* **14**, 110 (2021).
144. Q. Wu and X.-C. Zhang, "Free-space electro-optic sampling of terahertz beams," *Appl. Phys. Lett.* **67**, 3523 (1995).
145. G. T. Noe *et al.*, "Single-shot terahertz time-domain spectroscopy in pulsed high magnetic fields," *Opt. Express* **24**, 30328 (2016).
146. Y. Minami *et al.*, "Single-shot measurement of a terahertz electric-field waveform using a reflective echelon mirror," *Appl. Phys. Lett.* **103**, 051103 (2013).
147. H. Y. Hwang *et al.*, "A review of non-linear terahertz spectroscopy with ultrashort tabletop-laser pulses," *J. Mod. Opt.* **62**, 1447 (2015).
148. X. Zhu *et al.*, "High field single- to few-cycle THz generation with lithium niobate," *Photonics* **8**, 183 (2021).
149. M. Liu *et al.*, "Terahertz-field-induced insulator-to-metal transition in vanadium dioxide metamaterial," *Nature* **487**, 345 (2012).
150. X. Yang *et al.*, "Terahertz-light quantum tuning of a metastable emergent phase hidden by superconductivity," *Nat. Mater.* **17**, 586 (2018).
151. X. Li *et al.*, "Terahertz field–induced ferroelectricity in quantum paraelectric $SrTiO_3$," *Science* **364**, 1079 (2019).
152. A. X. Gray *et al.*, "Ultrafast terahertz field control of electronic and structural interactions in vanadium dioxide," *Phys. Rev. B* **98**, 045104 (2018).
153. T. A. Miller *et al.*, "Terahertz field control of in-plane orbital order in $La_{0.5}Sr_{1.5}MnO_4$," *Nat. Commun.* **6**, 8175 (2015).
154. H. Yamakawa *et al.*, "Mott transition by an impulsive dielectric breakdown," *Nat. Mater.* **16**, 1100 (2017).
155. J. Hebling *et al.*, "Velocity matching by pulse front tilting for large area THz-pulse generation," *Opt. Express* **10**, 1161 (2002).
156. J. Hebling *et al.*, "Generation of high-power terahertz pulses by tilted-pulse-front excitation and their application possibilities," *J. Opt. Soc. Am. B* **25**, B6 (2008).
157. K.-L. Yeh *et al.*, "Generation of 10μJ ultrashort terahertz pulses by optical rectification," *Appl. Phys. Lett.* **90**, 171121 (2007).
158. M. Jazbinsek *et al.*, "Organic crystals for THz photonics," *Appl. Sci.* **9**, 882 (2019).
159. S.-H. Lee *et al.*, "Recent progress in acentric core structures for highly efficient nonlinear optical crystals and their supramolecular interactions and terahertz applications," *CrystEngComm* **18**, 7180 (2016).
160. C. Vicario, B. Monoszlai, and C. P. Hauri, "GV/m single-cycle terahertz fields from a laser-driven large-size partitioned organic crystal," *Phys. Rev. Lett.* **112**, 213901 (2014).
161. C. P. Hauri *et al.*, "Strong-field single-cycle THz pulses generated in an organic crystal," *Appl. Phys. Lett.* **99**, 161116 (2011).
162. A. Baltuška, T. Fuji, and T. Kobayashi, "Controlling the carrier-envelope phase of ultrashort light pulses with optical parametric amplifiers," *Phys. Rev. Lett.* **88**, 133901 (2002).
163. F. Junginger *et al.*, "Single-cycle multiterahertz transients with peak fields above 10 MV/cm," *Opt. Lett.* **35**, 2645 (2010).
164. A. Sell, A. Leitenstorfer, and R. Huber, "Phase-locked generation and field-resolved detection of widely tunable terahertz pulses with amplitudes exceeding 100 MV/cm," *Opt. Lett.* **33**, 2767 (2008).
165. B. Liu *et al.*, "Generation of narrowband, high-intensity, carrier-envelope phase-stable pulses tunable between 4 and 18 THz," *Opt. Lett.* **42**, 129 (2017).
166. M. Knorr *et al.*, "Phase-locked multi-terahertz electric fields exceeding 13 MV/cm at a 190 kHz repetition rate," *Opt. Lett.* **42**, 4367 (2017).

167. M. Musheghyan *et al.*, "Tunable, few-cycle, CEP-stable mid-IR optical parametric amplifier for strong field applications," *J. Phys. B* **53**, 185402 (2020).
168. K. Yoshioka *et al.*, "Subcycle mid-infrared coherent transients at 4 MHz repetition rate applicable to light-wave-driven scanning tunneling microscopy," *Opt. Lett.* **44**, 5350 (2019).
169. X. Li *et al.*, "Observation of Dicke cooperativity in magnetic interactions," *Science* **361**, 794 (2018).
170. K. Yamaguchi *et al.*, "Terahertz time-domain observation of spin reorientation in orthoferrite $ErFeO_3$ through magnetic free induction decay," *Phys. Rev. Lett.* **110**, 137204 (2013).
171. J. Jiang *et al.*, "Dynamical spin reorientation transition in $NdFeO_3$ single crystal observed with polarized terahertz time domain spectroscopy," *Appl. Phys. Lett.* **103**, 062403 (2013).
172. T. Suemoto *et al.*, "Magnetization-free measurements of spin orientations in orthoferrites using terahertz time domain spectroscopy," *Appl. Phys. Lett.* **107**, 042404 (2015).
173. H. Horner and C. M. Varma, "Nature of spin-reorientation transitions," *Phys. Rev. Lett.* **20**, 845 (1968).
174. J. Jiang *et al.*, "Magnetic-field dependence of strongly anisotropic spin reorientation transition in $NdFeO_3$: a terahertz study," *J. Phys.* **28**, 116002 (2016).
175. X. Lin *et al.*, "Terahertz probes of magnetic field induced spin reorientation in $YFeO_3$ single crystal," *Appl. Phys. Lett.* **106**, 092403 (2015).
176. J. Scola *et al.*, "Spin reorientation induced by a very high magnetic field in domain-structured $YFeO_3$ films: Emergence of perpendicular anisotropy," *Phys. Rev. B* **81**, 174409 (2010).
177. B. T. Smith, J. Yamamoto, and E. E. Belli, "Far-infrared transmittance of Tb, Ho, Tm, Er, and Yb orthoferrite," *J. Opt. Soc. Am.* **65**, 605 (1975).
178. A. A. Mukhin *et al.*, "Submillimeter and far IR spectroscopy of magneto- and electrodipolar rare-earth modes in the orthoferrite $TmFeO_3$," *Phys. Lett. A* **153**, 499 (1991).
179. K. Zhang *et al.*, "Resolving the spin reorientation and crystal-field transitions in $TmFeO_3$ with terahertz transient," *Sci. Rep.* **6**, 23648 (2016).
180. R. V. Mikhaylovskiy *et al.*, "Selective excitation of terahertz magnetic and electric dipoles in Er^{3+} ions by femtosecond laser pulses in $ErFeO_3$," *Phys. Rev. Lett.* **118**, 017205 (2017).
181. A. P. Pyatakov and A. K. Zvezdin, "Magnetoelectric and multiferroic media," *Phys. Usp.* **182**, 593 (2012).
182. A. Pimenov *et al.*, "Possible evidence for electromagnons in multiferroic manganites," *Nat. Phys.* **2**, 97 (2006).
183. T. Kubacka *et al.*, "Large-amplitude spin dynamics driven by a THz pulse in resonance with an electromagnon," *Science* **343**, 1333 (2014).
184. N. Kida and Y. Tokura, "Terahertz magnetoelectric response via electromagnons in magnetic oxides," *J. Magn. Magn. Mater.* **324**, 3512 (2012).
185. A. Pimenov *et al.*, "Electromagnons in multiferroic manganites," *J. Phys.* **20**, 434209 (2008).
186. F. Matsukura, Y. Tokura, and H. Ohno, "Control of magnetism by electric fields," *Nat. Nanotechnol.* **10**, 209 (2015).
187. Y. Tokura, "Multiferroics—toward strong coupling between magnetization and polarization in a solid," *J. Magn. Magn. Mater.* **310**, 1145 (2007).
188. Y. Tokunaga *et al.*, "Composite domain walls in a multiferroic perovskite ferrite," *Nat. Mater.* **8**, 558 (2009).
189. Y. Tokunaga *et al.*, "Magnetic-field-induced ferroelectric state in $DyFeO_3$," *Phys. Rev. Lett.* **101**, 097205 (2008).
190. E. F. Bertaut *et al.*, "Structures magnetiques de $TbFeO_3$," *Solid State Commun.* **5**, 293 (1967).
191. S. Artyukhin *et al.*, "Solitonic lattice and Yukawa forces in the rare-earth orthoferrite $TbFeO_3$," *Nat. Mater.* **11**, 694 (2012).
192. J.-H. Lee *et al.*, "Spin-canting-induced improper ferroelectricity and spontaneous magnetization reversal in $SmFeO_3$," *Phys. Rev. Lett.* **107**, 117201 (2011).
193. R. D. Johnson, N. Terada, and P. G. Radaelli, "Comment on "spin-canting-induced improper ferroelectricity and spontaneous magnetization reversal in $SmFeO_3$"," *Phys. Rev. Lett.* **108**, 219701 (2012).
194. C.-Y. Kuo *et al.*, "k = 0 magnetic structure and absence of ferroelectricity in $SmFeO_3$," *Phys. Rev. Lett.* **113**, 217203 (2014).
195. T. N. Stanislavchuk *et al.*, "Magnon and electromagnon excitations in multiferroic $DyFeO_3$," *Phys. Rev. B* **93**, 094403 (2016).
196. T. N. Stanislavchuk *et al.*, "Far-IR magnetospectroscopy of magnons and electromagnons in $TbFeO_3$ single crystals at low temperatures," *Phys. Rev. B* **95**, 054427 (2017).
197. S. L. Gnatchenko *et al.*, "Two-step metamagnetic phase transition induced by a magnetic field parallel to the b-axis in $DyFeO_3$," *J. Magn. Magn. Mater.* **129**, 307 (1994).
198. D. Awschalom, N. Samarth, and D. Loss, *Semiconductor Spintronics and Quantum Computation* (Springer, 2011).
199. J. R. Weber *et al.*, "Quantum computing with defects," *Proc. Natl. Acad. Sci. U.S.A.* **107**, 8513 (2010).
200. D. D. Awschalom *et al.*, "Quantum spintronics: engineering and manipulating atom-like spins in semiconductors," *Science* **339**, 1174 (2013).
201. A. Ron *et al.*, "Ultrafast enhancement of ferromagnetic spin exchange induced by ligand-to-metal charge transfer," *Phys. Rev. Lett.* **125**, 197203 (2020).
202. T. Li *et al.*, "Femtosecond switching of magnetism via strongly correlated spin–charge quantum excitations," *Nature* **496**, 69 (2013).
203. M. Matsubara *et al.*, "Ultrafast photoinduced insulator-ferromagnet transition in the perovskite manganite $Gd_{0.55}Sr_{0.45}MnO_3$," *Phys. Rev. Lett.* **99**, 207401 (2007).
204. J. Wang *et al.*, "Ultrafast enhancement of ferromagnetism via photoexcited holes in GaMnAs," *Phys. Rev. Lett.* **98**, 217401 (2007).
205. D. Bossini *et al.*, "Femtosecond activation of magnetoelectricity," *Nat. Phys* **14**, 370 (2018).
206. A. S. Disa *et al.*, "Polarizing an antiferromagnet by optical engineering of the crystal field," *Nat. Phys.* **16**, 937 (2020).
207. A. S. Disa *et al.*, "Optical stabilization of fluctuating high temperature ferromagnetism in $YTiO_3$," arXiv:2111.13622 (2021).
208. M. Först *et al.*, "Driving magnetic order in a manganite by ultrafast lattice excitation," *Phys. Rev. B* **84**, 241104 (2011).
209. E. Fradkin, S. A. Kivelson, and J. M. Tranquada, "Colloquium: theory of intertwined orders in high temperature superconductors," *Rev. Mod. Phys.* **87**, 457 (2015).
210. Z. Sun and A. J. Millis, "Transient trapping into metastable states in systems with competing orders," *Phys. Rev. X* **10**, 021028 (2020).
211. M. H. Kalthoff *et al.*, "Nonequilibrium phase transition in a driven-dissipative quantum antiferromagnet," *Phys. Rev. Res.* **4**, 023115 (2022).
212. K. Balzer *et al.*, "Nonthermal melting of Néel order in the Hubbard model," *Phys. Rev. X* **5**, 031039 (2015).
213. M. Claassen *et al.*, "Dynamical time-reversal symmetry breaking and photo-induced chiral spin liquids in frustrated Mott insulators," *Nat. Commun.* **8**, 1192 (2017).
214. D. Golež *et al.*, "Mechanism of ultrafast relaxation of a photocarrier in antiferromagnetic spin background," *Phys. Rev. B* **89**, 165118 (2014).
215. J. Liu, K. Hejazi, and L. Balents, "Floquet engineering of multiorbital Mott insulators: applications to orthorhombic titanates," *Phys. Rev. Lett.* **121**, 107201 (2018).
216. E. Beaurepaire *et al.*, "Ultrafast spin dynamics in ferromagnetic nickel," *Phys. Rev. Lett.* **76**, 4250 (1996).
217. P. M. Oppeneer and A. Liebsch, "Ultrafast demagnetization in Ni: theory of magneto-optics for non-equilibrium electron distributions," *J. Phys.* **16**, 5519 (2004).
218. J. Wang *et al.*, "Ultrafast magneto-optics in ferromagnetic III–V semiconductors," *J. Phys.* **18**, R501 (2006).

219. J. Wang *et al.*, "Ultrafast quenching of ferromagnetism in InMnAs induced by intense laser irradiation," *Phys. Rev. Lett.* **95**, 167401 (2005).
220. J. Wang *et al.*, "Femtosecond demagnetization and hot-hole relaxation in ferromagnetic $Ga_{1-x}Mn_xAs$," *Phys. Rev. B* **77**, 235308 (2008).
221. E. Kojima *et al.*, "Observation of the spin-charge thermal isolation of ferromagnetic $Ga_{0.94}Mn_{0.06}As$ by time-resolved magneto-optical measurements," *Phys. Rev. B* **68**, 193203 (2003).
222. S. A. Crooker *et al.*, "Terahertz spin precession and coherent transfer of angular momenta in magnetic quantum wells," *Phys. Rev. Lett.* **77**, 2814 (1996).
223. T. Ogasawara *et al.*, "General features of photoinduced spin dynamics in ferromagnetic and ferrimagnetic compounds," *Phys. Rev. Lett.* **94**, 087202 (2005).
224. B. Koopmans *et al.*, "Explaining the paradoxical diversity of ultrafast laser-induced demagnetization," *Nat. Mater.* **9**, 259 (2010).
225. A. V. Kimel *et al.*, "Laser-induced ultrafast spin reorientation in the antiferromagnet $TmFeO_3$," *Nature* **429**, 850 (2004).
226. J. A. de Jong *et al.*, "Laser-induced ultrafast spin dynamics in $ErFeO_3$," *Phys. Rev. B* **84**, 104421 (2011).
227. K. Yamaguchi *et al.*, "Dynamics of photoinduced change of magnetoanisotropy parameter in orthoferrites probed with terahertz excited coherent spin precession," *Phys. Rev. B* **92**, 064404 (2015).
228. A. Ellens *et al.*, "Spectral-line-broadening study of the trivalent lanthanide-ion series. II. The variation of the electron-phonon coupling strength through the series," *Phys. Rev. B* **55**, 180 (1997).
229. T. Kurihara *et al.*, "Reconfiguration of magnetic domain structures of $ErFeO_3$ by intense terahertz free electron laser pulses," *Sci. Rep.* **10**, 7321 (2020).
230. D. Afanasiev, A. K. Zvezdin, and A. V. Kimel, "Laser-induced shift of the Morin point in antiferromagnetic $DyFeO_3$," *Opt. Express* **23**, 23978 (2015).
231. A. V. Kimel *et al.*, "Inertia-driven spin switching in antiferromagnets," *Nat. Phys.* **5**, 727 (2009).
232. J. A. de Jong *et al.*, "Coherent control of the route of an ultrafast magnetic phase transition via low-amplitude spin precession," *Phys. Rev. Lett.* **108**, 157601 (2012).
233. T. Kurihara *et al.*, "Macroscopic magnetization control by symmetry breaking of photoinduced spin reorientation with intense terahertz magnetic near field," *Phys. Rev. Lett.* **120**, 107202 (2018).
234. M. Först *et al.*, "Nonlinear phononics as an ultrafast route to lattice control," *Nat. Phys.* **7**, 854 (2011).
235. M. Fechner *et al.*, "Magnetophononics: ultrafast spin control through the lattice," *Phys. Rev. Mater.* **2**, 064401 (2018).
236. R. Mankowsky *et al.*, "Nonlinear lattice dynamics as a basis for enhanced superconductivity in $YBa_2Cu_3O_{6.5}$," *Nature* **516**, 71 (2014).
237. M. Först *et al.*, "Displacive lattice excitation through nonlinear phononics viewed by femtosecond X-ray diffraction," *Solid State Commun.* **169**, 24 (2013).
238. D. Afanasiev *et al.*, "Ultrafast control of magnetic interactions via light-driven phonons," *Nat. Mater.* **20**, 607 (2021).
239. P. G. Radaelli, "Breaking symmetry with light: ultrafast ferroelectricity and magnetism from three-phonon coupling," *Phys. Rev. B* **97**, 085145 (2018).
240. D. M. Juraschek, M. Fechner, and N. A. Spaldin, "Ultrafast structure switching through nonlinear phononics," *Phys. Rev. Lett.* **118**, 054101 (2017).
241. T. F. Nova *et al.*, "An effective magnetic field from optically driven phonons," *Nat. Phys.* **13**, 132 (2017).
242. D. M. Juraschek *et al.*, "Dynamical multiferroicity," *Phys. Rev. Mater.* **1**, 014401 (2017).
243. D. M. Juraschek, P. Narang, and N. A. Spaldin, "Phono-magnetic analogs to opto-magnetic effects," *Phys. Rev. Res.* **2**, 043035 (2020).
244. S. Baierl *et al.*, "Nonlinear spin control by terahertz-driven anisotropy fields," *Nat. Photonics* **10**, 715 (2016).
245. G. Fitzky *et al.*, "Ultrafast control of magnetic anisotropy by resonant excitation of 4*f* electrons and phonons in $Sm_{0.7}Er_{0.3}FeO_3$," *Phys. Rev. Lett.* **127**, 107401 (2021).
246. L. Chaix *et al.*, "Magneto- to electroactive transmutation of spin waves in $ErMnO_3$," *Phys. Rev. Lett.* **112**, 137201 (2014).
247. R. V. Mikhaylovskiy *et al.*, "Terahertz magnetization dynamics induced by femtosecond resonant pumping of Dy^{3+} subsystem in the multisublattice antiferromagnet $DyFeO_3$," *Phys. Rev. B* **92**, 094437 (2015).
248. Y. H. Wang *et al.*, "Observation of Floquet-Bloch states on the surface of a topological insulator," *Science* **342**, 453 (2013).
249. F. Mahmood *et al.*, "Selective scattering between Floquet–Bloch and Volkov states in a topological insulator," *Nat. Phys.* **12**, 306 (2016).
250. E. J. Sie *et al.*, "Large, valley-exclusive Bloch-Siegert shift in monolayer WS_2," *Science* **355**, 1066 (2017).
251. J.-Y. Shan *et al.*, "Giant modulation of optical nonlinearity by Floquet engineering," *Nature* **600**, 235 (2021).
252. M. Nuske *et al.*, "Floquet dynamics in light-driven solids," *Phys. Rev. Res.* **2**, 043408 (2020).
253. N. H. Lindner, G. Refael, and V. Galitski, "Floquet topological insulator in semiconductor quantum wells," *Nat. Phys.* **7**, 490 (2011).
254. J. Cayssol *et al.*, "Floquet topological insulators," *Phys. Status Solidi RRL* **7**, 101 (2013).
255. J. W. McIver *et al.*, "Light-induced anomalous Hall effect in graphene," *Nat. Phys.* **16**, 38 (2020).
256. J. H. Mentink, K. Balzer, and M. Eckstein, "Ultrafast and reversible control of the exchange interaction in Mott insulators," *Nat. Commun.* **6**, 6708 (2015).
257. K. Hejazi, J. Liu, and L. Balents, "Floquet spin and spin-orbital Hamiltonians and doublon-holon generations in periodically driven Mott insulators," *Phys. Rev. B* **99**, 205111 (2019).
258. G. Batignani *et al.*, "Probing ultrafast photo-induced dynamics of the exchange energy in a Heisenberg antiferromagnet," *Nat. Photonics* **9**, 506 (2015).
259. Y. Wang, T. P. Devereaux, and C.-C. Chen, "Theory of time-resolved Raman scattering in correlated systems: ultrafast engineering of spin dynamics and detection of thermalization," *Phys. Rev. B* **98**, 245106 (2018).
260. J. Zhang *et al.*, "Observation of a discrete time crystal," *Nature* **543**, 217 (2017).
261. J. H. Shirley, "Solution of the Schrödinger equation with a Hamiltonian periodic in time," *Phys. Rev.* **138**, B979 (1965).
262. M. S. Rudner and N. H. Lindner, "The Floquet engineer's handbook," arXiv:2003.08252 (2020).
263. S. Chaudhary, D. Hsieh, and G. Refael, "Orbital Floquet engineering of exchange interactions in magnetic materials," *Phys. Rev. B* **100**, 220403 (2019).
264. Y. Wang *et al.*, "X-ray scattering from light-driven spin fluctuations in a doped Mott insulator," *Commun. Phys.* **4**, 212 (2021).
265. A. Hirohata *et al.*, "Review on spintronics: principles and device applications," *J. Magn. Magn. Mater.* **509**, 166711 (2020).
266. M. N. Baibich *et al.*, "Giant magnetoresistance of (001)Fe/(001) Cr magnetic superlattices," *Phys. Rev. Lett.* **61**, 2472 (1988).
267. T. Miyazaki and N. Tezuka, "Giant magnetic tunneling effect in $Fe/Al_2O_3/Fe$ junction," *J. Magn. Magn. Mater.* **139**, L231 (1995).
268. L. Berger, "Emission of spin waves by a magnetic multilayer traversed by a current," *Phys. Rev. B* **54**, 9353 (1996).
269. S. Araki *et al.*, "Which spin valve for next giant magnetoresistance head generation?" *J. Appl. Phys.* **87**, 5377 (2000).
270. T. Jungwirth *et al.*, "The multiple directions of antiferromagnetic spintronics," *Nat. Phys.* **14**, 200 (2018).
271. S. K. Kim *et al.*, "Ferrimagnetic spintronics," *Nat. Mater.* **21**, 24 (2022).

272. J. Železný *et al.*, "Spin transport and spin torque in antiferromagnetic devices," *Nat. Phys.* **14**, 220 (2018).
273. P. Wadley *et al.*, "Electrical switching of an antiferromagnet," *Science* **351**, 587 (2016).
274. B. Dieny *et al.*, "Opportunities and challenges for spintronics in the microelectronics industry," *Nat. Electron.* **3**, 446 (2020).
275. H. Watanabe *et al.*, "Observation of long-lived coherent spin precession in orthoferrite $ErFeO_3$ induced by terahertz magnetic fields," *Appl. Phys. Lett.* **111**, 092401 (2017).
276. T. Kampfrath *et al.*, "Coherent terahertz control of antiferromagnetic spin waves," *Nat. Photonics* **5**, 31 (2011).
277. T. Kohmoto and T. Moriyasu, "Ultrafast magnon dynamics in antiferromagnetic nickel oxide observed by optical pump-probe and terahertz time-domain spectroscopies," in *2018 43rd International Conference on Infrared, Millimeter, and Terahertz Waves (IRMMW-THz)* (IEEE, 2018), p. 1.
278. E. A. Mashkovich *et al.*, "Terahertz light–driven coupling of antiferromagnetic spins to lattice," *Science* **374**, 1608 (2021).
279. D. J. Lockwood and M. G. Cottam, "Light scattering from magnons in MnF_2," *Phys. Rev. B* **35**, 1973 (1987).
280. A. B. Ustinov *et al.*, "Q factor of dual-tunable microwave resonators based on yttrium iron garnet and barium strontium titanate layered structures," *J. Appl. Phys.* **103**, 063908 (2008).
281. R. C. LeCraw, E. G. Spencer, and C. S. Porter, "Ferromagnetic resonance line width in yttrium iron garnet single crystals," *Phys. Rev.* **110**, 1311 (1958).
282. S. Dai, S. A. Bhave, and R. Wang, "Octave-tunable magnetostatic wave YIG resonators on a chip," *IEEE Trans. Ultrason. Ferroelectr. Freq. Control* **67**, 2454 (2020).
283. M. P. Kostylev *et al.*, "Spin-wave logical gates," *Appl. Phys. Lett.* **87**, 153501 (2005).
284. K. Yamaguchi, M. Nakajima, and T. Suemoto, "Coherent control of spin precession motion with impulsive magnetic fields of half-cycle terahertz radiation," *Phys. Rev. Lett.* **105**, 237201 (2010).
285. Z. Jin *et al.*, "Single-pulse terahertz coherent control of spin resonance in the canted antiferromagnet $YFeO_3$, mediated by dielectric anisotropy," *Phys. Rev. B* **87**, 094422 (2013).
286. M. F. DeCamp *et al.*, "Dynamics and coherent control of high-amplitude optical phonons in bismuth," *Phys. Rev. B* **64**, 092301 (2001).
287. É. D. Murray *et al.*, "Effect of lattice anharmonicity on high-amplitude phonon dynamics in photoexcited bismuth," *Phys. Rev. B* **72**, 060301 (2005).
288. Y.-H. Cheng *et al.*, "Coherent control of optical phonons in bismuth," *Phys. Rev. B* **96**, 134302 (2017).
289. T. Arikawa *et al.*, "Quantum control of a Landau-quantized two-dimensional electron gas in a GaAs quantum well using coherent terahertz pulses," *Phys. Rev. B* **84**, 241307 (2011).
290. A. Haldar and A. O. Adeyeye, "Functional magnetic waveguides for magnonics," *Appl. Phys. Lett.* **119**, 060501 (2021).
291. X. Zhang *et al.*, "Strongly coupled magnons and cavity microwave photons," *Phys. Rev. Lett.* **113**, 156401 (2014).
292. Y. Tabuchi *et al.*, "Hybridizing ferromagnetic magnons and microwave photons in the quantum limit," *Phys. Rev. Lett.* **113**, 083603 (2014).
293. Y.-P. Wang *et al.*, "Bistability of cavity magnon polaritons," *Phys. Rev. Lett.* **120**, 057202 (2018).
294. J. B. Curtis *et al.*, "Cavity magnon-polaritons in cuprate parent compounds," *Phys. Rev. Res.* **4**, 013101 (2022).
295. P. Sivarajah *et al.*, "THz-frequency magnon-phonon-polaritons in the collective strong-coupling regime," *J. Appl. Phys.* **125**, 213103 (2019).
296. M. Białek, A. Magrez, and J.-Ph. Ansermet, "Spin-wave coupling to electromagnetic cavity fields in dysposium ferrite," *Phys. Rev. B* **101**, 024405 (2020).
297. K. Grishunin *et al.*, "Terahertz magnon-polaritons in $TmFeO_3$," *ACS Photonics* **5**, 1375 (2018).
298. A. Baydin *et al.*, "Magnetically tuned continuous transition from weak to strong coupling in terahertz magnon polaritons," arXiv:2208.10030 (2022).
299. J. R. Hortensius *et al.*, "Coherent spin-wave transport in an antiferromagnet," *Nat. Phys.* **17**, 1001 (2021).
300. M. T. Johnson, *et al.*, "Magnetic anisotropy in metallic multilayers," *Rep. Prog. Phys.* **59**, 1409 (1996).
301. S. Andrieu *et al.*, "Co/Ni multilayers for spintronics: high spin polarization and tunable magnetic anisotropy," *Phys. Rev. Mater.* **2**, 064410 (2018).
302. J. Liu and T. Hesjedal, "Magnetic topological insulator heterostructures: a review," *Adv. Mater.* 2102427 (2021).
303. M. Gibertini *et al.*, "Magnetic 2D materials and heterostructures," *Nat. Nanotechnol.* **14**, 408 (2019).
304. W. H. Meiklejohn and C. P. Bean, "New magnetic anisotropy," *Phys. Rev.* **105**, 904 (1957).
305. J. Tang *et al.*, "Ultrafast photoinduced multimode antiferromagnetic spin dynamics in exchange-coupled Fe/$RFeO_3$ (R = Er or Dy) heterostructures," *Adv. Mater.* **30**, 1706439 (2018).
306. L. Joly *et al.*, "Spin-reorientation in the heterostructure Co/$SmFeO_3$," *J. Phys.* **21**, 446004 (2009).
307. L. Le Guyader *et al.*, "Dynamics of laser-induced spin reorientation in Co/$SmFeO_3$ heterostructure," *Phys. Rev. B* **87**, 054437 (2013).
308. W. Nolting, *Theoretical Physics 9: Fundamentals of Many-body Physics* (Springer International Publishing, 2018).
309. A. V. Chumak, A. A. Serga, and B. Hillebrands, "Magnon transistor for all-magnon data processing," *Nat. Commun.* **5**, 4700 (2014).
310. B. A. Kalinikos, N. G. Kovshikov, and A. N. Slavin, "Experimental observation of magnetostatic wave envelope solitons in yttrium iron garnet films," *Phys. Rev. B* **42**, 8658 (1990).
311. A. A. Serga *et al.*, "Parametric generation of forward and phase-conjugated spin-wave bullets in magnetic films," *Phys. Rev. Lett.* **94**, 167202 (2005).
312. S. Schlauderer *et al.*, "Temporal and spectral fingerprints of ultrafast all-coherent spin switching," *Nature* **569**, 383 (2019).
313. J. Lu *et al.*, "Coherent two-dimensional terahertz magnetic resonance spectroscopy of collective spin waves," *Phys. Rev. Lett.* **118**, 207204 (2017).
314. P. Hamm and M. Zanni, *Concepts and Methods of 2D Infrared Spectroscopy* (Cambridge University Press, 2011).
315. W. Kuehn *et al.*, "Strong correlation of electronic and lattice excitations in GaAs/AlGaAs semiconductor quantum wells revealed by two-dimensional terahertz spectroscopy," *Phys. Rev. Lett.* **107**, 067401 (2011).
316. C. Somma *et al.*, "Two-phonon quantum coherences in indium antimonide studied by nonlinear two-dimensional terahertz spectroscopy," *Phys. Rev. Lett.* **116**, 177401 (2016).
317. C. L. Johnson, B. E. Knighton, and J. A. Johnson, "Distinguishing nonlinear terahertz excitation pathways with two-dimensional spectroscopy," *Phys. Rev. Lett.* **122**, 073901 (2019).
318. F. Mahmood *et al.*, "Observation of a marginal Fermi glass," *Nat. Phys.* **17**, 627 (2021).
319. J. Mornhinweg *et al.*, "Tailored subcycle nonlinearities of ultrastrong light-matter coupling," *Phys. Rev. Lett.* **126**, 177404 (2021).
320. S. Pal *et al.*, "Origin of terahertz soft-mode nonlinearities in ferroelectric perovskites," *Phys. Rev. X* **11**, 021023 (2021).
321. M. Mootz, *et al.*, "Visualization and quantum control of light-accelerated condensates by terahertz multi-dimensional coherent spectroscopy," *Commun. Phys.* **5**, 47 (2022).
322. Z. Zhang *et al.*, "Nonlinear coupled magnonics: terahertz field-driven magnon upconversion," arXiv:2207.07103 (2022).
323. Y. Wan and N. P. Armitage, "Resolving continua of fractional excitations by spinon echo in THz 2D coherent spectroscopy," *Phys. Rev. Lett.* **122**, 257401 (2019).

324. W. Choi, K. H. Lee, and Y. B. Kim, "Theory of two-dimensional nonlinear spectroscopy for the Kitaev spin liquid," *Phys. Rev. Lett.* **124**, 117205 (2020).
325. S. Ghosh *et al.*, "Microcavity exciton polaritons at room temperature," *Photon. Insights* **1**, R04 (2022).
326. A. Bayer *et al.*, "Terahertz light–matter interaction beyond unity coupling strength," *Nano Lett.* **17**, 6340 (2017).
327. W. Gao *et al.*, "Continuous transition between weak and ultrastrong coupling through exceptional points in carbon nanotube microcavity exciton–polaritons," *Nat. Photonics* **12**, 362 (2018).
328. X. Li *et al.*, "Vacuum Bloch–Siegert shift in Landau polaritons with ultra-high cooperativity," *Nat. Photonics* **12**, 324 (2018).
329. G. Scalari *et al.*, "Ultrastrong coupling of the cyclotron transition of a 2D electron gas to a THz metamaterial," *Science* **335**, 1323 (2012).
330. F. Yoshihara *et al.*, "Superconducting qubit–oscillator circuit beyond the ultrastrong-coupling regime," *Nat. Phys* **13**, 44 (2017).
331. Y. Todorov *et al.*, "Ultrastrong light-matter coupling regime with polariton dots," *Phys. Rev. Lett.* **105**, 196402 (2010).
332. V. M. Muravev *et al.*, "Observation of hybrid plasmon-photon modes in microwave transmission of coplanar microresonators," *Phys. Rev. B* **83**, 075309 (2011).
333. C. Leroux, L. C. G. Govia, and A. A. Clerk, "Enhancing cavity quantum electrodynamics via antisqueezing: synthetic ultrastrong coupling," *Phys. Rev. Lett.* **120**, 093602 (2018).
334. W. Qin *et al.*, "Exponentially enhanced light-matter interaction, cooperativities, and steady-state entanglement using parametric amplification," *Phys. Rev. Lett.* **120**, 093601 (2018).
335. G. Romero *et al.*, "Ultrafast quantum gates in circuit QED," *Phys. Rev. Lett.* **108**, 120501 (2012).
336. P. Nataf and C. Ciuti, "Protected quantum computation with multiple resonators in ultrastrong coupling circuit QED," *Phys. Rev. Lett.* **107**, 190402 (2011).
337. P. Nataf and C. Ciuti, "No-go theorem for superradiant quantum phase transitions in cavity QED and counter-example in circuit QED," *Nat. Commun.* **1**, 72 (2010).
338. K. Hayashida *et al.*, "Perfect intrinsic squeezing at the superradiant phase transition critical point," arXiv:2009.02630 (2020).
339. Q. Zhang *et al.*, "Collective non-perturbative coupling of 2D electrons with high-quality-factor terahertz cavity photons," *Nat. Phys.* **12**, 1005 (2016).
340. R. H. Dicke, "Coherence in spontaneous radiation processes," *Phys. Rev.* **93**, 99 (1954).
341. K. Hepp and E. H. Lieb, "On the superradiant phase transition for molecules in a quantized radiation field: the Dicke maser model," *Ann. Phys.* **76**, 360 (1973).
342. Y. K. Wang and F. T. Hioe, "Phase transition in the Dicke model of superradiance," *Phys. Rev. A* **7**, 831 (1973).
343. R. G. Woolley, "Gauge invariance and the thermodynamics of the electromagnetic field," *J. Phys. A* **9**, L15 (1976).
344. I. Bialynicki-Birula and K. Rzążewski, "No-go theorem concerning the superradiant phase transition in atomic systems," *Phys. Rev. A* **19**, 301 (1979).
345. G. M. Andolina *et al.*, "Theory of photon condensation in a spatially varying electromagnetic field," *Phys. Rev. B* **102**, 125137 (2020).
346. M. Bamba and T. Ogawa, "Stability of polarizable materials against superradiant phase transition," *Phys. Rev. A* **90**, 063825 (2014).
347. L. Chirolli *et al.*, "Drude weight, cyclotron resonance, and the Dicke model of graphene cavity QED," *Phys. Rev. Lett.* **109**, 267404 (2012).
348. K. Baumann *et al.*, "Dicke quantum phase transition with a superfluid gas in an optical cavity," *Nature* **464**, 1301 (2010).
349. Z. Zhiqiang *et al.*, "Nonequilibrium phase transition in a spin-1 Dicke model," *Optica* **4**, 424 (2017).
350. J. M. Knight, Y. Aharonov, and G. T. C. Hsieh, "Are superradiant phase transitions possible?" *Phys. Rev. A* **17**, 1454 (1978).
351. M. Bamba and N. Imoto, "Circuit configurations which may or may not show superradiant phase transitions," *Phys. Rev. A* **96**, 053857 (2017).
352. P. Nataf *et al.*, "Rashba cavity QED: a route towards the superradiant quantum phase transition," *Phys. Rev. Lett.* **123**, 207402 (2019).
353. C. Riek *et al.*, "Direct sampling of electric-field vacuum fluctuations," *Science* **350**, 420 (2015).
354. C. Riek *et al.*, "Subcycle quantum electrodynamics," *Nature* **541**, 376 (2017).
355. F. F. Settembrini *et al.*, "Detection of quantum-vacuum field correlations outside the light cone," *Nat. Commun.* **13**, 3383 (2022).
356. M. Bamba *et al.*, "Magnonic superradiant phase transition," *Commun. Phys.* **5**, 3 (2022).
357. X. X. Zhang *et al.*, "Magnetic behavior and complete high-field magnetic phase diagram of the orthoferrite $ErFeO_3$," *Phys. Rev. B* **100**, 054418 (2019).
358. N. Marquez Peraca *et al.*, "Spin-magnon Dicke phase transition in $ErFeO_3$," in preparation (2022).
359. T. Makihara *et al.*, "Ultrastrong magnon–magnon coupling dominated by antiresonant interactions," *Nat. Commun.* **12**, 3115 (2021).
360. G. T. Noe *et al.*, "A table-top, repetitive pulsed magnet for nonlinear and ultrafast spectroscopy in high magnetic fields up to 30 T," *Rev. Sci. Instrum.* **84**, 123906 (2013).
361. M. O. Scully and M. S. Zubairy, *Quantum Optics* (Cambridge University Press, 1997).
362. R. E. Slusher *et al.*, "Observation of squeezed states generated by four-wave mixing in an optical cavity," *Phys. Rev. Lett.* **55**, 2409 (1985).
363. L.-A. Wu *et al.*, "Generation of squeezed states by parametric down conversion," *Phys. Rev. Lett.* **57**, 2520 (1986).
364. T. Kurihara *et al.*, "Spin canting in nonlinear terahertz magnon dynamics revealed by magnetorefractive probing in orthoferrite," arXiv:2202.11365 (2022).